NON-PRECIOUS METAL CATALYSIS FOR PROTON-EXCHANGE MEMBRANE FUEL CELLS

By

Nathaniel Dean Leonard

A DISSERTATION

Submitted to
Michigan State University
In partial fulfillment of the requirements
for the degree of

Chemical Engineering—Doctor of Philosophy

2015

ABSTRACT

NON-PRECIOUS METAL CATALYSIS FOR PROTON-EXCHANGE MEMBRANE FUEL CELLS

By

Nathaniel Dean Leonard

Non-precious metal catalysts (NPMC) for proton exchange membrane fuel cells (PEMFC) are explored. Research into NPMCs is motivated by the growing need for cleaner, more efficient energy options. NPMCs are one option to make fuel cells more commercially viable. To this end, the present work studies and simulates the morphology and function of metal-nitrogen-carbon (MNC) oxygen reduction catalysts.

A porosity study finds that mesoporosity is critical to high performance of autogenic pressure metal-nitrogen-carbon (APMNC) oxygen reduction catalysts. Various carbon materials are used as precursors to synthesis APMNC catalysts. The catalysts and the associated porous carbon materials are characterized morphologically, chemically, and electrochemically. The results indicated that substrates adsorbing the most nitrogen and iron show the highest activity. Furthermore, a relationship is found between mesoporosity and nitrogen content indicating the importance of transport to active site creation.

A correlation is found between surface alkalinity and catalytic activity for APMNC catalysts. The basic site strength and quantity were calculated by two different methods, and it was shown that increased Brønsted- Lowry basicity correlates to more active catalysts. The relationship between alkalinity and catalytic activity could be the

result of the impact of alkalinity on the electron density of the metal centers or basic sites could encourage active site formation.

It is found that the oxygen reduction reaction (ORR) proceeds both via a direct four-electron pathway to water at high potentials and an indirect peroxide pathway at low potentials on an APMNC catalyst. At higher potential, site availability inhibits peroxide generation causing the direct four-electron reduction pathway to dominate. Oxygen reduction begins to shift to the indirect peroxide pathway due to fast kinetics and higher site availability around 0.6 V vs RHE. The net peroxide generation remains relatively low over the entire range due to reduction of peroxide to water.

A PEMFC cathode model is developed for hydrophilic MNC catalysts. Water flooding was studied in terms of its impact on gas-phase transport and electrochemically accessible surface area (ECSA). Fuel cell data is modeled at a variety of pressures and catalyst layer thicknesses. A sensitivity study is performed on the controllable cathode parameters. Sensitivity analysis identified loading and density as critical parameters, and parametric studies indicated that decreased loading would lead to higher catalyst utilization. Also, density and loading of the catalyst layer are optimized for various fuel cell potential regions.

This dissertation is dedicated to Kelly and Natalie

ACKNOWLEDGEMENTS

I would like two acknowledge my family and friends for their spiritual and psychological support as well as my advisor and colleagues for their academic and technical mentorship and help. I would also like to acknowledge my funding sources, which have included during my tenure at MSU the Nation Science Foundation, the Department of Energy through its Hydrogen and Fuel Program via Northeastern University, Air Force Research Laboratory through the Student Research Participation Program by the Oak Ridge Institute for Science and Education, and the State of Michigan through the Department of Chemical Engineering and Material Science at Michigan State University

TABLE OF CONTENTS

LIST OF TABLES

LIST OF FIGURES

Chapter 1 Introduction

1.1. Motivation

As energy demand rises due to technology and population increases,[1,2] energy sources also need to change: research shows the detrimental impact our current energy technologies are having on our world.[3] This makes the challenges two-fold: not only do we have to improve energy availability, but we also have to provide the energy responsibly. For the present dissertation we will be concentrating on a specific energy technology that has the potential to be both efficient and clean: fuel cells.[4,5]

Fuel cells can be highly efficient in comparison to combustion technologies because less energy is wasted in the form of heat and sound,[5] furthermore the ability to utilize fuels such as hydrogen[5] or hydrazine[5,6] allow carbon emissions to be reduced. Although fuel cells have these advantages over current energy technologies, the challenge with fuel cells has been competing on a cost, power, and durability basis.[4,5,7] These three challenges have guided fuel cell research over the past decades, and catalysis is at the center of it. With better and cheaper catalysts, costs can be cut, power density can be improved, and the benefits of fuel cell technologies can be realized.

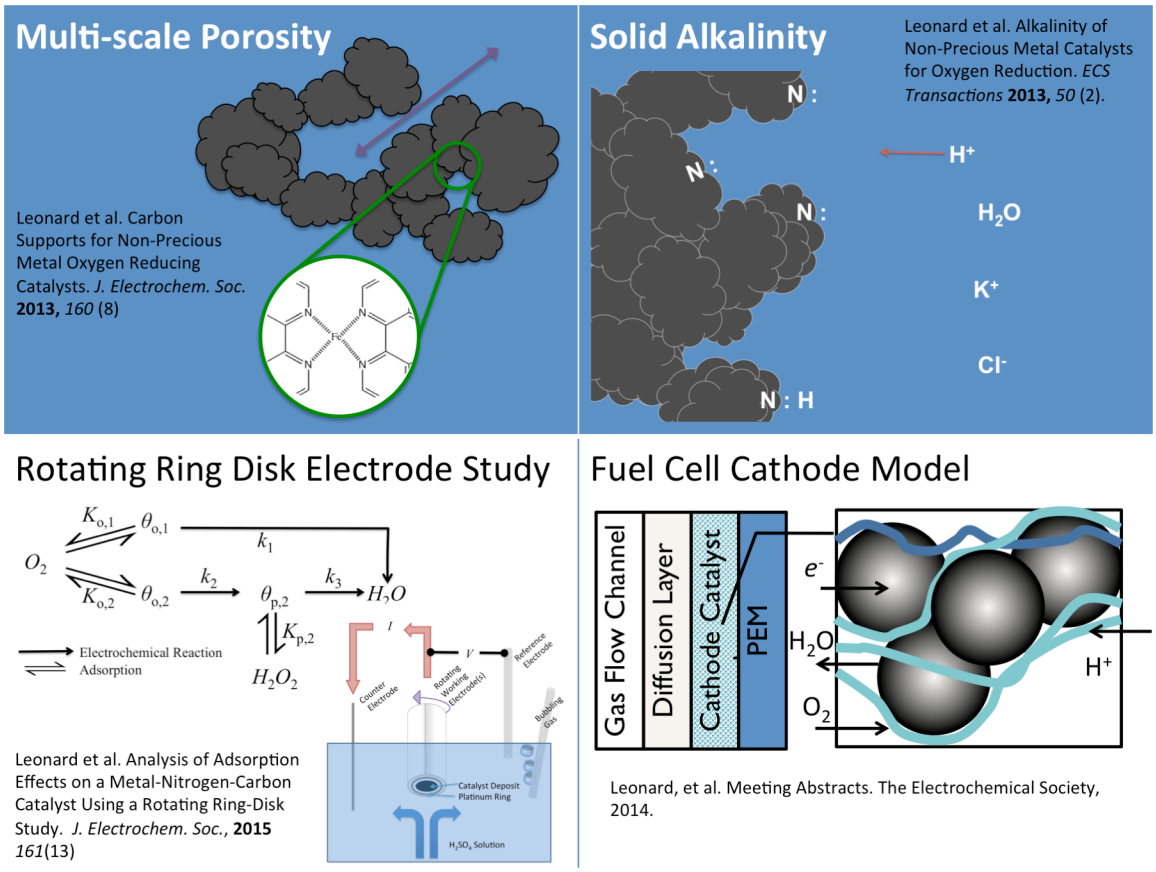

Figure 1.1: Graphical Abstracts of (a) Chapter 2 Carbon Supports for Non-precious Metal Oxygen Reducing Catalysts, (b) Chapter 3 Solid Alkalinity of MNC Catalyst for Oxygen Reduction Reaction, (c) Chapter 4 Analysis of Adsorption Effects on a Metal-Nitrogen-Carbon Catalyst using a Rotating Ring-Disk Study, and (d) Chapter 5 Transport Model for Thick PEMFC Cathodes

1.2. Overview of Work

This dissertation has increased understanding of MNC catalyst function and synthesis with four chapters:

1. Evaluation of the impact of mesoporosity on catalyst properties: A correlation between mesoporosity and activity is found, suggesting that mesoporosity increases active site creation or utilization.

2. Exploration of surface alkalinity in MNC catalysts: A correlation between activity and pH is observed, and the basic site strength and quantity are calculated by two different methods.
3. Exploration of peroxide generation of MNC catalysts: rotating ring-disk electrode (RRDE) studies are used to detect peroxide generation and deduce oxygen adsorption limitations for the MSU catalyst.
4. Numerically model catalyst function in fuel cell context: A thick, hydrophilic fuel cell membrane-electrode assemblies (MEAs) has been modeled to understand transport in an MNC catalyst developed by collaborators at the University of New Mexico.

Chapters one and three resulted in peer-reviewed journal publications.[8,9] Chapter two was published as a conference proceeding,[10] and Chapter four was presented at the ECS/SMEQ Joint International Meeting on October, 9th 2014, and the resulting paper is submitted. The final chapter will consider the impact of the current dissertation, and how future research efforts should be concentrated.

Of the competing MNC catalyst surveyed in the previous section, these chapters explore two of them. The first three chapters consider a high-pressure synthesis process developed at MSU in which the nitrogen precursors break down during the pyrolysis and the high partial pressure of nitrogen intermediates enhances catalyst site creation. The fourth and final chapter considers the modeling of a catalyst developed by collaborators at the University of New Mexico (UNM). This catalyst involves a hard templating of the catalyst particles around silica agglomerates. The templating ensures high quantities of mesoporosity. The importance of mesoporosity was main conclusion from chapter two.

1.3. Competing Fuel Cell Technologies

A fuel cell is a steady-state galvanic electrochemical reactor in which a fuel is oxidized and an oxidant reduced in order to convert chemical energy to electrical energy. There are many different types of fuel cells. They operate at range of temperatures and a variety of fuels, but the basics are: an anode where the fuel is oxidized, a cathode where the oxidant (generally oxygen) is reduced, and an electrolyte that allows a charge carrying ion to pass from one electrode to the other. Table 1.1 shows the various types of fuel cells with the two half-cell reactions, the charge-carrying ions, and the operating conditions.

Table 1.1: Fuel Cell Types[4,5]

Fuel Cell Type	Cathode Reaction	Charge-Carrying Ion (Electrolyte) ← →	Anode Reaction	Operating Conditions
Proton Exchange Membrane Fuel Cell (PEMFC)	$O_2 + 4H^+ + 4e^- \rightarrow H_2O$	H^+ (in a polymer membrane)	$2H_2 \rightarrow 4H^+ + 4e^-$	50-100 °C with air and hydrogen gases[4]
Alkaline Fuel Cell (AFC)	$O_2 + 2H_2O + 4e^- \rightarrow 4OH^-$	OH^-	$2H_2 + 4OH^- \rightarrow 4H_2O + 4e^-$	60-200 °C with air and hydrogen gases[5]
Solid Oxide Fuel Cell (SOFC)	$O_2 + 2e^- \rightarrow O^{2-}$	O^{2-}	$O^{2-} + Fuel \rightarrow 2e^- + Fuel\ oxide$	600-1000 °C with air and a variety of fuels[4]
Phosphoric Acid Fuel Cell (PAFC)	$O_2 + 4H^+ + 4e^- \rightarrow H_2O$	H^+ (in phosphoric acid)	$2H_2 \rightarrow 4H^+ + 4e^-$	200 °C with air and hydrogen gases[4]
Molten Carbonate Fuel Cell (MCFC)	$O_2 + 2CO_2 + 4e^- \rightarrow 2CO_3^{2-}$	CO_3^{2-}	$2H_2 + 2CO_3^{2-} \rightarrow 4H_2O + 2CO_2 + 4e^-$	650 °C with air and hydrogen gases[4]

Of these fuel cells, solid oxide fuel cells (SOFCs), phosphoric acid fuel cells (PAFCs), and molten carbonate fuel cells (MCFCs) are considered high temperature fuel cells and are used primarily in stationary applications, often when combined heat and power (CHPs) is desired.[4,5] Proton exchange membrane fuel cells (PEMFCs) and alkaline fuel cells (AFCs) are considered

low-temperature fuel cells and are the most researched fuel cells for transportations applications.[4,5]

AFCs have been widely used in the space industry and have the advantage of relatively facile kinetics in comparison to other fuel cell systems, but degradation issues have been the most difficult challenge.[4,5,11,12] Specifically, in aqueous AFCs, any carbon dioxide in the system reacts with hydroxide to form carbonate and bicarbonate, which decreases the electrolyte pH.[4,11,12] Because OH^- is the charge-carrying ion, any decrease in pH results in a decrease in conductivity. Furthermore, these carbonate and bicarbonate ions can degrade electrode material. [4] For this reasons much research has been devoted to developing anion exchange membranes (AEM).[13] Although these membranes improve carbon dioxide tolerance, they generally have stability issues especially at lower hydration levels.[4,13] Although much research has been spent on improving stability, this challenge has caused the transportation industry to invest most of their resources towards PEMFCs.[7,14]

PEMFCs have also been used in the space industry and are the most widely considered fuel cell for automotive applications.[4,5,14] This is due to the high durability and high conductivity of the ionomer membrane.[4,5] The challenge with the PEMFC has been that both half-cell reactions require precious metal catalysts.[4,5] The present dissertation concerns this challenge.

As mentioned in the overview, the primary challenges in competing with internal combustion engines on a cost and performance basis. The primary impediment to competing on a cost basis is the expense of the catalysts. This loading of costly catalysts must also be balanced with the competing concerns of power and durability. Of the two half-cell reactions, the oxygen reduction reaction (ORR) is the most sluggish resulting higher platinum loadings. The anode platinum loadings are generally on the order of 0.05 mg/cm^2, while the cathode loadings range from 0.2-

0.4 mg/cm^2.[4] Due to the higher platinum loading, the cathode catalyst has been the focus of the most research.[4] Table 1.2 shows various catalysts that have been considered for ORR in PEMFCs.

Table 1.2: Oxygen Reduction Catalysts

Catalyst	Performance at 0.6 V / A cm^{-2}	General Form	Metals	Non-metals
Platinum and Platinum Alloys	1.5[15]	Pt_xMe_y	Me=Ni, Mn, Fe, Co, Cu[16]	C-support
Metal-Nitrogen-Carbon HT catalyst	0.4[17]	MeN_xC_y	Me=Fe, Co, Ni, Cu, Mn[18]	N,C
Chalcogenides	0.18[19]	Me_mX_8	Me=Mo, Ru	X=Se
Transition Metal Nitrides and Carbides	0.05[20]	MeX_x	Me=Ti,Ta,W,Mo	X=N,C

For precious metal catalysts the goal is to reduce Pt usage without effecting durability or activity. The current state-of-the-art catalyst for ORR in PEMFCs is de-alloyed $PtNi_3$.[15,21,22] The catalyst is based on a precursor of $PtNi_3$ alloy nanoparticles. Upon heat treatment, de-alloying causes the surface of the nanoparticles to be platinum rich, while the centers are primarily composed of the cheaper Ni metal.[15,21,22] This catalyst has been found to function better the pure platinum not only on a Pt-mass basis, but also the interior Ni has been found to enhance catalytic properties of the Pt-rich surface.[15,21,22] Although these catalyst have extremely high activity on a platinum basis (0.35 A/mg$_{Pt}$), this level of Pt use is still too high (2015 goal: 0.44 A/mg$_{Pt}$).[23,24]

As shown in Table 1.2, there are a number of alternatives to platinum group metal (PGM) catalysts for ORR. The most competitive is metal nitrogen carbon (MNC) catalysts. Jasinski discovered the catalytic activity of metal-N_4 macrocycles.[25] Later developments by Yeager et al. showed improved catalytic activity and durability from a pyrolyzed mixture of cobalt acetate, carbon, and polyacrylonitrile.[26] Ultimately this classification consists of a wide variety of catalysts, but the synthesis procedure generally involves a mixing step involving metal, nitrogen, and carbon precursors followed by a pyrolysis step at 700-1000 °C.[8,17,27-31] The initial pyrolysis

step is followed by a leaching step to remove excess metal that can be harmful to Nafion and often a second or third pyrolysis.[17,27,31] These MNC catalysts can be broken down into three main categories: ammonia activated catalysts,[32,33] autogenic pressure generating catalysts,[34,35] and high-molecular-weight nitrogen precursor catalysts.[31,36] The ammonia activated catalysts are synthesized by purging the reactor with ammonia gas during the first pyrolysis. Normally these catalysts have a second pyrolysis under an inert atmosphere to increase durability. The autogenic pressure generating catalysts use nitrogen precursors that decompose during pyrolysis. The decomposition of the nitrogen precursors creates a high pressure of gaseous intermediates that react with the remaining solid phase to create active sites.[34,35,37] These catalysts were developed at Michigan State University and are the subject of Chapters 2-4. High molecular-weight nitrogen precursor catalysts are synthesized with nitrogen or metal-nitrogen precursors such as nicarbazim,[32] polyaniline,[31] or metal macrocycles.[38,39] These catalysts can be synthesized using an atmospheric-pressure, purged reactor without losing enough nitrogen precursor to hurt activity. One of these catalysts was developed at the University of New Mexico[32] and will be the subject of Chapter 5.

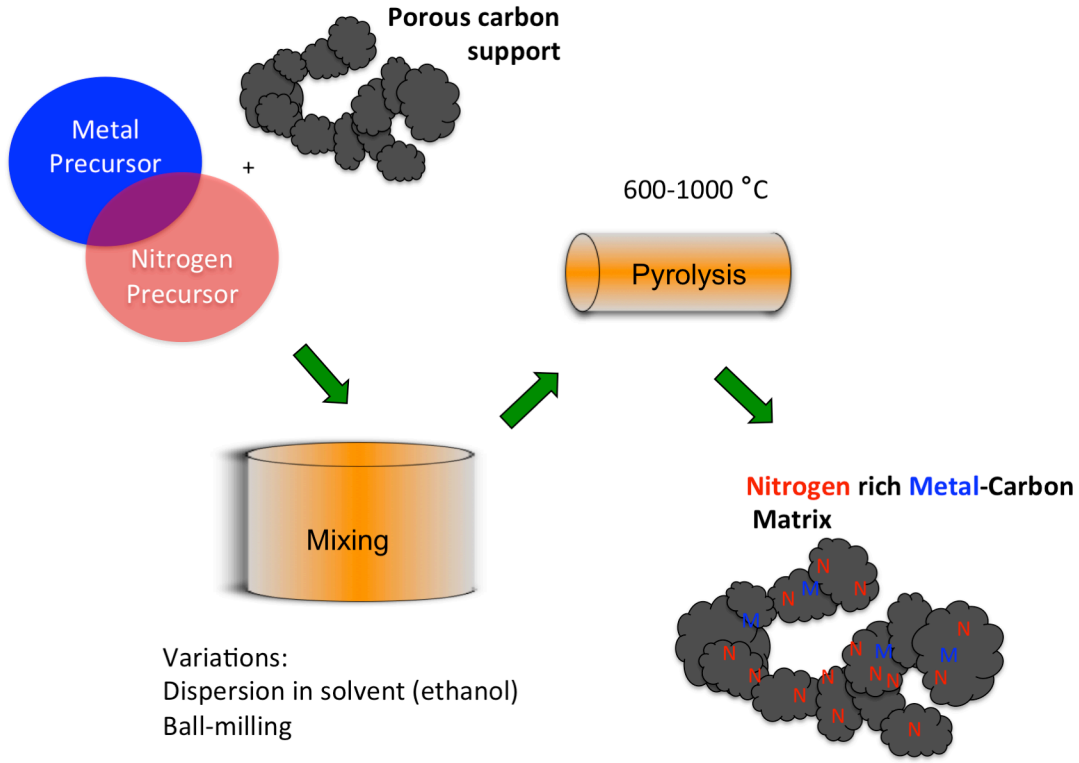

Figure 1.2: Synthesis of MNC catalysts

The current state of the art MNC catalyst is a high-molecular-weight MNC developed by Zelenay et al at Los Alamos National Laboratories.[31] For this catalyst, the carbon support, iron-salt, and short chain aniline oligomer are mixed. After the mixing, an oxidant is added to polymerize the aniline. The polymerization step is followed by a heat treatment in nitrogen at 900 °C, a leaching step in sulfuric acid, and a second heat treatment in nitrogen atmosphere.[31]

1.4. Methods and Fundamentals

1.4.1 Physical Characterization

The primary surface morphology techniques used in this dissertation consider porosity. We will consider porosimetry techniques based on nitrogen physisorption and mercury intrusion. The nitrogen physisorption analysis methods used in this dissertation are: non-local density functional theory (NLDFT); the Brunauer, Emmett, and Teller (BET) method (a method for

establishing specific surface area of a substance);[40] and the Barrett, Joyner, and Halenda (BJH) method (a method for establishing pore size distributions for pores larger than 2 nm).[41]

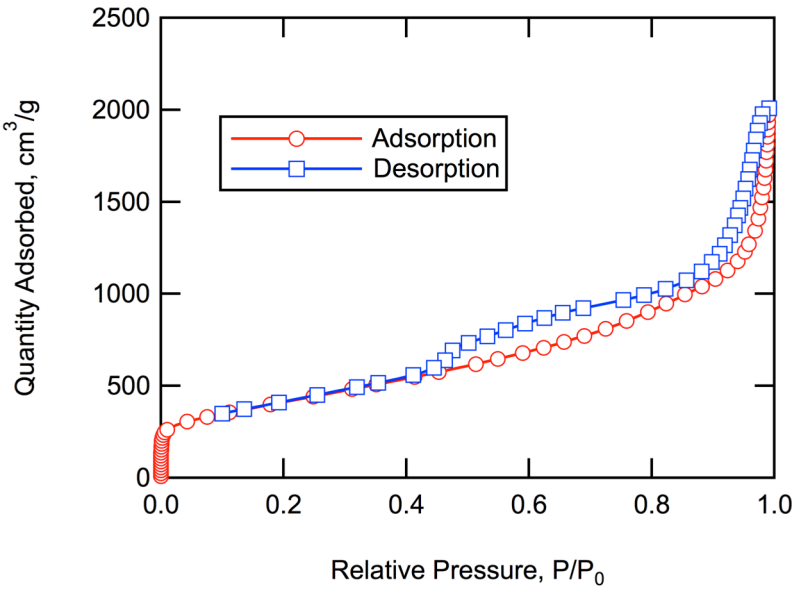

Figure 1.3: Typical Nitrogen Isotherm showing both adsorption and desorption curves on Ketjen EC 600J carbon black at 77 K.

All three nitrogen physisorption techniques are calculations based on adsorption isotherms. Figure 1.3 shows a typical isotherm of Ketjen EC 600J, a material commonly used in the synthesis of MNC catalysts. As the nitrogen pressure is increased at a constant temperature (generally 77 K), nitrogen molecules adsorb to the sample surface as the saturation pressure is approached. The BET surface area is based on a calculation of the volume of a single layer of nitrogen atoms on the sample surface, a monolayer. Essentially, it is assumed that molecules adsorb to the surface with one heat of adsorption, and that molecules adsorb to other adsorbed molecules with a different heat of adsorption. Calculation of equilibrium surface coverage based on Arrhenius adsorption laws as well as significant algebraic manipulation results in the BET equation:[41]

$$\frac{P/P_0}{Q(1-P/P_0)} = \frac{1}{cv_{\mathrm{m}}} + \frac{(c-1)P/P_0}{cv_{\mathrm{m}}} \quad [1]$$

where P is measured pressure, P_0 is saturation pressure, Q is measure adsorbed volume, v_{m} is monolayer volume, and c is a constant representing the ratio of adsorption energies for the first monolayer (adsorbent to surface) to the remaining monolayers (adsorbent to adsorbent). The left-hand side of Eq. 1 can be regressed with respected to P/P_0 in order to deduce v_{m} from the slope (S_{BET}) and intercept (J_{BET}):

$$v_{\mathrm{m}} = \frac{1}{S_{\mathrm{BET}} + J_{\mathrm{BET}}} \quad [2]$$

Then, given the size of the nitrogen atoms, a surface area can be calculated from the monolayer volume.[41]

BJH is a method of determining the pore size distribution over a relatively wide range spanning primarily the mesoporous region (~2-50nm).[42] In this method, the pore structure is modeled as a system of cylindrical pores. The pores associated with a specific diameter can be considered a single cylindrical pore with a given length. The method also assumes an initial condition where all pores are filled (i.e. at saturation pressure). As the pressure decreases, the critical pressures of the liquid phase nitrogen in the center of the pores are reached. Essentially, smaller, more confined pores allow the liquid nitrogen to be more stable decreasing the critical pressure. In this way, each decreasing pressure value can be associated with a certain pore radius. When the decreasing pressure reaches the critical value for a given pore size, the vaporization of the liquid nitrogen in the pore causes a decrease in adsorbed nitrogen shown in the desorption curve in Figure 1.3. BJH theory uses the Kelvin equation to model the relationship between observed vapor pressure, P, and pore of radius, r: [40]

$$RTln(P/P_0) = \frac{\gamma V}{r} \quad [3]$$

where R is the ideal gas constant, T is the absolute temperature, P_0 is the normal vapor pressure, V is molar volume, and γ is the surface tension. In this way desorption between two different pressures can be associated with vaporization of liquid in pores or a certain radius allowing the calculation of a pore size distribution.[40]

Surface area and pore size distribution information are also obtained using a non-local density functional theory (NLDFT) model for non-graphitic carbons developed by Ustinov.[43,44] In this approach, density functions for various pore sizes and pressures were obtained by minimizing the grand thermodynamic potential, Ω, as a function of local density. ρ:

$$\Omega = \int \rho[f(x,\rho,\rho_{\mathrm{m}}) + u^{\mathrm{ext}}(x) - \mu]dx \quad [4]$$

where u_{ext} is the external potential exerted by the solid, μ is the chemical potential, and f is the local molar Helmholtz free energy. The Helmholtz free energy is a function of position, x; local density, ρ; and smoothed density, ρ_{m}. Ustinov calculated molecular parameters from nitrogen adsorption on a non-graphitized carbon black (BP 280) and incorporated these parameters in the energy equation to find density as a function of pressure. The minimization of Eq. for various pore sizes and pressures, allows a mean density to be calculated. This kernel of density as it varies with pressure and pore size can be used to deconvolute an adsorption isotherm into adsorption associated with specific pore sizes. The total adsorption, Q as a function of pressure, P, is:

$$Q(P) = \sum_i \rho_{\mathrm{m,i}}|_{\mathrm{P}} v_i \quad [5]$$

where $\rho_{m,i}|_P$ is the mean density in the *i*th pore at pressure, *P*, and v_i is volume of the *i*th pore. The set of *v* is the discretized pore size distribution.

So far the porosity techniques have only considered pores smaller than about 300nm diameter. Larger pores are generally measured with mercury intrusion porosimetry (MIP). In this method, mercury is forced into pores by increasing pressure. As the pressure increases, mercury is forced into increasingly smaller pores. This phenomenon is governed by the surface energy of mercury via by Washburn's equation:[45]

$$r_c = \frac{-2\gamma cos(\theta)}{P_c} \quad [6]$$

where P_c is the mercury pressure, γ is the surface tension, theta is the contact angle, and r_c is the pore radius. Using the consistent surface properties of mercury a pore size distribution is calculated.

1.4.2 Electrochemical Characterization

A number of electrochemical methods will be useful for understanding this dissertation: linear sweep voltammetry (LSV), cyclic voltammetry (CV), rotating disc electrode (RDE), and rotating ring-disc electrode (RRDE). Both LSV and CV are electrochemical methods in which the potential is varied and the current is allowed to respond using a three electrode system.[46] A three-electrode system consists of a working, counter, and reference electrode. The reaction of interest occurs at the working electrode, while a second reaction is required for charge neutrality at the counter electrode. To eliminate the impact of ohmic and kinetic potential drops across the counter electrode, a third electrode is required. The third electrode is the reference: it contains a known electrochemical reaction. Measuring the potential of the working electrode with respect to the equilibrium potential of the reference electrode reaction eliminates the impact of the counter

electrode. The main difference between LSV and CV is that CV consists of multiple potential sweeps between two potentials. A typical voltammetry curve consists of three main sections. If one starts at open circuit (on the right side of Fig. 1.2), it begins with a section in which there is no faradaic current because the electric field at the electrode surface is not large enough to drive the reaction. Eventually, as the potential sweeps farther from open circuit (middle of Fig. 1.2), the electric field at the electrode surface becomes large enough to drive the reaction. Initially this over-potential is small and results the reaction being limited by the kinetics of the electrochemical reaction. Eventually the reaction rate increases to the extent that the electrode surface becomes depleted of reactant molecules (left side of Fig. 1.2). At this point the reaction becomes limited by the ability of the reactant to diffuse to the electrode surface. As the reactant is depleted from the surface, the surface concentration approaches zero. When the surface concentration is essentially zero, the reaction rate is governed by the rate at which the reactant can diffuse to the surface, and the current becomes independent of potential. These three regions will now be covered in detail.

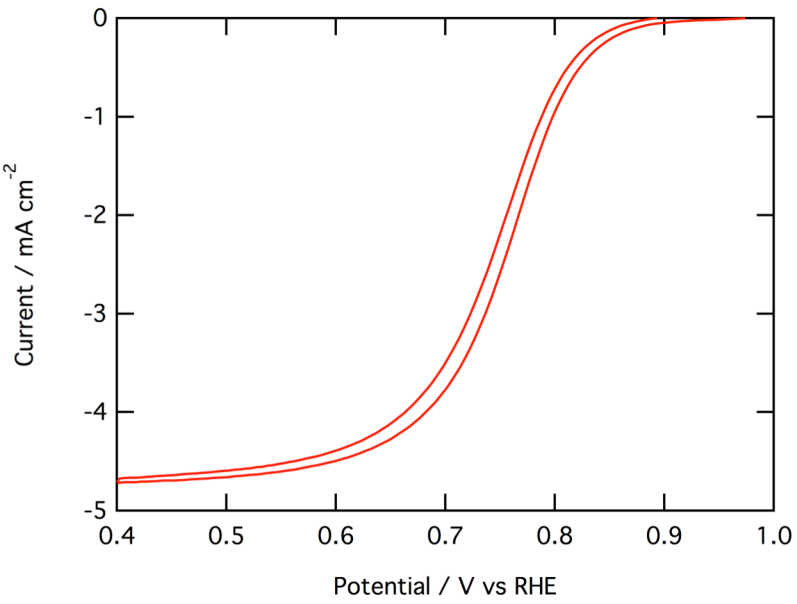

Figure 1.4: Typical cyclic voltammogram for a reduction reaction.

Although the primary parameter of interest for electrocatalysts is current, the open circuit potential can also give information about the catalyst. The open circuit potential is the result of equilibrium between the forward and reverse reactions (for this work the forward reaction is a reduction reaction and the reverse reaction is oxidation) resulting in zero net current. This equilibrium is considered using Gibbs free energy and results in the Nernst Equation. If we consider currents to be reversible, we can express a change in Gibbs free energy, G, as a charge passed over a reversible potential, E:[46]

$$\Delta G = -nFE \qquad [7]$$

where n is the number of electrons per molecule, and F is Faraday's constant representing charge per mole electron. A reference Gibbs free energy is defined This is generally defined as a standard free energy and reversible potential when all substances are 1 M. Activity is measure of

chemical availability and is generally considered to be to molarity. When substances are no longer present at unit activity, the chemical potential can be considered:

$$\Delta G = \Delta G^0 + RTln(a) \quad [8]$$

where the superscript 0 refers to standard values, R is the ideal gas constant, T is the temperature, and a is activity. Activity is the availability of a constituent relative to 1 M concentration or 1 atmosphere partial pressure. A reference Gibbs free energy is defined when all constituents have unit activity. In terms of the potential this becomes the Nernst Equation:[46]

$$E = E^0 + \frac{RT}{nF} ln(\frac{a_{\mathrm{ox}}}{a_{\mathrm{red}}}) \quad [9]$$

where the potential is a function of the ideal gas constant, R; the temperature, T; and the activity of the oxidant and reductant, a_{ox} and a_{red} respectively.

When the polarization curve moves to non-equilibrium regions, a new kinetic model is used. In these cases, one of the most general kinetic models is Butler-Volmer. This model assumes that forward and reverse reaction rates follow an Arrhenius form: [46]

$$k = A \exp(-\Delta G/RT) \quad [10]$$

where the reaction rate, k, is a function of some pre-exponential, A, and some energy barrier, ΔG. Considering Eq. 7 and 9, these reaction rates can be considered in terms of potential: [46]

$$k = k_0 \exp((E^0 - E)\alpha F/RT) \quad [11]$$

where k_0 is some equilibrium rate constant, and α is an exchange coefficient that represents some fraction of the activation barrier. When we consider both an oxidation and reduction reaction rate constant, the rate, expressed as a current is the Butler-Volmer Equation: [46]

$$i = nFk_0[C_{\text{ox}} \exp(-\alpha(E - E^0)F/RT) - C_{\text{red}} \exp((1-\alpha)(E - E^0)F/RT)] \quad [12]$$

where the current density, i, is a function of a rate constant, k_0 and concentrations at the surface for oxidant, C_{ox}, and reductant, C_{red}. Note that the nF converts the rate to a current. Often it is assumed that the reaction is symmetrical, meaning that the potential deviation equally affects the anodic and cathodic branches resulting in an exchange coefficient is 0.5. An approximation of this kinetic model is Tafel kinetics in which it is assumed one branch is much slower than the other branch, that is:

$$C_{\text{ox}} \exp(-\alpha f(E - E^0)) \gg C_{\text{red}} \exp((1-\alpha) f(E - E^0)) \quad [13]$$

or vise versa. In this case, the Butler-Volmer expression simplifies to: [46]

$$i = nFk_0 C \exp(-\alpha f(E - E^0)) \quad [14]$$

This equation is the Tafel equation, and results in an exponential relationship between potential and current. This Tafel relationship allows for quick and easy identification of kinetically limited regions of polarization curves.

A second aspect of these electrochemical characterization techniques is how the basic technique (LSV, CV, etc.) is incorporated applied to specific chemistry, electrode design, and transport system. For this dissertation, the chemistry will generally be oxygen reduction, and thorough discussion is included in Chapter 4. The oxygen reduction reaction (ORR) can follow two different pathways (Fig. 1.5).[47-52] The first pathway is direct four-electron reduction to water without a desorbing intermediate (k_1 in Fig. 1.5). The second pathway is incomplete reduction of oxygen to hydrogen peroxide (k_2). The hydrogen peroxide can desorb from the surface ($K_{P,2}$),[47] disproportionate to water and oxygen,[49] or reduce to water (k_3).[49]

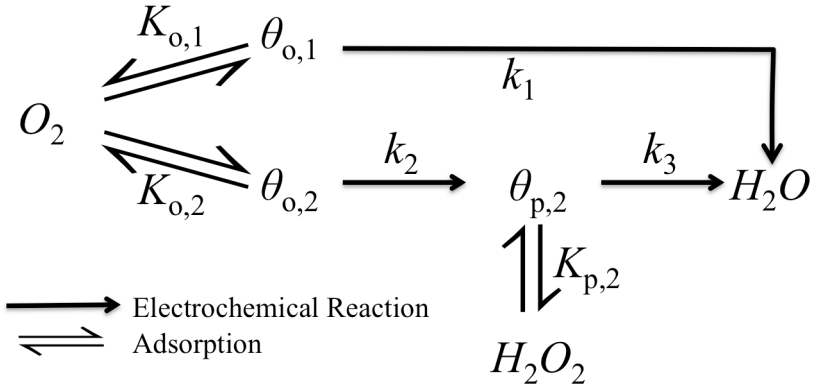

Figure 1.5: Reaction schematic showing two pathways: pathway one ($K_{o,1}$ and k_1) is the complete reduction of oxygen to water with no desorbing intermediate and pathway two ($K_{o,2}$ and k_2) is the two-electron reduction to a desorbing peroxide intermediate that disperses into the catalyst layer ($K_{p,2}$), but also has the potential to be further reduced to water (k_3).

To return to the explanation of electrochemical characterization techniques, one commonly used system is rotating disk electrode (RDE). As shown in Figure 1.6, the system consists of a rotating, glassy-carbon, working electrode with a layer of catalyst on it, a reference electrode, and platinum counter electrode in an acidic solution. Oxygen is bubbled into the solution to ensure that the bulk oxygen concentration in the electrolyte remains at saturation. The protons are supplied by the acidic solution, but charge neutrality is conserved due to the reaction at the counter electrode. Essentially, the drag caused by the rotation of the disk induces a radial flow of electrolyte at the surface. The centrifugal acceleration causes a flux radially away from the disk center and axially towards the disk as shown in Fig. 1.6. In this way the rotation of the working electrode allows LSV or CV with controllable diffusion limitations.[46,53,54] Rotating ring-disk electrodes (RRDEs) are also used extensively in this work. In the RRDE system, a second working electrode is used. This fourth electrode is a concentric ring around the disk, and any by-

products resulting from reactions at the disk pass the ring electrode due to flow field in the system.[46,47]

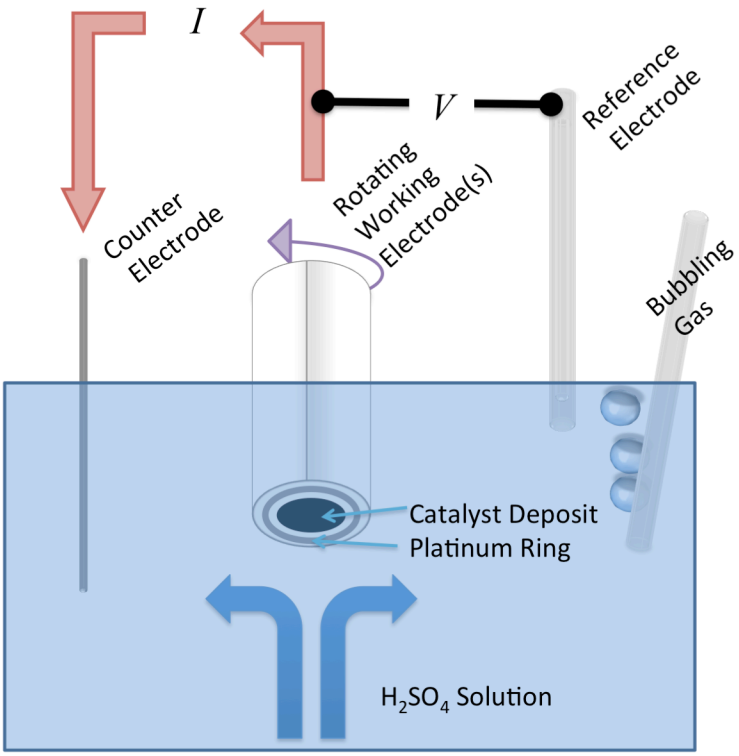

Figure 1.6: Rotating Ring-Disc Electrode Experimental Set-up

Due to the complexity involved in Chapter 4, this introduction will cover the transport environment surrounding RDEs and RRDEs in more detail. The diffusion limitations are well known via the Levich equation.[53] Although a complete derivation of the Levich equation is outside of the scope of this introduction, an explanation and discussion will suffice. The full derivation is well documented.[53,54] Initially, the flow field around the disk is calculated from a solution to the Navier-Stokes equations in the electrolyte surrounding the disk. It is assumed that there is a no-slip boundary condition at the electrode surface and that the electrolyte is stagnant and large distances from the disk. The hydrodynamic boundary layer has a thickness, δ_0:[53,54]

$$\delta_0 = 3.6\sqrt{\nu/\omega} \quad [15]$$

Using the flow field and solution to the convective diffusion equation can be found. The boundary conditions consist of some concentration at the surface and some bulk concentration at distances far from the disk. This solution allows the concentration to be written as a function of velocity and position and results in a diffusion boundary layer, δ_D:[53,54]

$$\delta_D = 1.61 D^{1/3} \nu^{1/6} \omega^{-1/2} \quad [16]$$

where D is a diffusivity, ν is viscosity, and ω is rotation speed. A comparison of the hydrodynamic and diffusion boundary layers shows that the diffusion layer thickness is about 6% of the hydrodynamic layer thickness for oxygen in water (viscosity of 0.01 cm^2/s and oxygen diffusivity of 2×10^{-5} cm^2/s): [55,56]

$$\frac{\delta_D}{\delta_0} = 0.45 \frac{D^{1/3}}{\nu^{1/3}} \quad [17]$$

The relative thinness of the diffusion boundary layer ensures that diffusion dominates mass transport near the electrode surface. Assuming Fickian diffusion near the surface, a relationship between current, *i*, and concentration at the surface, C_s can be found:[47,48,51]

$$i = nFD \frac{(C_s - C_b)}{\delta_D} \quad [18]$$

where C_b is the bulk concentration. This relationship is the foundation for Chapter 4, and allows the R(R)DE system to be useful in isolating a catalyst's performance from transport considerations. By setting the surface concentration to zero and combining Eqs. 16 and 18, the Levich equation is obtained:[47,48,51]

$$i_{mt} = 0.62 nF D^{2/3} \nu^{-1/6} \omega^{1/2} C_b \quad [19]$$

The Levich equation calculates the mass transfer limiting current, i_{mt}, in a RDE system.

The second important transport system in this dissertation is a membrane electrode assembly (MEA). This transport system is important to the oxygen reduction reaction because it represents the intended application of these catalysts. The MEA system, shown in Fig. 1.1d, allows the transport of protons and oxygen to active sites in a conductive solid network. A further transport consideration is the egress of water from the MEA. The transport of protons as well as the electric current network are generally considered using Ohm's law in which the current, *i*, is proportional to the gradient of the electric field:[57]

$$i = \kappa \nabla V \qquad [20]$$

where V is potential and κ is conductivity. The proton flux represents a current through the electrolyte phase of the MEA. Besides ohmic considerations there are also mass transport considerations for gas and liquid species. In the gas phase, multi-component diffusion must be considered due to the presence of oxygen, nitrogen, and water vapor. The flux of these components is dependent on their concentrations and is often considered with Stefan-Maxwell diffusion which accounts for momentum conservation of randomly colliding gas molecules:[57]

$$\nabla x_{\mathrm{i}} = \sum_{\mathrm{i} \neq \mathrm{j}} \frac{N_{\mathrm{i}} x_{\mathrm{j}} - N_{\mathrm{j}} x_{\mathrm{i}}}{c D_{\mathrm{ij}}} \qquad [21]$$

where the vapor fraction of constituent *i*, x_{i}, is related to the fluxes, N, and gas phase concentration, c, as well as binary diffusivity between constituent *i* and *j*, D_{ij}. The liquid phase is generally considered pure water, and the Hagen-Poiseuille equation relates the liquid flux, N_{L} to the pressure gradient:[57]

$$N_{\mathrm{L}} = -\frac{k}{\mu} \nabla P_{\mathrm{L}} \qquad [22]$$

where k is permeability, μ is viscosity, and P_L is pressure in the liquid phase. Because understanding the transport requires the deconvolution of the impact of four different phases, MEA results are not necessarily very useful in understanding catalyst kinetics. This complexity is why RDE results are so useful as shown in Chapter 4. On the other hand, the importance of the MEA results to catalyst application requires full understanding. This MEA transport understanding is the goal of Chapter 5.

REFERENCES

REFERENCES

1. *International Energy Outlook 2014,* (ed. Doman, L.), U.S. Energy Information Administration, DOE/EIA-0484(2014) (2014). <http://www.eia.gov/forecasts/ieo/>

2. *World Population Prospects: The 2012 Revision,* Population Division of the Department of Economic and Social Affairs of the United Nations Secretaria, (2012). < http://esa.un.org/unpd/wpp/index.htm >

3. *Mitigation of Climate Change: Technical Summary,* Intergovenmental Panel on Climate Change, (2014).

4. K.-D. Kreuer, *Fuel Cells: Selected Entries from the Encyclopedia of Sustainability Science and Technology,*(Springer, 2012).

5. J. Larminie and A. Dicks, *Fuel cell systems explained,*(J. Wiley, New York, 2003).

6. A. Serov and C. Kwak, "Direct hydrazine fuel cells: A review," *Applied Catalysis B: Environmental,* **98**(1), 1-9 (2010).

7. M. K. Debe, "Electrocatalyst approaches and challenges for automotive fuel cells," *Nature,* **486**(7401), 43-51 (2012).

8. N. Leonard, V. Nallathambi and S. C. Barton, "Carbon Supports for Non-Precious Metal Oxygen Reducing Catalysts," *Journal of the Electrochemical Society,* **160**(8), F788-F792 (2013). doi:10.1149/2.026308jes

9. N. D. Leonard and S. C. Barton, "Analysis of Adsorption Effects on a Metal-Nitrogen-Carbon Catalyst Using a Rotating Ring-Disk Study," *Journal of The Electrochemical Society,* **161**(13), H3100-H3105 (2015).

10. N. D. Leonard, S. Ganesan, V. Nallathambi and S. C. Barton, "Alkalinity of Non-Precious Metal Catalysts for Oxygen Reduction," *ECS Transactions,* **50**(2), 1869-1873 (2013).

11. J. R. Varcoe and R. C. Slade, "Prospects for Alkaline Anion‐Exchange Membranes in Low Temperature Fuel Cells," *Fuel cells,* **5**(2), 187-200 (2005).

12. G. F. McLean, T. Niet, S. Prince-Richard and N. Djilali, "An assessment of alkaline fuel cell technology," *International Journal of Hydrogen Energy,* **27**(5), 507-526 (2002). doi:10.1016/S0360-3199(01)00181-1

13. J. R. Varcoe, P. Atanassov, D. R. Dekel, A. M. Herring, M. A. Hickner, P. A. Kohl, A. R. Kucernak, W. E. Mustain, K. Nijmeijer, K. Scott, T. Xu and L. Zhuang, "Anion-exchange membranes in electrochemical energy systems," *Energy & Environmental Science,* **7**(10), 3135-3191 (2014). doi:10.1039/C4EE01303D

14. "FUEL CELL R&D ACTIVITIES," http://energy.gov/eere/fuelcells/fuel-cell-rd-activities, accessed 10/28.

15. B. Han, C. E. Carlton, A. Kongkanand, R. S. Kukreja, B. R. Theobald, L. Gan, R. O'Malley, P. Strasser, F. T. Wagner and Y. Shao-Horn, "Record activity and stability of dealloyed bimetallic catalysts for proton exchange membrane fuel cells," *Energy & Environmental Science* (2014).

16. C. Wang, N. M. Markovic and V. R. Stamenkovic, "Advanced Platinum Alloy Electrocatalysts for the Oxygen Reduction Reaction," *ACS Catalysis,* **2**(5), 891-898 (2012). doi:10.1021/cs3000792

17. F. Jaouen, J. Herranz, M. Lefevre, J.-P. Dodelet, U. I. Kramm, I. Herrmann, P. Bogdanoff, J. Maruyama, T. Nagaoka, A. Garsuch, J. R. Dahn, T. Olson, S. Pylypenko, P. Atanassov and E. A. Ustinov, "Cross-Laboratory Experimental Study of Non-Noble-Metal Electrocatalysts for the Oxygen Reduction Reaction," *ACS Applied Materials & Interfaces,* **1**(8), 1623-1639 (2009). doi:10.1021/am900219g

18. E. Yeager, "Electrocatalysts for O-2 Reduction," *Electrochimica Acta,* **29**(11), 1527-1537 (1984). doi:10.1016/0013-4686(84)85006-9

19. Y. Feng, A. Gago, L. Timperman and N. Alonso-Vante, "Chalcogenide metal centers for oxygen reduction reaction: Activity and tolerance," *Electrochimica Acta,* **56**(3), 1009-1022 (2011). doi:10.1016/j.electacta.2010.09.085

20. H. Peng, Z. Mo, S. Liao, H. Liang, L. Yang, F. Luo, H. Song, Y. Zhong and B. Zhang, "High Performance Fe- and N- Doped Carbon Catalyst with Graphene Structure for Oxygen Reduction," *Sci. Rep.,* **3** (2013). doi:10.1038/srep01765

21. F. Hasché, M. Oezaslan and P. Strasser, "Activity, structure and degradation of dealloyed PtNi3 nanoparticle electrocatalyst for the oxygen reduction reaction in PEMFC," *Journal of The Electrochemical Society,* **159**(1), B24-B33 (2011).

22. P. Strasser, S. Koh, T. Anniyev, J. Greeley, K. More, C. Yu, Z. Liu, S. Kaya, D. Nordlund, H. Ogasawara, M. F. Toney and A. Nilsson, "Lattice-strain control of the activity in dealloyed core-shell fuel cell catalysts," *Nat Chem,* **2**(6), 454-60 (2010). doi:10.1038/nchem.623

23. *Nanosegregated Cathode Alloy Catalysts with Ultra-Low Platinum Loading,* DOE Hydrogen and Fuel Cells Program, (2013).

24. *DOE Hydrogen Program- 2008 Annual Progress Report,* United States Department of Energy, (2008). <http://www.hydrogen.energy.gov/annual_progress08.html>

25. R. Jasinski, "A New Fuel Cell Cathode Catalyst," *Nature,* **201**(4925), 1212-1213 (1964).

26. S. Gupta, D. Tryk, I. Bae, W. Aldred and E. Yeager, "Heat-Treated Polyacrylonitrile-Based Catalysts for Oxygen Electroreduction," *Journal of Applied Electrochemistry,* **19**(1), 19-27 (1989).

27. F. Jaouen, E. Proietti, M. Lefèvre, R. Chenitz, J.-P. Dodelet, G. Wu, H. T. Chung, C. M. Johnston and P. Zelenay, "Recent advances in non-precious metal catalysis for oxygen-reduction reaction in polymer electrolyte fuel cells," *Energy & Environmental Science,* **4**(1), 114 (2011). doi:10.1039/c0ee00011f

28. H. T. Chung, C. M. Johnston, K. Artyushkova, M. Ferrandon, D. J. Myers and P. Zelenay, "Cyanamide-derived non-precious metal catalyst for oxygen reduction," *Electrochemistry Communications,* **12**(12), 1792-1795 (2010). doi:10.1016/j.elecom.2010.10.027

29. A. Serov, M. H. Robson, M. Smolnik and P. Atanassov, "Templated bi-metallic non-PGM catalysts for oxygen reduction," *Electrochimica Acta,* **80**(0), 213-218 (2012). doi:10.1016/J.Electacta.2012.07.008

30. V. Nallathambi, N. Leonard, W. Patterson, K. Artyushkova, P. Atanassov and S. C. Barton, "Ammonia-Generating Precursors in MNC Electrocatalysts for Oxygen Reduction," *Meeting Abstracts*(16), 1150-1150 (2011).

31. R. Bashyam and P. Zelenay, "A class of non-precious metal composite catalysts for fuel cells," *Nature,* **443**(7107), 63-66 (2006). doi:10.1038/nature05118

32. E. Proietti, F. Jaouen, M. Lefevre, N. Larouche, J. Tian, J. Herranz and J. P. Dodelet, "Iron-based cathode catalyst with enhanced power density in polymer electrolyte membrane fuel cells," *Nature communications,* **2**, 416 (2011). doi:10.1038/ncomms1427

33. M. Lefevre, E. Proietti, F. Jaouen and J. P. Dodelet, "Iron-Based Catalysts with Improved Oxygen Reduction Activity in Polymer Electrolyte Fuel Cells," *Science,* **324**(5923), 71-74 (2009). doi:10.1126/science.1170051

34. R. Kothandaraman, V. Nallathambi, K. Artyushkova and S. C. Barton, "Non-precious oxygen reduction catalysts prepared by high-pressure pyrolysis for low-temperature fuel cells," *Applied Catalysis B Environmental,* **92**(1-2), 209-216 (2009). doi:10.1016/J.Apcatb.2009.07.005

35. V. Nallathambi, J. W. Lee, S. P. Kumaraguru, G. Wu and B. N. Popov, "Development of high performance carbon composite catalyst for oxygen reduction reaction in PEM Proton Exchange Membrane fuel cells," *Journal of Power Sources,* **183**(1), 34-42 (2008). doi:10.1016/j.jpowsour.2008.05.020

36. A. Serov, K. Artyushkova and P. Atanassov, "Fe-N-C Oxygen Reduction Fuel Cell Catalyst Derived from Carbendazim: Synthesis, Structure, and Reactivity," *Advanced Energy Materials,* **4**(10), n/a-n/a (2014). doi:10.1002/aenm.201301735

37. V. Nallathambi, N. Leonard, R. Kothandaraman and S. Calabrese Barton, "Nitrogen Precursor Effects in Iron-Nitrogen-Carbon Oxygen Reduction Catalysts," *Electrochemical and Solid State Letters,* **14**(6), B55-B58 (2011). doi:10.1149/1.3566065

38. S. Maldonado and K. J. Stevenson, "Direct preparation of carbon nanofiber electrodes via pyrolysis of iron(II) phthalocyanine: Electrocatalytic aspects for oxygen reduction," *Journal of Physical Chemistry B,* **108**(31), 11375-11383 (2004). doi:10.1021/Jp0496553

39. P. Bogdanoff, I. Herrmann, M. Hilgendorff, I. Dorbandt, S. Fiechter and H. Tributsch, "Probing structural effects of pyrolysed CoTMPP-based electrocatalysts for oxygen reduction via new preparation strategies," *Journal of New Materials for Electrochemical Systems,* **7**(2), 85-92 (2004).

40. S. Brunauer, P. H. Emmett and E. Teller, "Adsorption of Gases in Multimolecular Layers," *Journal of the American Chemical Society,* **60**(2), 309-319 (1938). doi:10.1021/ja01269a023

41. E. P. Barrett, L. G. Joyner and P. P. Halenda, "The Determination of Pore Volume and Area Distributions in Porous Substances. I. Computations from Nitrogen Isotherms," *Journal of the American Chemical Society,* **73**(1), 373-380 (1951). doi:10.1021/ja01145a126

42. F. Jaouen, S. Marcotte, J.-P. Dodelet and G. Lindbergh, "Oxygen Reduction Catalysts for Polymer Electrolyte Fuel Cells from the Pyrolysis of Iron Acetate Adsorbed on Various Carbon Supports," *The Journal of Physical Chemistry B,* **107**(6), 1376-1386 (2003). doi:10.1021/jp021634q

43. E. A. Ustinov, D. D. Do and V. B. Fenelonov, "Pore size distribution analysis of activated carbons: Application of density functional theory using nongraphitized carbon black as a reference system," *Carbon,* **44**(4), 653-663 (2006). doi:10.1016/j.carbon.2005.09.023

44. E. A. Ustinov, "Nitrogen Adsorption on Silica Surfaces of Nonporous and Mesoporous Materials," *Langmuir,* **24**(13), 6668-6675 (2008). doi:10.1021/la704011z

45. A. W. Adamson and A. P. Gast, *Physical chemistry of surfaces,*(Wiley, New York, 1997).

46. A. J. Bard and L. R. Faulkner, *Electrochemical methods : fundamentals and applications,*(John Wiley, New York, 2001).

47. N. A. Anastasijevic, V. Vesovic and R. R. Adzic, "Determination of the kinetic parameters of the oxygen reduction reaction using the rotating ring-disk electrode: Part I. Theory," *Journal of Electroanalytical Chemistry and Interfacial Electrochemistry,* **229**(12), 305-316 (1987). doi:10.1016/0022-0728(87)85148-3

48. N. Anastasijević, V. Vesović and R. Adžić, "Determination of the kinetic parameters of the oxygen reduction reaction using the rotating ring-disk electrode: Part II. Applications," *Journal of electroanalytical chemistry and interfacial electrochemistry,* **229**(1), 317-325 (1987).

49. F. Jaouen, "O2 Reduction Mechanism on Non-Noble Metal Catalysts for PEM Fuel Cells. Part II: A Porous-Electrode Model To Predict the Quantity of H2O2 Detected by Rotating Ring-Disk Electrode," *The Journal of Physical Chemistry C,* **113**(34), 15433-15443 (2009).

50. H. S. Wroblowa, P. Yen Chi and G. Razumney, "Electroreduction of oxygen: A new mechanistic criterion," *Journal of Electroanalytical Chemistry and Interfacial Electrochemistry,* **69**(2), 195-201 (1976). doi:10.1016/S0022-0728(76)80250-1

51. K. L. Hsueh, D. T. Chin and S. Srinivasan, "Electrode kinetics of oxygen reduction: A theoretical and experimental analysis of the rotating ring-disc electrode method," *Journal of Electroanalytical Chemistry and Interfacial Electrochemistry,* **153**(1), 79-95 (1983). doi:10.1016/S0022-0728(83)80007-2

52. A. Damjanovic, M. A. Genshaw and J. O. M. Bockris, "The Role of Hydrogen Peroxide in the Reduction of Oxygen at Platinum Electrodes," *The Journal of Physical Chemistry,* **70**(11), 3761-3762 (1966). doi:10.1021/j100883a515

53. V. G. Levich, *Physicochemical Hydrodynamics,*(Prentice-Hall, Englewood Cliffs, NJ, 1962).

54. Y. V. Pleskov and V. Y. Filinovski, *The Rotating Disc Electrode,*(Consultants Bureau, New York, 1976).

55. K. E. Gubbins and R. D. Walker, "The solubility and diffusivity of oxygen in electrolytic solutions," *Journal of The Electrochemical Society,* **112**(5), 469-471 (1965).

56. W. M. Haynes (ed.) *CRC Handbook of Chemistry and Physics* (CRC Press, 2010).

57. A. Z. Weber and J. Newman, "Modeling Transport in Polymer-Electrolyte Fuel Cells," *Chemical Reviews,* **104**(10), 4679-4726 (2004).

Chapter 2 Carbon Supports for Non-precious Metal Oxygen Reducing Catalysts

2.1 Abstract

Porous carbon materials with varying structural and compositional properties were studied for their impact on the nitrogen content and activity of metal-nitrogen-carbon (MNC) oxygen reduction catalysts prepared using high-pressure pyrolysis. The carbon materials and resulting catalysts were characterized morphologically using nitrogen physisorption, coupled with non-local density functional theory (NLDFT) analysis to calculate pore size distributions. Graphiticity was assessed via X-ray Diffraction (XRD), bulk nitrogen content was observed using CHN combustion analysis and iron content by Inductively Coupled Plasma (ICP). The catalysts were characterized electrochemically using rotating ring-disk measurements. The results indicate that substrates adsorbing the most nitrogen and iron show the highest activity. Furthermore, a relationship found between mesoporosity and nitrogen adsorption indicate the importance of transport of precursors to potential active sites.

2.2 Introduction

The cost of precious metals has driven the search for lower-cost alternatives to catalyze the oxygen reduction reaction (ORR) and accelerate commercialization of low-temperature fuel cells. An important class of non-precious metal catalysts for oxygen reduction is pyrolyzed metal/nitrogen/carbon (MNC) compounds.[1-3] These compounds involve the association of metal atoms with nitrogen moieties immobilized in a conductive carbon matrix. Recent research has lead to increased understanding of key aspects of catalyst activation, function, and stability. However, the nature of the active site is not yet clear because of the complexities introduced by pyrolysis on high surface-area supports. Such lack of understanding has hindered the engineering and implementation of these catalysts in fuel cell applications.

Dodelet et al. suggest that MNC catalytic sites occur where metal atoms are bridge-bonded to nitrogen sites and span micropores of width less than 2 nm.[4,5] Lefevre et al. also hypothesize that high temperature ammonia etching of micropores during pyrolysis creates potential catalytic site hosts.[6] Although microporosity can have a significant impact on activity, species transport to reactive sites occurs most efficiently through mesopores. This suggests that, for geometrically complex materials, mesoporosity will have a significant impact on the apparent catalyst activity.[7-9]

Although a number of MNC catalyst synthesis methods have been reported, including ammonia etching [10] and ion sputtering,[11] this work considers a high-pressure, closed-vessel pyrolysis.[1,12] Precursors are pre-mixed and vacuum-sealed in a quartz vial so that the process pressure is elevated by evaporation and decomposition of volatile precursors.[1] Precursor retention in the closed vessel and high partial pressures of reaction intermediates leads to increased catalyst activity.

The present work considers the impact of varying the carbon black substrate on resulting nitrogen and iron content, and catalyst activity. Melamine and Iron acetate were selected as nitrogen and iron precursors respectively consistent with our previous work,[12] in which high nitrogen to carbon ratios are shown to improve activity. Nitrogen and iron content were also kept the same: 6.3 wt% and 1 wt% respectively. This composition was previously found to lead to optimum ORR current density (data not shown). The carbons used are Ketjen EC 600J, Black Pearls 2000, Norit SX Ultra, and Vulcan XC 72R. These carbons were selected to examine a wide variety of pore distributions, from Vulcan with little porosity of any size, to Black Pearls with substantial mesoporosity (2-50 nm scale pores) and microporosity (<2 nm pores). Norit is a primarily microporous activated carbon, and Ketjen is a primary mesoporous carbon black.[4,6,13]

A number of works have explored porosity in MNC catalysts.[6,14-16] These articles have primarily observed the importance of microporosity on catalyst synthesis and etching by nitrogen precursors, particularly ammonia. To add to the previous body of work, the current study evaluates the impact of mesoporosity on catalyst properties. A correlation between mesoporosity, nitrogen content, and activity was identified, indicating the importance of mesoporosity for transport of reactants during both active site synthesis and ORR catalysis.

2.3 Experimental

2.3.1 Materials

Iron (II)-acetate, melamine, Nafion® solution (5 wt%) and sulfuric acid (ACS grade) were obtained from Alfa Aesar (Ward Hill, MA). Ketjenblack® 600JD carbon black was obtained from Akzo Nobel (Chicago, IL). Black Pearls 2000 and Vulcan XC72R carbon blacks were obtained from Cabot Corporation (Boston, MA). Norit SX Ultra activated carbon was obtained from Norit Americas (Marshall, TX). Pressurized oxygen cylinders were obtained from Airgas (Lansing, MI). All materials were used as received. 190 Proof Ethanol was obtained from Koptec (King of Prussia, PA)

2.3.2 Catalyst Synthesis

7.5 mg Melamine, 31 mg iron acetate, and 850 mg of various carbons were dispersed in ethanol, which was evaporated under continuous stirring to yield a dry powder. Melamine was added to the powder to obtain a mass ratio of 6.3 wt% Nitrogen, and the mixture was inserted into a quartz ampule that was then flame sealed under vacuum. The ampule was subjected to heat treatment at 800°C for three hours. After pyrolysis, the quartz ampule was broken under ventilation, releasing a quantity of gas with an ammonia odor. The remaining powder was then poured out of the opened ampule.

2.3.3 Physical Characterization

Surface area and pore size distribution were obtained using a Micromeretics ASAP 2020 Surface Area and Porosity Analyzer. Nitrogen adsorption isotherms at 77 K were measured. The Brunauer, Emmett, and Teller (BET)[17] surface area calculation, Barrett, Joyner, and Halenda (BJH)[18] pore volume calculation and non-local density functional theory (NLDFT) were used to analyze the isotherms. The NLDFT model is a non-graphitic model developed by Ustinov.[19,20] Catalyst nitrogen content was evaluated by carbon hydrogen nitrogen (CHN) analysis (Midwest Microlab, Indianapolis, IN). Iron content was measured using the inductively coupled plasma (ICP) technique (Michigan State University Department of Geological Sciences, MI). X-ray diffraction (XRD) spectra of MNC catalysts obtained using a Bruker AXS Model D8 Advance diffractometer with Cu Kα radiation (λ = 1.54 Å). Thermogravimetric analysis (TGA) results were obtained using a TGA Q50 (TA instruments). Temperature was scanned at 5 °C min^{-1} below 450 °C and 20 °C min^{-1} from 450 to 850 °C. Chemical characterization of TGA products was obtained using a JSM 6610LV Scanning Electron Microscope (SEM) from JEOL with energy dispersive X-ray spectrometer (EDS) with acceleration voltage set to 8 kV.

2.3.4 Electrode Preparation

Catalyst ink was prepared by dispersing 4 mg of the catalyst powder ultrasonically in a solution mixture containing 150 μL ethanol and 50 μL Nafion® (5 wt% solution). A catalyst loading of 0.5 mg cm^{-2} was achieved by depositing 5 μL of the suspension on the glassy carbon electrode followed by drying for 10 min at 60°C.

2.3.5 Electrochemical Characterization

Electrochemical characterization was conducted using a glassy carbon rotating ring-disk electrode (RRDE, 5 mm diameter, Pine Research Instrumentation, Raleigh, NC). All experiments

were conducted in O_2-saturated 0.5 M sulfuric acid (pH 1) at 40 °C using a K_2SO_4 saturated $Hg|Hg_2SO_4$ reference electrode (0.65 V/NHE); all potentials were corrected to a reversible hydrogen electrode (RHE) reference based on a measured electrolyte pH of 0.8. A platinum wire coil served as the counter electrode. Linear-sweep polarization curves were recorded in the potential range 1.0–0.4 V/RHE at a scan rate of 0.5 mV s^{-1} and rotation speed of 1200 rpm. In RRDE experiments, the ring was poised at 1.2 V/RHE. Peroxide percentage, $X_{H2O2,}$ was calculated from the collection efficiency ($N = 0.24$), ring current, I_{ring}, and disk current, I_{disk}

$$X_{H_2O_2} = \frac{2I_{ring}/N}{I_{disk} + I_{ring}/N} * 100\%$$

Ring collection efficiency represents the fraction of reaction products produced at the disk that are collected at the ring.[1] This collection efficiency was validated by reduction of ferricyanide at Pt disk and re-oxidation at the ring as explained in detail by Paulus et al.[21] Further experiments confirmed that a MNC catalyst deposition on the Pt disk had no significant impact on collection efficiency.

2.4 Results and Discussion

In this work iron acetate and melamine are used as precursors on various carbon substrates. Pore size distributions obtained by NLDFT of nitrogen adsorption data are shown in Figure 2.1. A wide variety of pore distributions are observed, from Vulcan with little porosity of any size, to Black Pearls with substantial mesoporosity (2-50 nm scale pores) and microporosity (<2 nm pores). The catalyst morphologies are similar to the neat carbon substrates with the main differences in the microporous region. Most of the catalysts lose pore volume during pyrolysis. Norit loses no porosity (Fig 2.1c), while Black Pearls (Fig 2.1b), and Ketjen (Fig 2.1a), lose substantial microporosity. Vulcan has very little porosity to begin with. A potential explanation for decreased catalyst microporosity is deposits from decomposition products, primarily from the

melamine precursor.[1,12] In the case of Norit, the lack of mesoporosity may prevent decomposition products from collecting in the micropores, allowing etching from high temperature nitrogen intermediates such as ammonia. Numerical values for the surface area and pore volume are included in Table 2.1.

Table 2.1: Physical and Electrochemical Characteristics of MNC Catalysts

Carbon Substrate Material	Surface Area (m^2 g^{-1} by BET)		Catalyst Pore Volume (cm^3 g^{-1} by DFT)		N content (wt%)	Activity mA/mg @0.8 V/RHE
	Support	Catalyst	Micropore (<2 nm) ±13%	Mesopore (2-50 nm) ±8%		
Ketjen EC600J	1439	1021	0.39	1.28	4.2±0.4	2.23±0.67
Black Pearls 2000	1426	688	0.35	0.55	3.4±0.4	0.13±0.09
Norit SX Ultra	938	993	0.19	0.23	0.4±0.4	0.06±0.01
Vulcan XC 72R	269	194	0.038	0.19	0.8±0.4	0.02±0.01

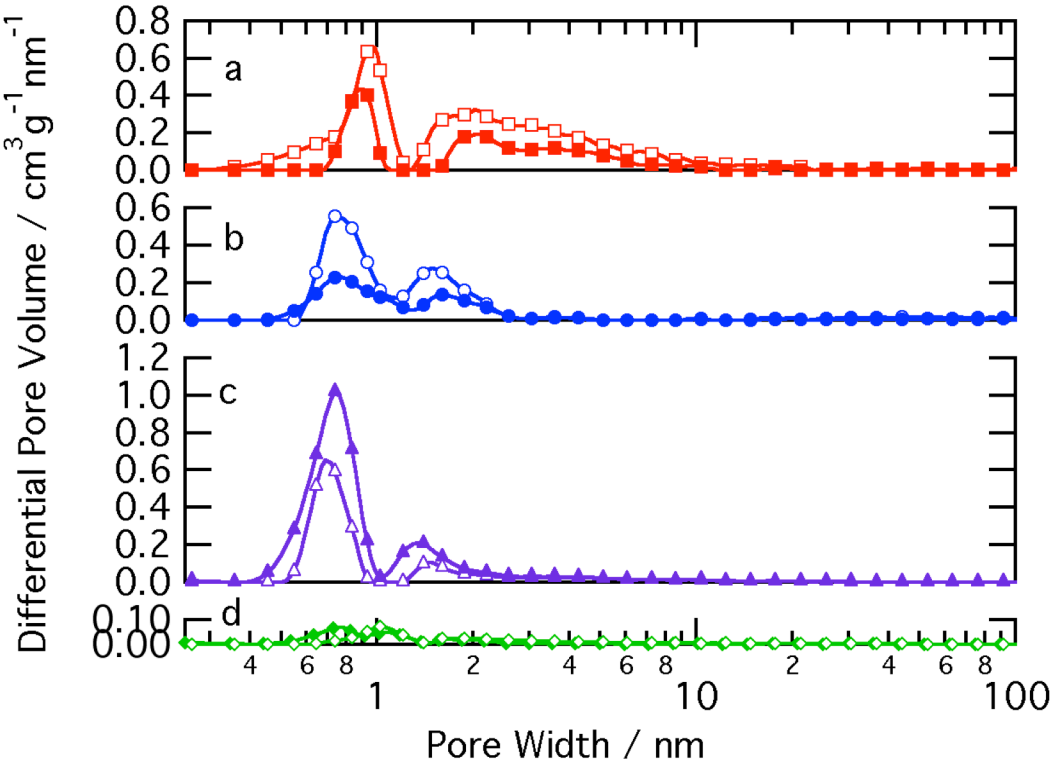

Figure 2.1: Pore Size Distribution of various carbon precursors (open shapes) and the associated catalysts (filled shapes) modeled from DFT calculations based on nitrogen adsorption at 77K. a) Ketjen, b) Black Pearls, c) Norit, d) Vulcan.

Rotating ring-disc electrode (RRDE) studies were performed on the four catalysts. Typical linear sweep polarization curves are shown in Figure 2.2. Catalysts using Ketjen show not only a higher activity than those from other substrates, they also show lower peroxide generation of about 10 percent at 0.8 V vs. RHE decreasing to under 5 percent below 0.5 V vs. RHE. The other catalysts had low activity around 0.8 V vs. RHE preventing an accurate measurement of peroxide generation at that potential. Peroxide generation at 0.5 V vs. RHE for Norit, Black Pearls, and Ketjen were 10, 15, and 20 percent respectively. Except for Norit, the relative peroxide generation correlates with activity. Ketjen-based catalysts generate the least peroxide, followed by Norit, Black Pearls, and Vulcan. Because high peroxide generation implies low current efficiency—*i.e.* not all the oxygen is fully reduced to water—the low peroxide generation of the

relatively inactive Norit catalyst suggest that it may have good catalytic activity for peroxide reduction, which prevents peroxide from escaping the catalyst layer.

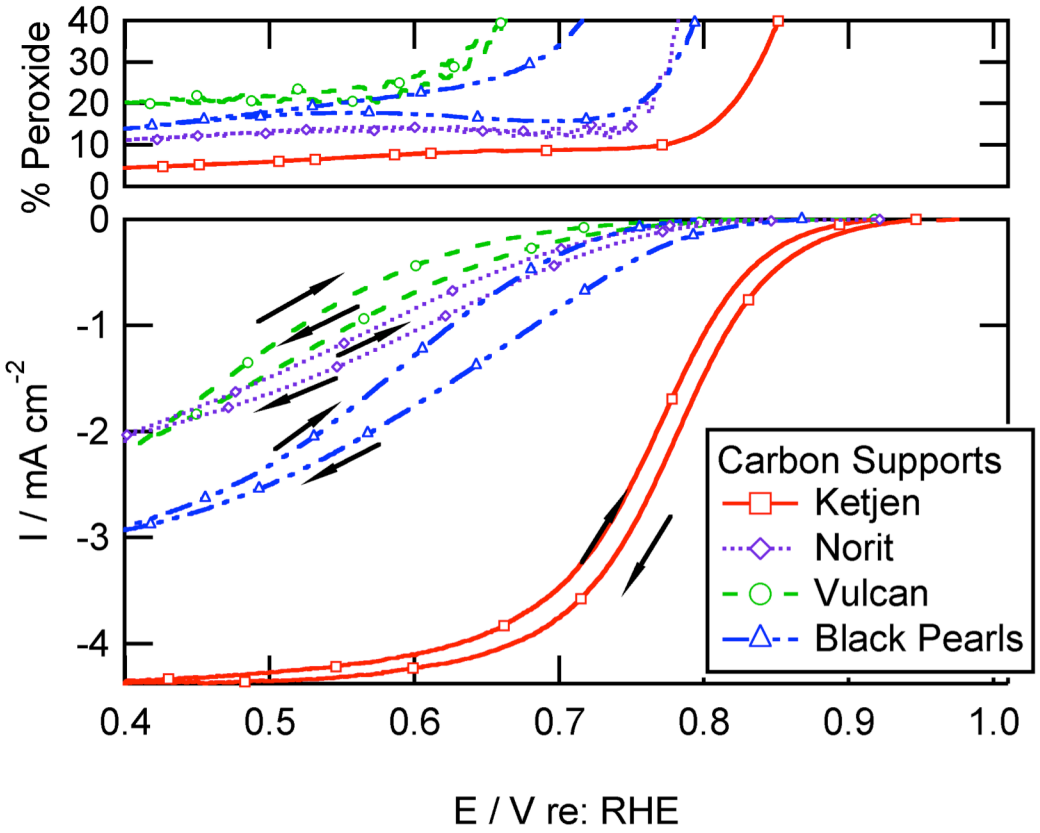

Figure 2.2: Oxygen reduction at rotating ring-disk electrodes (RRDE) with percent peroxide generation. Experimental conditions: O_2-saturated 0.5 M H_2SO_4, 60°C, rotation speed 1200 rpm, catalyst loading of 500 μg/cm^2 on a glassy carbon electrode.

The Tafel plots shown in Figure 2.3 represent mass transfer corrected RDE data, where the key metric is current density at 0.8 V/RHE values of which are listed in Table 3. Mass transfer corrections were accomplished using a Koutecky-Levich relationship:

$$\frac{1}{i} = \frac{1}{i_k} + \frac{1}{i_{pl}}$$

Were the measured current, i, is related to a kinetically limited current i_k and the plateau limiting current, i_{pl}, which was measured from the plateau of the polarization curve. In this way we were able to isolate and report the kinetically limited current for any given potential. As shown in

Figure 2.3, all catalysts exhibit similar Tafel slopes of ~80 mV/decade transitioning to a second larger slope below 0.7 V/RHE. The smaller initial slopes of 80 mV/decade slope are similar to other results for MNC catalysts,[1,22,23] Perry et al. suggest that Tafel slopes in porous electrodes can be controlled by electrochemical kinetics, mass transport, and ohmic resistance.[24] The similarity in Tafel slopes suggests that the ORR mechanism does not vary significantly among these catalysts.

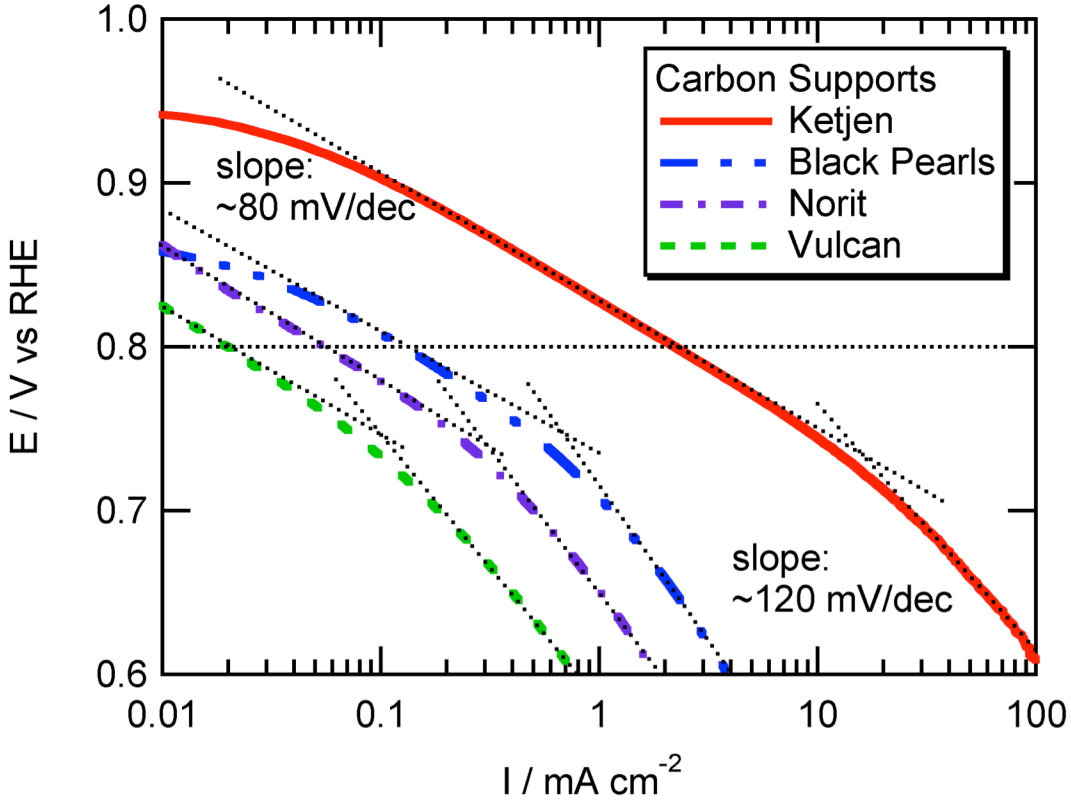

Figure 2.3: Tafel plot of oxygen reduction polarization of four different catalysts. Conditions as in Fig. 2.

A correlation was observed between mesoporous volume and activity as shown in Figure 2.4. Nitrogen content of the catalysts, as determined by CHN analysis, also scales with the mesoporosity and electrochemical activity. Although no correlation was found between virgin microporosity and activity, the correlation indicated by Figure 2.4 suggests that, for fabrication

of catalysts by high-pressure pyrolysis, activity is heavily impacted by a combination of transport effects caused by mesoporosity and the ability of substrates to adsorb nitrogen precursors.

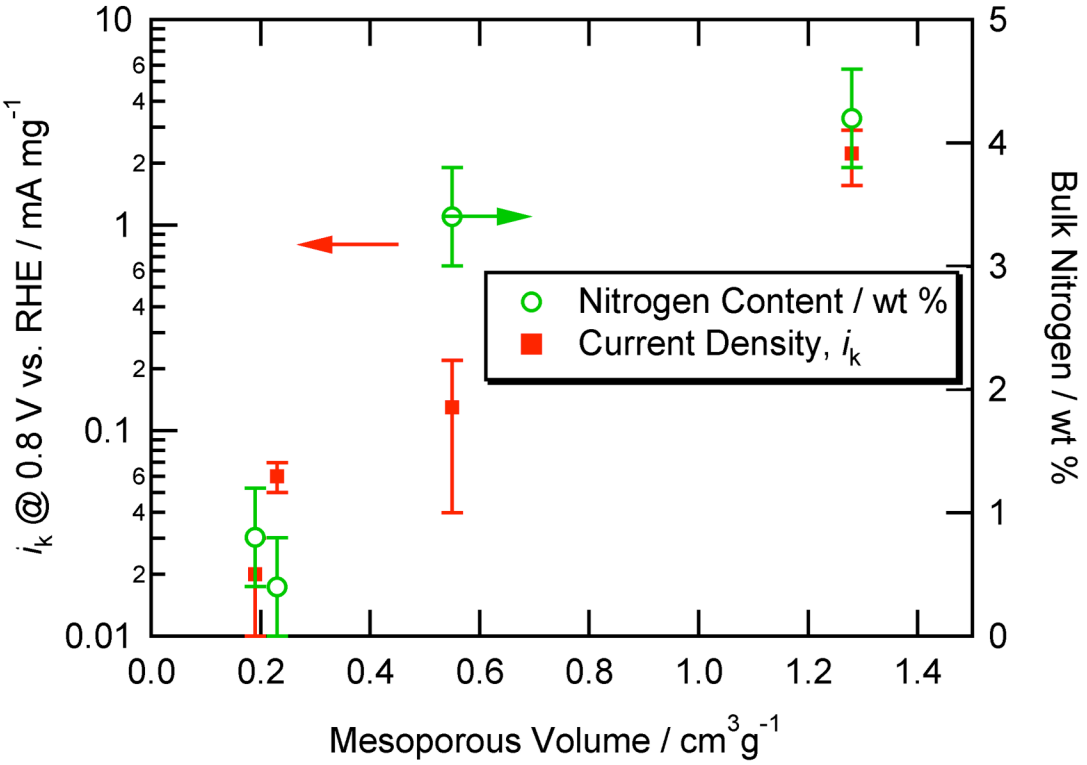

Figure 2.4: Relationship between mesoporous volume of four different catalysts and two different parameters: nitrogen content measured by CHN, and iR-free oxygen reduction current density at 0.8 V vs. RHE.

A second correlation was observed between nitrogen content and iron content as shown in Figure 2.5. These catalysts were analyzed using CHN combustion analysis to measure bulk nitrogen content, and by inductively coupled plasma (ICP) to assess iron content. Carbon materials that retained high iron content after pyrolysis also retained high nitrogen contents. Although nominal iron and nitrogen content were fixed at 4.4 at% and 6.7 at%, respectively, for all catalysts, the final products had varying retention of these initial loadings, and therefore various concentrations of both.

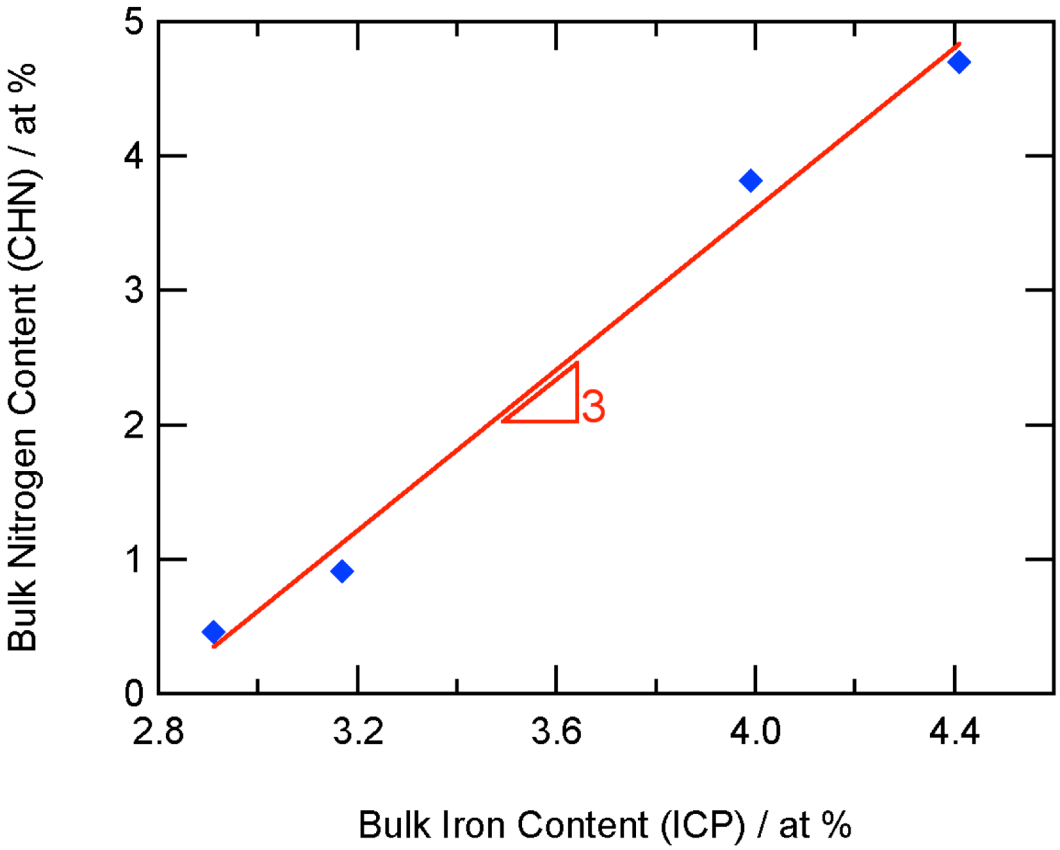

Figure 2.5: Correlation between nitrogen content and iron content in catalysts prepared with various carbon precursors.

Nitrogen is likely lost via ammonia evolution, as evidenced by the strong smell upon opening the pyrolyzed ampule. The mechanism of iron loss is not so obvious. Iron may be lost during the mixing process in ethanol, due to varying levels of iron adsorption on the various carbons. Unadsorbed iron acetate in suspension adheres to the container walls upon drying. Some iron-containing compounds, such as iron pentacarbonyl have high vapor pressures at room temperature.[25] These compounds could evaporate once the pyrolyzed ampule is opened.

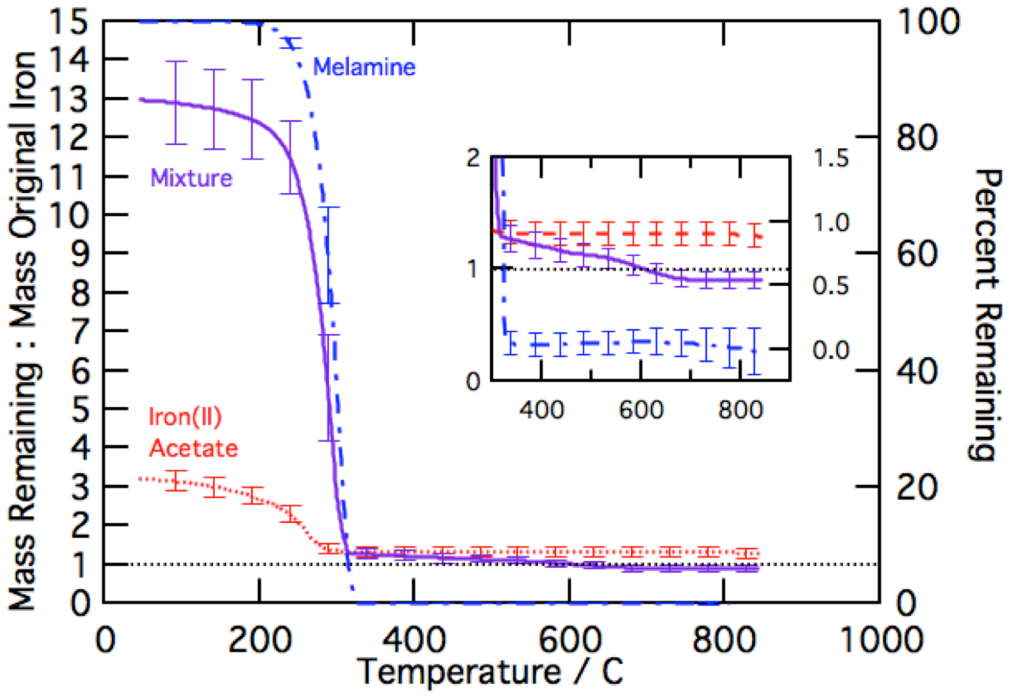

Figure 2.6: TGA of various precursor materials. Mixture represents a 6.3 to 1 nitrogen to iron mixture of melamine and iron (II) acetate.

Table 2.2: Composition of TGA Product by EDS*

Material	Fe (wt%)	C (wt%)	O (wt%)
Melamine, Iron (II) Acetate Mixture (Fe:N::1:6.3)	58±13	26±7	16±7

*No significant nitrogen content

In order to study iron loss via volatile compounds, TGA was performed on iron acetate, melamine, and an iron-melamine mixture in an argon atmosphere. Figure 2.6 shows a plot of sample mass remaining, normalized to original iron content of the precursors (left vertical axis), as a function of temperature. Melamine samples fully volatilize above 300C, resulting in complete mass loss. Iron acetate also loses mass associated with the acetate moieties, and only iron carbide or oxide remains above 300C. One can observe that, for the mixture of iron (II)

acetate and melamine, the relative mass falls well below one above 600 C, suggesting iron loss to the gas phase. EDS of the post-TGA product indicated that the sample contained only about 58 wt% iron (shown in Table 2.2), meaning that only about half of the original iron is retained after TGA. Iron may therefore be lost via a volatile iron compound at high temperatures. The detailed mechanism of this iron loss is a subject of future research.

As evident in Figure 2.5, high iron content correlates to high nitrogen content, which suggests that iron content may encourage nitrogen adsorption, or vice versa. When plotted on a molar basis, as at%, the slope of the trend-line is 3, suggesting a 3:1 atomic ratio of nitrogen to iron in these catalysts. This result is in the right range for most model active sites, which consider either 2:1 or 4:1 ratios.[26,27] The *x*-intercept of the plot is non-zero (2.8 at%), which suggests that a large portion of the iron content is not involved in nitrogen adsorption. Such iron may exist as bulk metal nanoparticles with limited contact with carbon and nitrogen species.

The correlation of nitrogen content with porosity is weak, as shown in Figure 2.4 (right axis), mainly because the activated carbon Norit displayed particularly weak nitrogen absorption. It is likely that chemical or surface properties also contribute to nitrogen adsorption. This would suggest that the various carbon blacks have different optimal nitrogen contents. Various nitrogen contents have been studied on these carbon blacks (data not shown), but the results did not change observed relative activity. For that reason XRD data was collected giving a qualitative assessment of catalyst graphiticity as shown in Figure 2.7. While the majority of the catalysts have the graphitic d-peak around 24 degrees, Norit's peak is shifted about 2 degrees. Although such values of d-peak are too far from graphitic carbon to be quantitatively meaningful, the larger apparent d-spacing (smaller d-peak angle) in Norit signifies a lower degree of graphiticity as compared to the other carbons, which could have a significant impact on iron and/or nitrogen

adsorption.

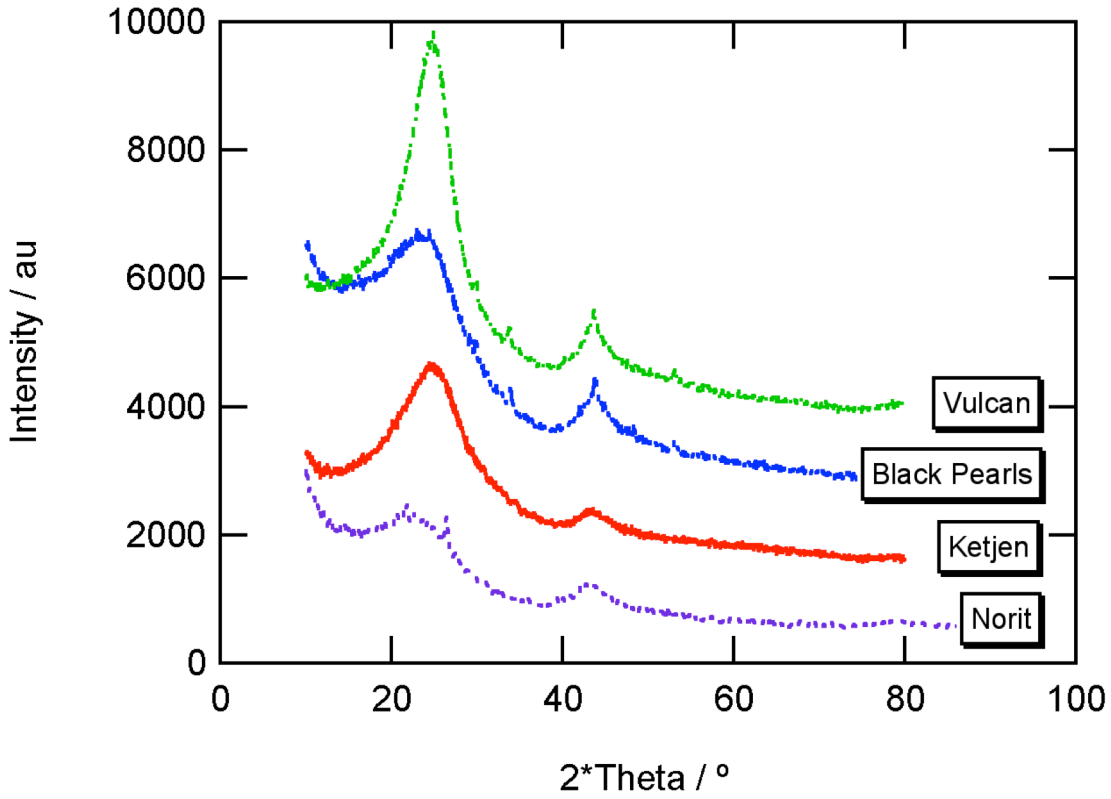

Figure 2.7. X-ray diffraction (XRD) spectra of catalysts prepared with various carbon precursors. Curves offset by 1000 au.

2.5 Conclusions

An electrochemical and morphological study of various carbon supports in MNC electrocatalysts for oxygen reduction indicates that carbon mesoporosity can impact nitrogen adsorption in the catalyst and overall electrochemical activity. The relationship between nitrogen adsorption and activity shows that substrates that adsorb the most nitrogen and iron show the highest activity. Moreover, ICP results show that interactions between the carbon support and iron content also play a role in nitrogen adsorption. The relationship between mesoporosity and nitrogen adsorption may indicate the importance of transport of precursors to potential active sites. As mesoporosity increases, both nitrogen adsorption and activity increase. This relationship

is likely influenced by variations in surface chemistry and microstructure.

2.6 Acknowledgments

The authors gratefully acknowledge support from the United States Dept. of Energy Hydrogen and Fuel Cell Program via Northeastern University. We are also grateful to Dr. Eugene Ustinov for assistance with NLDFT analysis.

*This work is based on results previously published in ECS Transactions **4**:1 pp. 1175 (2011).*

REFERENCES

REFERENCES

1. R. Kothandaraman, V. Nallathambi, K. Artyushkova and S. C. Barton, "Non-precious oxygen reduction catalysts prepared by high-pressure pyrolysis for low-temperature fuel cells," *Applied Catalysis B Environmental,* **92**(1-2), 209-216 (2009). doi:10.1016/J.Apcatb.2009.07.005

2. M. Bron, S. Fiechter, M. Hilgendorff and P. Bogdanoff, "Catalysts for oxygen reduction from heat-treated carbon-supported iron phenantroline complexes," *Journal of Applied Electrochemistry,* **32**(2), 211-216 (2002). doi:10.1023/a:1014753613345

3. H. T. Chung, C. M. Johnston, K. Artyushkova, M. Ferrandon, D. J. Myers and P. Zelenay, "Cyanamide-derived non-precious metal catalyst for oxygen reduction," *Electrochemistry Communications,* **12**(12), 1792-1795 (2010). doi:10.1016/j.elecom.2010.10.027

4. F. Jaouen, S. Marcotte, J. P. Dodelet and G. Lindbergh, "Oxygen reduction catalysts for polymer electrolyte fuel cells from the pyrolysis of iron acetate adsorbed on various carbon supports," *Journal of Physical Chemistry B,* **107**(6), 1376-1386 (2003). doi:10.1021/Jp021634q

5. M. Lefevre, E. Proietti, F. Jaouen and J. P. Dodelet, "Iron-Based Catalysts with Improved Oxygen Reduction Activity in Polymer Electrolyte Fuel Cells," *Science,* **324**(5923), 71-74 (2009). doi:10.1126/science.1170051

6. M. Lefevre and J. P. Dodelet, "Fe-based electrocatalysts made with microporous pristine carbon black supports for the reduction of oxygen in PEM fuel cells," *Electrochimica Acta,* **53**(28), 8269-8276 (2008). doi:10.1016/j.electacta.2008.06.050

7. S. H. Joo, S. J. Choi, I. Oh, J. Kwak, Z. Liu, O. Terasaki and R. Ryoo, "Ordered nanoporous arrays of carbon supporting high dispersions of platinum nanoparticles," *Nature,* **412**(6843), 169-72 (2001). doi:10.1038/35084046

8. S. Pylypenko, T. S. Olson, N. J. Carroll, D. N. Petsev and P. Atanassov, "Templated Platinum/Carbon Oxygen Reduction Fuel Cell Electrocatalysts," *Journal of Physical Chemistry C,* **114**(9), 4200-4207 (2010).

9. E. Proietti, F. Jaouen, M. Lefevre, N. Larouche, J. Tian, J. Herranz and J. P. Dodelet, "Iron-based cathode catalyst with enhanced power density in polymer electrolyte membrane fuel cells," *Nature communications,* **2**, 416 (2011). doi:10.1038/ncomms1427

10. M. Lefevre, J. P. Dodelet and P. Bertrand, "O2 Reduction in PEM Fuel Cells: Activity and Active Site Structural Information for Catalysts Obtained by the Pyrolysis at High Temperature of Fe Precursors," *The Journal of Physical Chemistry B,* **104**(47), 11238-11247 (2000). doi:10.1021/jp002444n

11. R. Yang, A. Bonakdarpour, E. B. Easton, P. Stoffyn-Egli and J. R. Dahn, "Co--C--N Oxygen Reduction Catalysts Prepared by Combinatorial Magnetron Sputter Deposition," *Journal of The Electrochemical Society,* **154**(4), A275-A282 (2007).

12. V. Nallathambi, N. Leonard, R. Kothandaraman and S. Calabrese Barton, "Nitrogen Precursor Effects in Iron-Nitrogen-Carbon Oxygen Reduction Catalysts," *Electrochemical and Solid State Letters,* **14**(6), B55-B58 (2011). doi:10.1149/1.3566065

13. S. Vengatesan, H.-J. Kim, S.-K. Kim, I.-H. Oh, S.-Y. Lee, E. Cho, H. Y. Ha and T.-H. Lim, "High dispersion platinum catalyst using mesoporous carbon support for fuel cells," *Electrochimica Acta,* **54**(2), 856-861 (2008). doi:10.1016/j.electacta.2008.05.072

14. F. Jaouen, M. Lefevre, J. P. Dodelet and M. Cai, "Heat-treated Fe/N/C catalysts for O-2 electroreduction: Are active sites hosted in micropores?," *Journal of Physical Chemistry B,* **110**(11), 5553-5558 (2006).

15. S. Barazzouk, M. Lefevre and J. P. Dodelet, "Oxygen Reduction in PEM Fuel Cells: Fe-Based Electrocatalysts Made with High Surface Area Activated Carbon Supports," *Journal of the Electrochemical Society,* **156**(12), B1466-B1474 (2009). doi:10.1149/1.3242293

16. F. Jaouen, J. Herranz, M. Lefevre, J.-P. Dodelet, U. I. Kramm, I. Herrmann, P. Bogdanoff, J. Maruyama, T. Nagaoka, A. Garsuch, J. R. Dahn, T. Olson, S. Pylypenko, P. Atanassov and E. A. Ustinov, "Cross-Laboratory Experimental Study of Non-Noble-Metal Electrocatalysts for the Oxygen Reduction Reaction," *ACS Applied Materials & Interfaces,* **1**(8), 1623-1639 (2009). doi:10.1021/am900219g

17. S. Brunauer, P. H. Emmett and E. Teller, "Adsorption of gases in multimolecular layers," *Journal of the American Chemical Society,* **60**, 309-319 (1938).

18. E. P. Barrett, L. G. Joyner and P. P. Halenda, "The Determination of Pore Volume and Area Distributions in Porous Substances .1. Computations from Nitrogen Isotherms," *Journal of the American Chemical Society,* **73**(1), 373-380 (1951).

19. E. A. Ustinov, D. D. Do and V. B. Fenelonov, "Pore size distribution analysis of activated carbons: Application of density functional theory using nongraphitized carbon black as a reference system," *Carbon,* **44**(4), 653-663 (2006). doi:10.1016/j.carbon.2005.09.023

20. E. A. Ustinov, "Nitrogen Adsorption on Silica Surfaces of Nonporous and Mesoporous Materials," *Langmuir,* **24**(13), 6668-6675 (2008). doi:10.1021/la704011z

21. U. A. Paulus, T. J. Schmidt, H. A. Gasteiger and R. J. Behm, "Oxygen reduction on a high-surface area Pt/Vulcan carbon catalyst: a thin-film rotating ring-disk electrode study," *Journal of Electroanalytical Chemistry,* **495**(2), 134-145 (2001).

22. T. E. Wood, Z. Tan, A. K. Schmoeckel, D. O'Neill and R. Atanasoski, "Non-precious metal oxygen reduction catalyst for PEM fuel cells based on nitroaniline precursor," in 510-516, (Elsevier Science Bv, 2008). doi:10.1016/j.jpowsour.2007.10.093

23. A. A. Gewirth and M. S. Thorum, "Electroreduction of Dioxygen for Fuel-Cell Applications: Materials and Challenges," *Inorganic Chemistry,* **49**(8), 3557-3566 (2010). doi:10.1021/ic9022486

24. M. L. Perry, J. Newman and E. J. Cairns, "Mass transport in gas-diffusion electrodes: A diagnostic tool for fuel-cell cathodes," *Journal of the Electrochemical Society,* **145**(1), 5-15 (1998).

25. A. G. Gilbert and K. G. P. Sulzmann, "The Vapor Pressure of Iron Pentacarbonyl," *Journal of the Electrochemical Society,* **121**(6), 832-834 (1974). doi:10.1149/1.2401930

26. J. Masa, T. Schilling, M. Bron and W. Schuhmann, "Electrochemical synthesis of metal-polypyrrole composites and their activation for electrocatalytic reduction of oxygen by thermal treatment," *Electrochimica Acta,* **60**(0), 410-418 (2012). doi:10.1016/j.electacta.2011.11.076

27. M. Ferrandon, A. J. Kropf, D. J. Myers, K. Artyushkova, U. Kramm, P. Bogdanoff, G. Wu, C. M. Johnston and P. Zelenay, "Multitechnique Characterization of a Polyaniline--Iron--Carbon Oxygen Reduction Catalyst," *The Journal of Physical Chemistry C,* **116**(30), 16001-16013 (2012).

Chapter 3. Solid Alkalinity of MNC Catalyst for Oxygen Reduction Reaction

3.1 Abstract

Low-cost oxygen reduction catalysts composed of pyrolyzed metal/nitrogen/carbon (MNC) compounds involve the association of metal atoms with nitrogen species integrated into a conductive carbon support. Currently, the nature of the active site is not completely understood due to complexities introduced by pyrolysis on high surface-area supports. The present work considers the impact of surface alkalinity on the activity of MNC catalysts prepared using a high-pressure pyrolysis method. The basic site strength and quantity are calculated by two different methods, and it is shown that increased Brønsted-Lowry basicity correlates to more active catalysts.

3.2 Introduction

The cost of precious metal oxygen reduction catalysts represents a major barrier to commercialization of low temperature fuel cells. Low-cost oxygen reduction catalysts composed of pyrolyzed metal/nitrogen/carbon (MNC) compounds[1,2] have been studied for over 40 years but have recently been demonstrated to possess oxygen reduction activity nearly high enough to replace platinum-based catalysts. In the literature the impact of porosity, nitrogen content, and many other parameters on catalyst activity have been explored, but the nature of the active site is not completely understood due to complexities introduced by pyrolysis on high surface-area supports. Further understanding of the active site will allow better optimization of the catalysts, and lead to increased understanding of oxygen reduction.

The present work considers the impact of surface basicity on the activity of MNC catalysts. Pyrolysis is conducted in a closed vessel containing metal, nitrogen, and carbon precursors,

thereby controlling mass losses due to convection of high temperature byproducts. The carbons used are Ketjen EC 600J, Black Pearls 2000, and Vulcan XC 72R.

Previous reports have considered many important elements of NPM catalysts such as nitrogen content,[1,3] nitrogen precursors,[2-4] iron precursors,[5] carbon precursors,[3,6,7] and heat treatment [1]. Previous work has highlighted the importance of surface chemistry to identification and understanding of the active site(s).[6] The present work elucidates one aspect of surface chemistry for MNC catalysts, Brønsted basicity, and how that aspect could impact catalyst function.

Studies by Herranz et al. have highlighted the importance of surface chemistry to identification and understanding of the active site(s),[6] and they have concluded that the turnover frequency of MNC catalysts is dependent on basic nitrogen groups.[8] Kramm et al. have suggested that the principal active site is an iron-nitrogen complex with a basic neighbor nitrogen functionality that changes the energy scheme of the central iron atom.[8] Both researchers suggest that alkalinity would have a significant impact on catalyst activity based on correlations between surface chemistry and activity, but the causality is not clear. For this reason the proposed work attempts to increase the understanding of alkalinity in APMNC catalysts.

3.3 Experimental Methods

3.3.1 Materials

Iron(II)-acetate, melamine, Nafion® solution (5 wt%) and sulfuric acid (ACS grade) were obtained from Alfa Aesar (Ward Hill, MA). Ketjenblack® 600JD carbon black was obtained from Akzo Nobel (Chicago, IL). Black Pearls 2000 and Vulcan XC72R carbon blacks were obtained from Cabot Corporation (Boston, MA). Pressurized oxygen cylinders were obtained from Airgas (Lansing, MI). All materials were used as received.

3.3.2 Catalyst Synthesis

All catalysts were prepared as described previously.[6] Briefly, melamine, iron acetate, and carbon materials were dispersed in 190 proof ethanol, which was then evaporated to yield a dry powder. After addition melamine at 50 wt% of the dry powder, the sample was flame-sealed in a quartz ampule under vacuum, and subjected to heat treatment at 800°C for three hours. The enclosed ampule provides retention of volatile precursors as well as increased activity due to elevated pressure.

3.3.3 Alkalinity Characterization

The surface pH of the neat carbon supports and the as-prepared catalysts was determined by sonicating suspensions of 0.5-8 g/L solids in a 10 mL, 0.1 M aqueous KCl solution. After a five minute resting period, The pH was of this suspension was measured (Fischer Scientific Accumet AB15) relative to the pure KCl solution (pH 6.5±0.5), representing the impact of the solid on the electrolyte.[9]

3.3.4 Electrode Preparation

The catalyst ink was prepared as previously described,[6] Briefly, 4 mg of catalyst was ultrasonically dispersed in a mixture of 150 μL of ethanol and 50 μL of 5 wt% Nafion® solution. Rotating disk electrodes were prepared at a catalyst loading of 0.5 mg cm^{-2} by depositing an appropriate amount of the suspension on a glassy carbon rotating disk electrode (RDE, 5 mm diameter, Pine Research Instrumentation, Raleigh, NC) and drying for 10 min in air.

3.3.5 Electrochemical Characterization

All experiments were conducted in O_2-saturated 0.5 M sulfuric acid at room temperature using a K_2SO_4 saturated $Hg|Hg_2SO_4$ reference electrode (0.65 V/NHE); all potentials were corrected to the RHE scale. A platinum wire served as the counter electrode. Linear-sweep

polarization curves were recorded in the potential range 1.0-0.4 V/RHE at a scan rate of 0.5 mV s^{-2} and rotation speed of 1200 rpm.

3.4 Results and Discussion

Increased pH of the catalyst slurries represent a decrease in protons in the aqueous KCl caused by retention of basic surface groups on the catalyst surface (schematic in Figure 3.1). In this way, high pH indicates solid basicity. Considering that the catalyst is known to have a wide variety of nitrogen groups,[1] one would expect pH to vary with nominal nitrogen content due to the known proton affinity of nitrogen based compounds. Schoone et al use molecular dynamics to calculate proton affinities for eight different pyridine and imidazole based derivatives, confirming that these nitrogen containing molecules are basic[10] In fact, pH closely followed catalyst activity and not nominal nitrogen content indicating that solid basicity and catalytic activity are closely related. This relationship could take a number of different forms. For example, the increased basicity could be a result of optimized chemisorption of nitrogen onto the catalyst surface during pyrolysis. Although a complete understanding of this process would require further testing.

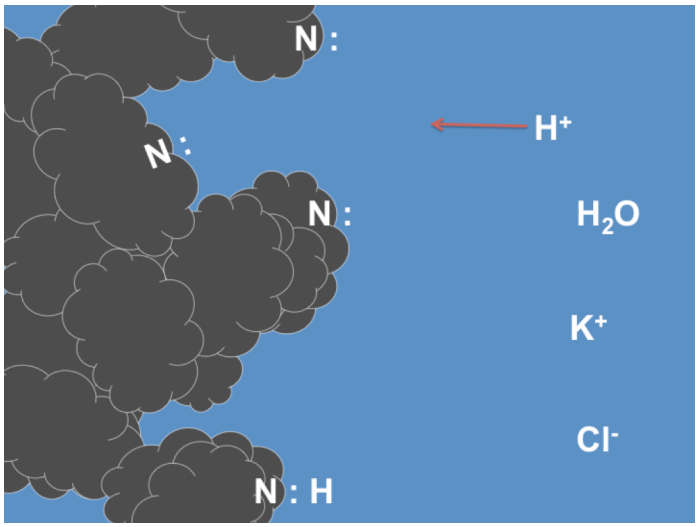

Figure 3.1: Schematic of catalyst interaction with an aqueous KCl solution where basic surface groups retain protons from the electrolyte reducing the pH of the slurry.

A second consideration is the relationship between specific surface area and pH. If solid basicity were tied solely to specific surface area and not to quantity of active sites, one would expect an increase in pH with an increase in specific surface area. Previous studies have shown a decrease in surface area with increasing nitrogen content for catalysts prepared by high-pressure pyrolysis.[1] Nallathambi et al use nitrogen precursors of various nitrogen to carbon ratios to show that increased carbon in precursors leads to decreased surface area.[11] The observed maximum in catalyst basicity for varying nitrogen content suggests that surface area does not significantly control surface basicity.

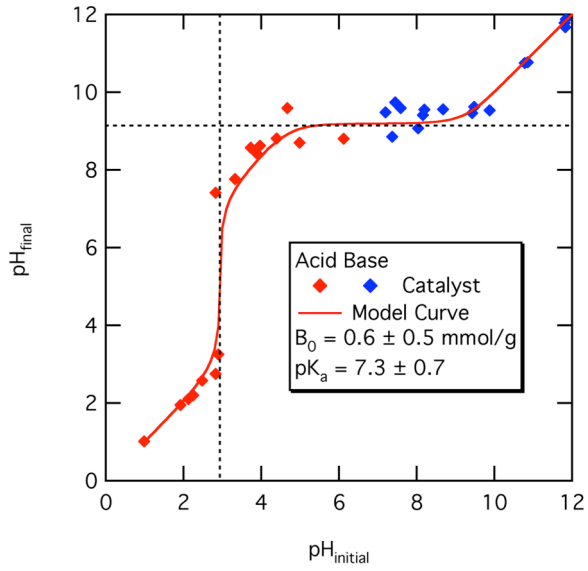

Figure 3.2: Boehm Titration: suspension pH as a function of initial solution pH. Experimental conditions: sonicated 2 gL-1 catalyst slurries; acid solutions obtained by dilution of sulfuric acid, base solutions by solutions of sodium hydroxide.

In to order to calculate average pKa and quantity of basic sites on the catalyst, a Boehm titration was performed as explained by Herranz et al.[12] In short, aqueous solutions of varying concentrations of H_2SO_4 and NaOH are sonicated to provide a spectrum of pH values. Catalyst is added to the solutions, and the slurries are sonicated. After sonication the pH is measured again. Figure 3.2 represents a plot of catalyst slurry pH as a function of initial solution pH prior to catalyst insertion. The data can be modeled with the following equations:

$$pH_i = \log[B_0] \tag{1}$$

$$pH_f = 7 + \tfrac{1}{2}(pK_a + \log[B_0]) \tag{2}$$

where pH_i is the initial pH prior to addition of solid, B_0 is the concentration of protonated surface sites, pH_f is the pH after addiction of solid, and pK_a is the acid dissociation constant. The first equation represents the first inflection (around $pH_i = 3$) caused by the basic material in the

presence of a concentration of a strong acid (H_2SO_4) at which all the basics sites become protonated and there are essentially no remaining excess protons in the solution. The second equation represents the plateau caused by the basic material in the presence of an essentially neutral solution at which the material is modeled as a weak base. The resulting curve was used to calculate an average pK_a (7.3 ± 0.7) and quantity of basic sites (0.6 ± 0.5 mmol g^{-1}). These values agree well with what Herranz et al. calculated for their ammonia based catalyst,[12] and these results also suggest that the vast majority of basic sites are weak bases because the average acid dissociation constant is on the same order of magnitude as that of water.

The correlation between activity and basicity was confirmed in an optimization study of nominal nitrogen content shown in Figure 3.3. Varying amounts of nitrogen precursor were added to the precursor mixture before pyrolysis. An optimal nitrogen proportion was found at

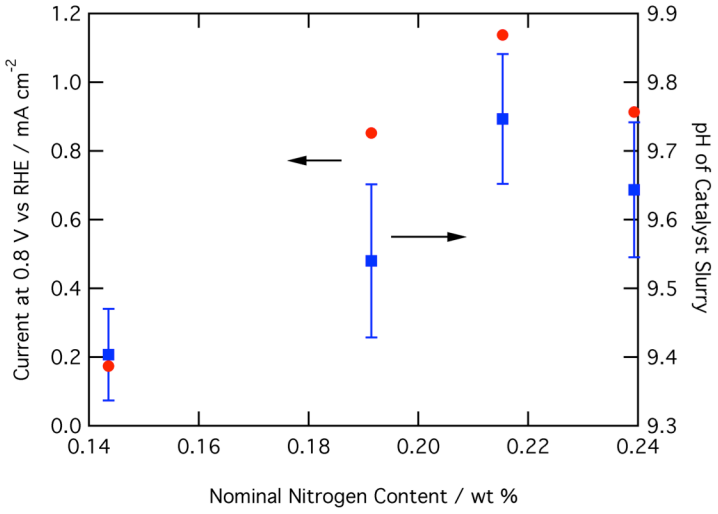

Figure 3.3: Comparison of nominal nitrogen content to current and basicity of the catalyst. Experimental conditions: RDE: 0.8 V vs. RHE, 0.5M H_2SO_4, 1200 rpm, catalyst loading 0.5 mg/cm^2 on glass carbon electrode, pH: 1 g/L catalyst suspension, 0.1 M KCl.

around 22 wt.% N. Catalyst basicity did not vary directly with nitrogen content, as would be expected if basicity were only caused by nitrogen content in the catalyst. Instead pH closely followed catalyst activity confirming that the active site is associated with basic sites.

A second consideration should be the relationship between specific surface area and pH. If catalyst proton adsorption were tied solely to specific surface area and not to quantity of active sites, one would expect an increase in pH with an increase in specific surface area. Previous studies have shown an general decrease in surface area with increasing nitrogen content for catalysts prepared by high-pressure pyrolysis.[1] Nallathambi et al use nitrogen precursors of various nitrogen to carbon ratios to show that increased carbon in precursors leads to decreased surface area.[2] The observed maximum in catalyst basicity for varying nitrogen content suggests that surface area does not significantly control surface basicity.

3.5 Conclusions

An electrochemical and surface basicity study of various MNC electrocatalysts for oxygen reduction indicates that catalyst basicity is connected to overall electrochemical activity. A trend was found between catalyst activity and a pH shift in suspension of the catalyst. Higher pH values represent an increase in basic proton adsorption sites. The trend between catalyst activity and a pH suggests that basicity is an important parameter in catalyst site activity and identification.

REFERENCES

REFERENCES

1. R. Kothandaraman, V. Nallathambi, K. Artyushkova and S. C. Barton, "Non-precious oxygen reduction catalysts prepared by high-pressure pyrolysis for low-temperature fuel cells," *Applied Catalysis B Environmental,* **92**(1-2), 209-216 (2009). doi:10.1016/J.Apcatb.2009.07.005

2. V. Nallathambi, N. Leonard, R. Kothandaraman and S. C. Barton, "Nitrogen Precursor Effects in Iron-Nitrogen-Carbon Oxygen Reduction Catalysts," *Electrochemical and Solid State Letters,* **14**(6), B55-B58 (2011). doi:10.1149/1.3566065

3. F. Jaouen, J. Herranz, M. Lefevre, J.-P. Dodelet, U. I. Kramm, I. Herrmann, P. Bogdanoff, J. Maruyama, T. Nagaoka, A. Garsuch, J. R. Dahn, T. Olson, S. Pylypenko, P. Atanassov and E. A. Ustinov, "Cross-Laboratory Experimental Study of Non-Noble-Metal Electrocatalysts for the Oxygen Reduction Reaction," *ACS Applied Materials & Interfaces,* **1**(8), 1623-1639 (2009). doi:10.1021/am900219g

4. J. Tian, L. Birry, F. Jaouen and J. P. Dodelet, "Fe-based catalysts for oxygen reduction in proton exchange membrane fuel cells with cyanamide as nitrogen precursor and/or pore-filler," *Electrochimica Acta,* **56**(9), 3276-3285 (2011). doi:10.1016/j.electacta.2011.01.029

5. G. Faubert, G. Lalande, R. Cote, D. Guay, J. P. Dodelet, L. T. Weng, P. Bertrand and G. Denes, "Heat-treated iron and cobalt tetraphenylporphyrins adsorbed on carbon black: Physical characterization and catalytic properties of these materials for the reduction of oxygen in polymer electrolyte fuel cells," *Electrochimica Acta,* **41**(10), 1689-1701 (1996). doi:10.1016/0013-4686(95)00423-8

6. N. D. Leonard, V. Nallathambi and S. Calabrese Barton, "Carbon Supports for Non-Precious Metal Proton Exchange Membrane Fuel Cells," *ECS Transactions,* **41**(1), 1175-1181 (2011). doi:10.1149/1.3635650

7. M. Lefevre and J. P. Dodelet, "Fe-based electrocatalysts made with microporous pristine carbon black supports for the reduction of oxygen in PEM fuel cells," *Electrochimica Acta,* **53**(28), 8269-8276 (2008). doi:10.1016/j.electacta.2008.06.050

8. U. I. Kramm, J. Herranz, N. Larouche, T. M. Arruda, M. Lefevre, F. Jaouen, P. Bogdanoff, S. Fiechter, I. Abs-Wurmbach, S. Mukerjee and J.-P. Dodelet, "Structure of the catalytic sites in Fe/N/C-catalysts for O2-reduction in PEM fuel cells," *Physical Chemistry Chemical Physics,* **14**(33), 11673-11688 (2012). doi:10.1039/c2cp41957b

9. A. Mukherjee, A. R. Zimmerman and W. Harris, "Surface chemistry variations among a series of laboratory-produced biochars," *Geoderma,* **163**(3-4), 247-255 (2011). doi:10.1016/j.geoderma.2011.04.021

10. K. Schoone, J. Smets, R. Ramaekers, L. Houben, L. Adamowicz and G. Maes, "Correlations between experimental matrix-isolation FT-IR and DFT (B3LYP) calculated data for isolated 1: 1 H-bonded complexes of water and pyridine or imidazole derivatives," *Journal of molecular structure,* **649**(1), 61-68 (2003).

11. V. Nallathambi, N. Leonard, R. Kothandaraman and S. Calabrese Barton, "Nitrogen Precursor Effects in Iron-Nitrogen-Carbon Oxygen Reduction Catalysts," *Electrochemical and Solid State Letters,* **14**(6), B55-B58 (2011). doi:10.1149/1.3566065

12. J. Herranz, F. Jaouen, M. Lefevre, U. I. Kramm, E. Proietti, J.-P. Dodelet, P. Bogdanoff, S. Fiechter, I. Abs-Wurmbach, P. Bertrand, T. M. Arruda and S. Mukerjee, "Unveiling N-Protonation and Anion-Binding Effects on Fe/N/C Catalysts for O2 Reduction in Proton-Exchange-Membrane Fuel Cells," *The Journal of Physical Chemistry C,* **115**(32), 16087-16097 (2011). doi:10.1021/jp2042526

Chapter 4. Analysis of Adsorption Effects on a Metal-Nitrogen-Carbon Catalyst using a Rotating Ring-Disk Study

4.1 Abstract

A steady-state, rotating ring disk study of the oxygen reduction reaction (ORR) was conducted in acid environment using a pyrolyzed metal/nitrogen/carbon (MNC) electrocatalyst. Analysis of peroxide generation indicates that ORR proceeds both via a direct four-electron pathway to water at high potentials and an indirect peroxide pathway at low potentials. Above 0.6 V vs RHE, the direct four-electron pathway to water without a desorbing intermediate dominates oxygen reduction because peroxide generation is inhibited due to site availability. In contrast, at potentials below 0.6 V, oxygen reduction begins to shift to the indirect peroxide pathway due to fast kinetics and higher site availability. The net peroxide generation remains relatively low over the entire range due to reduction of peroxide to water.

4.2 Introduction

The need for less expensive electrocatalysts for the oxygen reduction reaction (ORR) in low temperature fuel cells has impeded commercialization of these devices for transportation applications. Metal/nitrogen/carbon (MNC) compounds represent a major focus in the search for platinum alternatives.[1-3] These compounds involve the combination of metal and nitrogen components immobilized in a conductive carbon matrix, and are typically pyrolyzed to enhance activity and stability.[4] Although the structure of the MNC active site is poorly understood due to complexities introduced by pyrolysis on high surface-area supports, an increased understanding of mechanism provides evidence for possible structures, as well as direction for further engineering optimization of these catalysts for fuel cell applications. In the present work, a

rotating ring-disk electrode analysis is conducted to increase understanding of oxygen and peroxide reactions occurring on a pyrolyzed MNC catalyst.

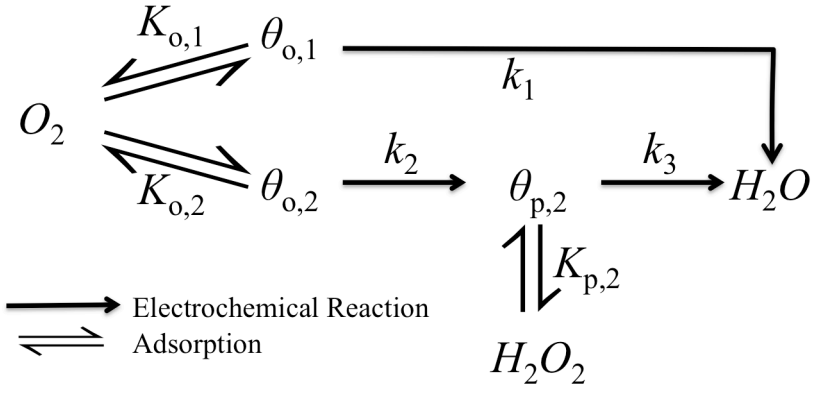

Figure 4.1: Reaction schematic showing two pathways: pathway one (Ko,1 and k1) is the complete reduction of oxygen to water with no desorbing intermediate and pathway two (Ko,2 and k2) is the two-electron reduction to a desorbing peroxide intermediate that disperses into the catalyst layer (Kp,2), but also has the potential to be further reduced to water (k3).

The oxygen reduction reaction is considered here to be composed of two pathways (Fig. 4.1).[5-10] The first pathway represents direct four-electron reduction to water without a desorbing intermediate (k_1 in Fig. 4.1). The second pathway represents incomplete reduction of oxygen to hydrogen peroxide (k_2), which can desorb from the surface ($K_{P,2}$),[5] disproportionate to water and oxygen,[7] or reduce to water (k_3).[7] Jaouen found that disproportionation was insignificant for his Fe-N-C catalyst and that disproportionation reaction rates would have to be orders of magnitude higher that experimental values to account for the low peroxide yield found in these catalyst.[7] We therefore neglect disproportionation in the present work.

Rotating ring-disk electrode (RRDE) experiments are used to distinguish between the above two pathways. The RRDE allows for controlled, well-characterized transport to and from the catalyst layer at steady state.[11] An analysis can be performed considering the figure of merit,

$I_D N/I_R$, vs. $\omega^{-1/2}$ where I_D is disk current, N is ring electrode collection efficiency, I_R is ring current, and ω is rotation speed.[6,8-10] The figure of merit, $I_D N/I_R$, represents a ratio of disk current to flux of intermediates from the disk, and indicates the electronic efficiency of the catalyzed reaction. This parameter can easily be connected to Koutecky-Levich relationships that are mathematically developed from kinetic models, from which rate constants may be determined by comparison to experimental results. Hsueh et al. present five such models for RRDE results,[9] and Anastasijevic et al. present another, more sophisticated, model.[6] The Anastasijevic model makes the distinction of representing the 4-electron pathway not as an ideal direct reduction pathway, but as a strongly adsorbed pathway.

The difficulty in applying these models to the present system is that they assume a planar electrode. The present MNC catalysts are porous electrodes with nonzero thickness, adding transport effects that are not considered in the above models.

Previous RRDE studies of non-precious metal catalysts for oxygen reduction[1,12-17] generally show an increase in peroxide generation by one to two percent per 0.1 mg/cm^2 decrease in loading.[1,13,17,18] This suggests that peroxide detection at the ring could be artificially low because inner layers may further reduce peroxide to water, decreasing peroxide at the ring and increasing total disk current. Additionally, more active catalysts have been found to produce less peroxide; this is found both by varying metal content[14] and morphology of the carbon support. Such considerations motivate the need for increased understanding of the ORR mechanism using MNC catalysts. For the present work we take steady-state measurements in order to insure uniform transport characteristics as well as minimizing unstable intermediates. This has significant implications especially due to the impact of transport phenomena on peroxide and oxygen availability at the electrode surface.

In the present work, an analysis of the MNC catalyst is attempted via the figure of merit, $I_D N/I_R$. This method is revised to isolate the indirect ORR pathway and establish a new figure of merit, $C_o N/I_R$. Finally, this new figure of merit is utilized to understand the kinetic and adsorption limitations of the MNC catalyst in the context of Langmuir Hinshelwood kinetics.

4.3 Experimental Methods

4.3.1 Materials

Carbon, nitrogen, and iron materials used in catalyst synthesis were Ketjen 600JD carbon black (Akzo Nobel, Chicago, IL), melamine (Alfa Aesar, Ward Hill, MA), and iron (II) acetate (Alfa Aesar, Ward Hill, MA) respectively. Materials used in characterization were perfluorosulfonic acid-PTFE copolymer (5 wt%), reagent grade sulfuric acid (Alfa Aesar, Ward Hill, MA), and oxygen (Airgas, Lansing, MI).

4.3.2 Catalyst Synthesis

Catalysts were synthesized as described previously.[1,16,18] Briefly, Ketjen (95.7 wt.%), melamine (0.8 wt.%), and iron (II) acetate (3.5 wt.%) were dispersed in ethanol and dried overnight to produce a dry powder. Further melamine was added to the powder in a ratio of 5:9 to increase the nitrogen content to 24 wt.% (resulting iron content was 0.7 wt.%), and 105 mg were inserted in a quartz ampule. The quartz ampule was pulled under vacuum to a volume of 2.4 cc, and pyrolyzed at 800° C for 3 hours. The quartz ampule was opened and the catalyst consisted of the contained powder.

4.3.3 Electrode Preparation

The catalyst ink was prepared by ultrasonically mixing 4 mg catalyst in 50 µL of 5 wt.% ionomer and 150 µL 190 proof ethanol as described previously[16], catalyst layers were prepared at

loadings of 0.5 to 0.1 mg cm^{-2} by depositing 5 μL of the ink on the 5 mm diameter, glassy-carbon disk of a rotating ring-disk electrode (Pine Research Instrumentation, Raleigh, NC) and drying for 10 min in air. The ink was diluted with ethanol to achieve lower loadings; in this way the drop volume and ionomer to catalyst ratio were held constant for all loadings.

4.3.4 Electrochemical Characterization

Experiments were conducted in oxygen saturated 0.5 M sulfuric acid at room temperature. Potentials were measured relative to a Hg/Hg_2SO_4 reference electrode that was calibrated with respect to a reversible hydrogen electrode. All potentials were corrected to RHE scale (0.7 V vs. RHE). A platinum wire served as the counter electrode. Potentiostatic measurements were made at 400, 900, 1200, and 1600 rpm in 50 mV increments between 0.2 and 0.9 V vs. RHE.

Fractional peroxide yield, χ_p, was calculated based on the following equation:[19]

$$\chi_{\mathrm{P}} = \frac{2I_{\mathrm{R}}/N}{I_{\mathrm{D}} + I_{\mathrm{R}}/N} \qquad [1]$$

Where I_R is the ring current, N the collection efficiency, and I_D the disk current. Collection efficiency, N, was calculated from similar potentiostatic measurements in 0.1 M NaOH, 0.01 M $K_3Fe(CN)_6$. The collection efficiency was not found to vary significantly with loading, although it did decrease slightly with rotation speed consistent with Claude et al.[20] Collection efficiencies were 0.24 ± 0.01, 0.23 ± 0.01, 0.23 ± 0.01, and 0.22 ± 0.01 for 400, 900, 1200, and 1600 rpm respectively.

4.4 Results and Discussion

Potentiostatic, steady-state RRDE experiments were conducted at fixed catalyst loading for four different disk rotation speeds, and at fixed rotation speed for five different loadings. Fig. 4.2a shows polarization disk current and ring current with respect to disk potential at various rotation speeds. Above 0.7 V, both the disk current, I_D, and ring current, I_R, exhibit exponential (Tafel) dependence on potential. The disk limiting current (I_{lim}, the current plateau below 0.6 V) increases with increasing rotation speed, indicating mass transfer limitation. The ring current also increases with rotation speed, but is more weakly correlated than the disk current. This implies that $I_D N/I_R$ increases with rotation speed.

Fig. 4.2b shows steady state polarization curves at various catalyst loadings. Loading impacts disk current at high potentials, where the current falls below I_{lim}, but impacts ring current much more significantly, even at low potentials.

Comparisons can be made between the peroxide generation rate and the overall rate of water production. Fig. 4.2b shows that above 0.7 V vs. RHE, disk current increases significantly with loading, whereas ring current is relatively constant. The disk current at such high potentials can therefore be primarily attributed to four-electron reduction because the ring current is 500-fold smaller and constant over the same loading range. Hence, the peroxide generating ORR pathway appears to be insignificant at high potentials.

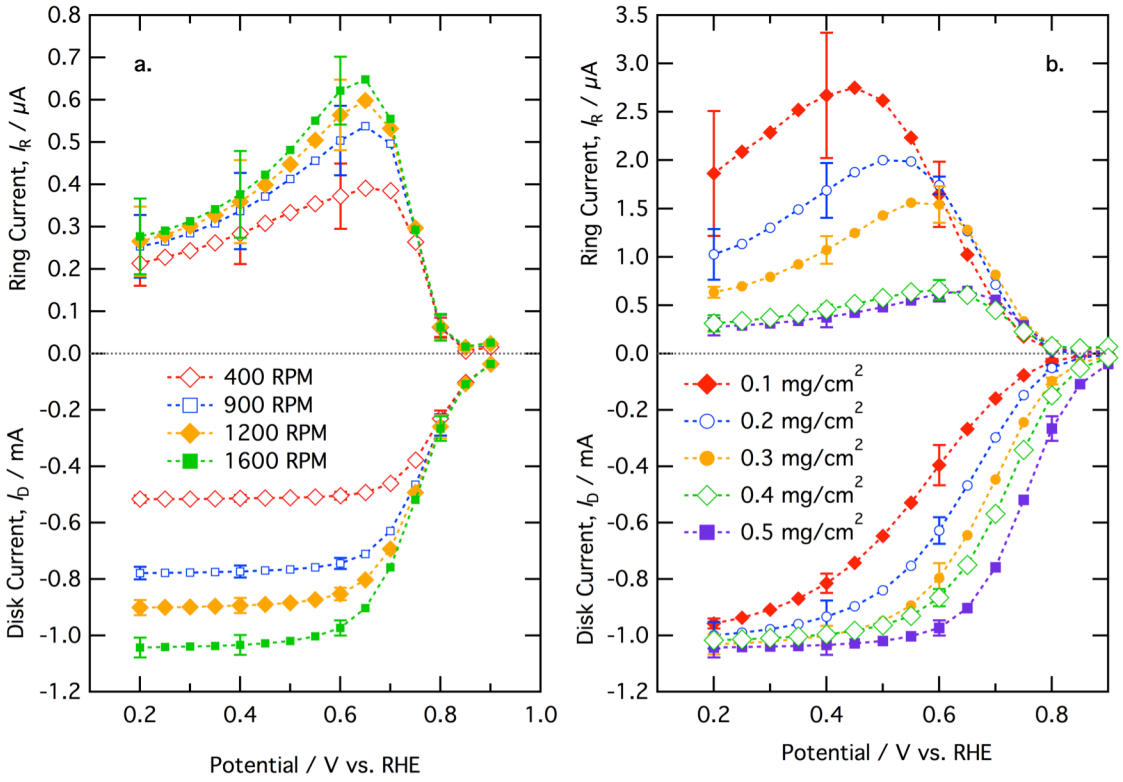

Figure 4.2: Steady-state polarization curve showing disk current and ring current: 0.5 M H_2SO_4, room temperature, oxygen saturated, ring poised at 1.2 V vs. RHE at (a) 0.5 mg cm^{-2}, various rotation speeds (b) 1600 rpm, various loadings.

The ring current, I_R, can be thought of in two ways: as a measure of peroxide flux from the disk and as a measure of peroxide concentration at the disk. In the following results and discussion both perspectives will be considered.

The exponential increase of ring current with decreasing potential near 0.7 V vs RHE (Fig. 4.2) suggests that peroxide generation is limited by the kinetics of the first $2e^-$ reduction step, because the reduction of oxygen to hydrogen peroxide coincides with that potential. Decreasing ring current below the maximum at 0.5-0.6 V suggests either the onset of step 3 (further reduction of peroxide to water) or competition between the two different oxygen reduction reactions (steps 1 and 2). A detailed analysis of the $2e^- + 2e^-$ reaction pathway (I_2 and I_3) is necessary to compare these two phenomena, via the figure of merit, $I_D N/I_R$.[6,8-10]

By assuming a reaction mechanism, an expression for $I_D N/I_R$ can be obtained in terms of fundamental rate constants plus the rotation rate.[5,8-10] Without considering adsorption (Ignoring $K_{o,1}$ and $K_{o,2}$), the expression for the mechanism displayed in Fig. 4.1 is:[9]

$$\frac{I_D N}{I_R} = 1 + 2\frac{k_1}{k_2} + \frac{2 + 2k_1/k_2}{z_P} k_3 \omega^{-1/2} \quad [2]$$

Where k_1, k_2, and k_3 are the rate constants for reduction of oxygen to water, reduction of water to hydrogen peroxide, and reduction of hydrogen peroxide to water, respectively. The parameter $z_p = 0.62 D_p^{2/3} \nu^{-1/6}$ is an abbreviation for the group of constants in the Levich equation:[5,6,8,9]

$$i_{mt} = 0.62 n F C_b D^{2/3} \nu^{-1/6} \omega^{1/2} \quad [3]$$

Where the mass transport limited current at a rotating disk, i_{mt}, is a function of n is the number of electrons per mole oxygen, F is Faraday's constant, C_b is a bulk concentration, D is diffusivity, v is viscosity, and ω is the rotation speed. The parameter z is calculated from a correlation of the mass transfer limiting current and $\omega^{1/2}$. Based on a bulk oxygen concentration of 1 mM[21] and a viscosity of 0.01 cm^2/s,[22] the resulting z values indicate diffusivities of $(2.17 \pm 0.07) \times 10^{-5}$ cm^2/s for oxygen (which is in the range of reported values: 1.87×10^{-5} to 2.12×10^{-5} cm^2/s)[21] and $(1.28 \pm 0.25) \times 10^{-5}$ cm^2/s for hydrogen peroxide (reported value: 1.71×10^{-5} cm^2/s).[23]

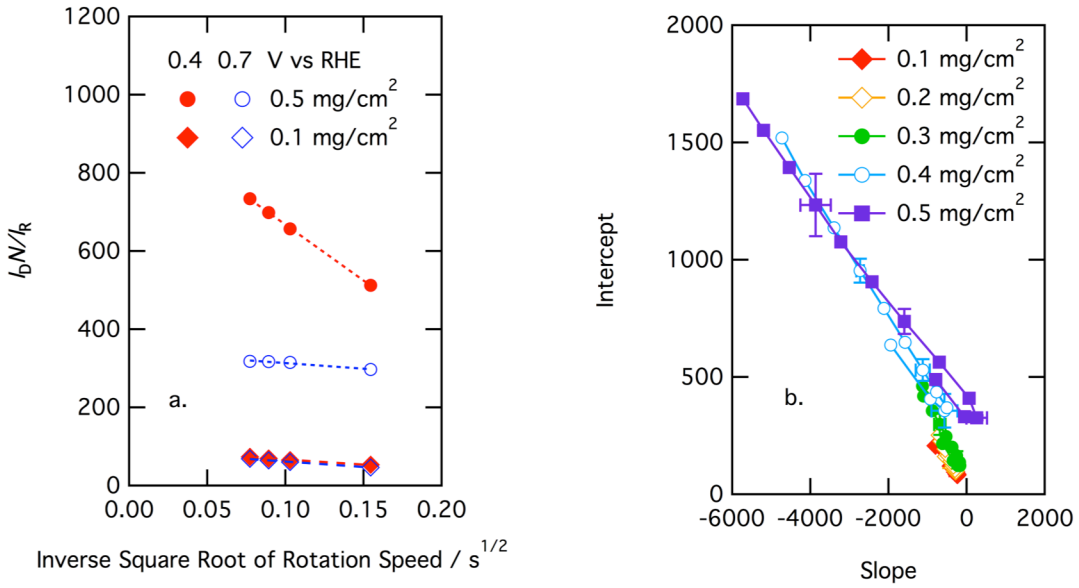

Figure 4.3: (a) Plot of $I_D N/I_R$ vs rotation speed for two different electrodes at two different potentials, 0.5 M H_2SO_4, room temperature, oxygen saturated, ring poised at 1.2 V vs. RHE. (b) Slope and intercept plot at various loadings and potentials: 0.5 M H_2SO_4, room temperature, oxygen saturated, ring poised at 1.2 V vs. RHE.

The figure of merit, $I_D N/I_R$, for the current data set was regressed with respect to the inverse square root of the rotation speed, and sample regressions are shown in Fig. 4.3a, with a plot of slope vs intercept given in Fig. 4.3b. One issue with the application of this analysis is that Eq.18 predicts a positive slope with respect to $\omega^{-1/2}$, but the data clearly show negative slope.

A requirement for the validity of Eq. 2 is first order kinetics.[5] In order to test this requirement, the variation of disk and ring currents with oxygen concentration is explored as shown in Fig. 4.4. Assuming a Nernst boundary layer at the disk surface, C_o can be calculated from the bulk oxygen concentration and the ratio of the total reduction current at a given potential and the mass transfer limiting current:[9]

$$C_o = C_{o,b}\left(1 - \frac{I_D + I_R/N}{I_{lim}}\right) \qquad [4]$$

where $C_{o,b}$ represents oxygen concentration in the bulk electrolyte, C_o is dissolved oxygen concentration at the catalyst surface, and I_{lim} the diffusion limited current. At high potential (0.7 V vs RHE), where the peroxide reduction rate is small, $I_R \sim NI_2$. This correlation with oxygen ($I_1 \sim I_D$ and $I_2 \sim I_R/N$) shows that neither reaction pathway appears to show first order kinetics ($I \propto C_o$).

If the disk and ring currents were first order, the traces in Fig. 4.4 would be straight lines that intercept the origin. Because this is not the case, kinetics controlled by surface adsorption were explored. For single constituent adsorption, the Langmuir adsorption coefficient may be defined as: [23]

$$K_{i,j} = \frac{C_i \theta_{v,j}}{\theta_{i,j}} \quad [5]$$

where $K_{i,j}$ is the adsorption coefficient for species *i* on site *j*, $\theta_{i,j}$ is the fraction of sites occupied by species *i*, C_i is concentration of species *i* near the surface, and $\theta_{v,j}$ is the fraction of vacant sites. A mass balance on the total number of sites of type *j* yields:

$$1 = \theta_{v,j} + \sum_i \theta_{i,j} \quad [6]$$

Then $\theta_{v,j}$ can be solved for and substituted into the adsorption equations to obtain the surface fractions. For a single adsorbent this results in:

$$\theta_{i,j} = \frac{C_i}{K_{i,j} + C_i} \quad [7]$$

If an electrochemical reaction is first order with respect to the surface species, $\theta_{i,j}$, reaction rate laws can be written as a current:

$$i = \frac{nFkC_{\mathrm{i}}}{K_{\mathrm{i,j}} + C_{\mathrm{i}}} \qquad [8]$$

where k is a rate constant, and nFk represents a plateau current density when $C_{\mathrm{o}} \gg K_{\mathrm{o,j}}$, *i.e.* when the surface is saturated.

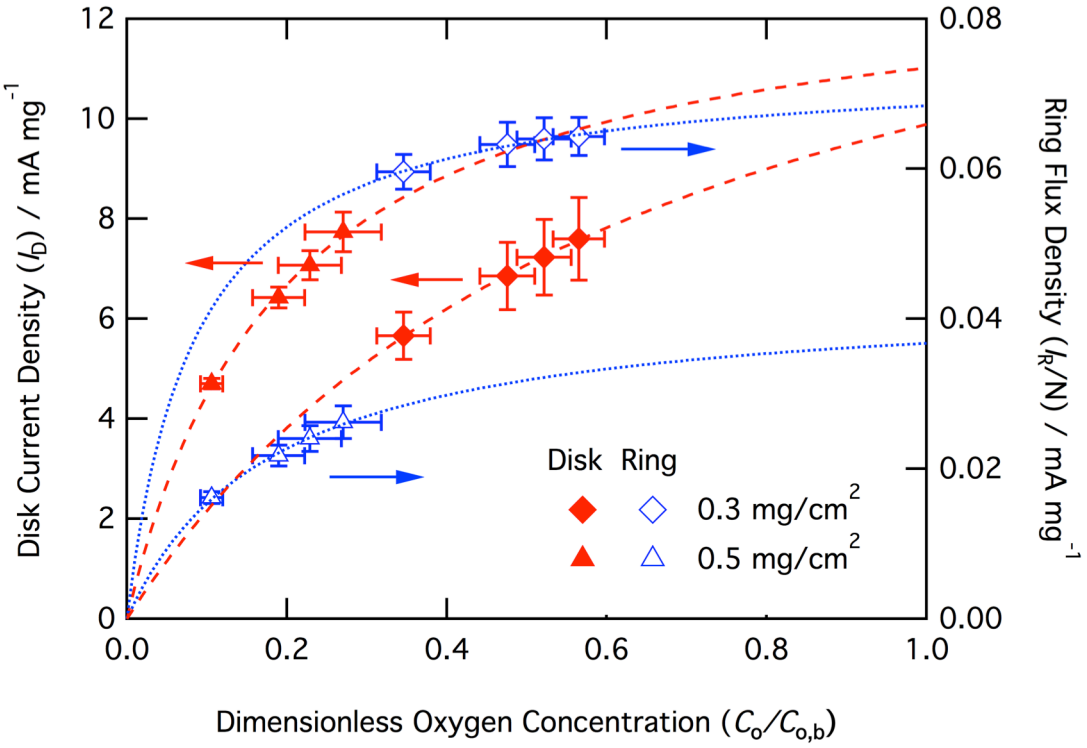

Figure 4.4: Plot of disk and ring current densities vs oxygen concentration (varying rotation speed) for two different loadings at 0.7 V vs RHE, 0.5 M H_2SO_4, room temperature, oxygen saturated, ring poised at 1.2 V vs. RHE. Dashed lines represent fit of Eq. 8.

Returning to Fig. 4.4, one can see that Eq. 8 fits the experimental data well. The data are therefore well explained by a site-limited surface reaction, because the current density plateaus as C_0 increases. As mentioned earlier, a high potential was chosen for Fig. 4.4 to minimize rate 3 (peroxide reduction). The small rate three allows comparison between oxygen adsorption on the direct $4e^-$ and indirect $2e^-$ active sites. The smaller variation with oxygen concentration in the ring current (representing peroxide generation) as compared to the disk current (dominated by $4e^-$ oxygen reduction) suggests that the $2e^-$ sites are more saturated than the $4e^-$ sites.

One can extend the analysis to lower potentials for the disk current, assuming that I_l dominates. Disk current is plotted vs. oxygen concentration at 0.5 V vs RHE in Fig. 4.5; the disk current displays more linear kinetics, suggesting that the surface concentration is low, $C_o \ll K_{o,j}$.

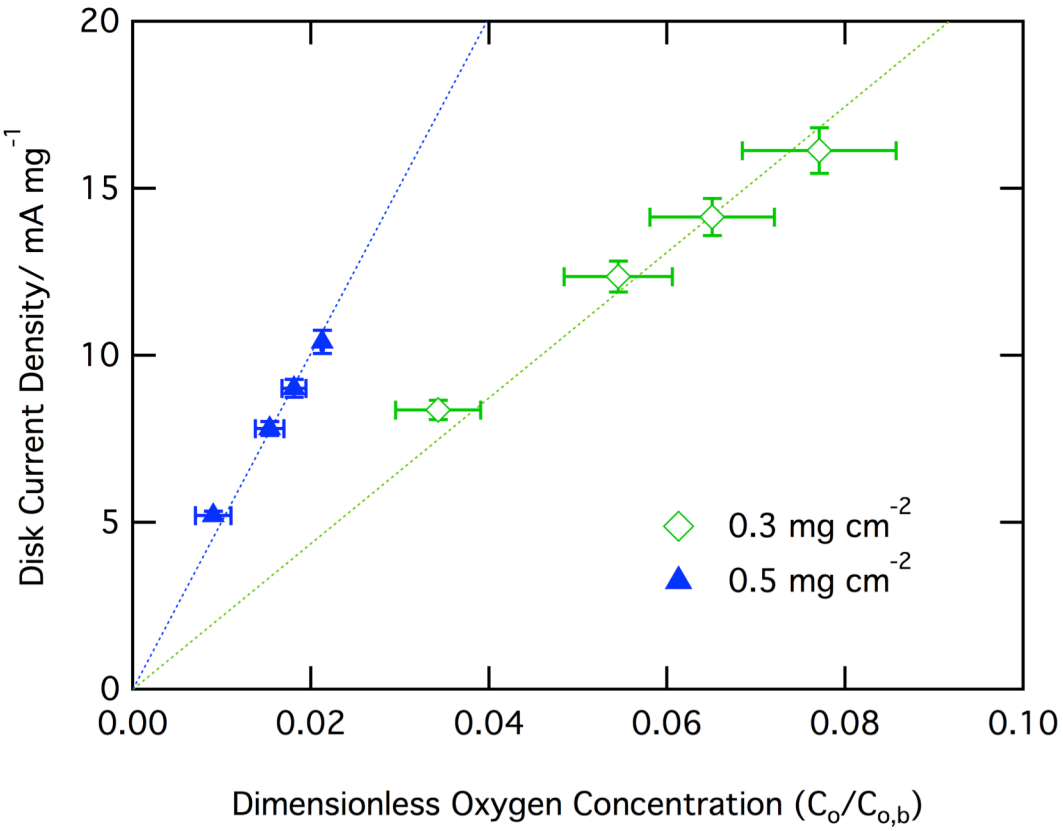

Figure 4.5: Plot of disk current density vs oxygen concentration (varying rotation speed) for two different loadings at 0.5 V vs RHE, 0.5 M H_2SO_4, room temperature, oxygen saturated, ring poised at 1.2 V vs. RHE.

The observed adsorption limitation and resulting nonlinear kinetics do not satisfy the requirements for Eq. 2. For this reason, the RRDE data must be reanalyzed assuming Langmuir-Hinshelwood kinetics. In this analysis we will assume that the two reduction pathways occur on different sites. As shown in Fig. 4.1, site one is responsible for direct $4e^-$ reduction of oxygen to water, while site two is responsible for the indirect, $2e^- + 2e^-$ reduction pathway via peroxide. We will obtain an expression for parameter C_oN/I_R, where C_O is calculated by Eq. 4, and will assume that the rate peroxide generation by reaction 2 is first order with respect to oxygen

concentration. Initially, the method will be established assuming linear kinetics (no adsorption limitations), and then extended to consider Langmuir adsorption. For the initial analysis, with linear kinetics ($C_o \ll K_{o,j}$) The two-electron oxygen reduction current I_2 may be expressed as:

$$I_2 = \frac{nFk_2C_o}{K_{o,2}} \quad [9]$$

where k_2 is the associated rate constant, $K_{o,2}$ is the adsorption equilibrium coefficient for 2+2 pathway surface sites (site 2), and C_o is oxygen concentration given by Eq. 4. The ring current, I_R, is related to the concentration of peroxide, C_p at the disk by a Levich-like transport model:[6,8-10]

$$I_R = nFNC_p z_p \omega^{1/2} \text{, where } \quad z_i = 0.62 D_i^{2/3} \nu^{1/6} \quad [10]$$

where n is the number of electrons per mole oxygen, F is Faraday's constant, D the diffusivity, v the viscosity, and ω the rotation speed. An equation for I_3 with respect to ring current can be developed by assuming that I_3, i.e. the further reduction of peroxide to water is first order with respect to peroxide concentration at the disk:

$$I_3 = \frac{nFk_3}{K_{p,2}} C_p = \frac{k_3}{K_{p,2}} \frac{I_R \omega^{-1/2}}{z_p N} \quad [11]$$

where $K_{p,2}$ is the adsorption coefficient of peroxide on site two. Eqns. 9 and 11 provide rate expressions for each step associated with the two-by-two reaction pathway (I_2 and I_3) with the only parameters being three rate constant groups ($k_2/K_{o,2}$, $k_3/K_{p,2}$) and mass transport properties.

A charge balance on peroxide generation/consumption relates the ring current to I_2 and I_3:

$$I_2 = \frac{I_R}{N} + I_3 \quad [12]$$

Here we have neglected bulk disproportionation of peroxide. Combining equations 12 and 11 allows I_2 to be represented as a function of the ring current and some reaction coefficient $k_3/K_{p,2}$:

$$I_2 = \frac{I_R}{N}\left(\frac{k_3}{K_{p,2} z_p}\omega^{-1/2} + 1\right) \quad [13]$$

Rearranging Eq. 13 and introducing C_o via Eq. 9 yields:

$$\frac{C_o N}{I_R} = \frac{K_{o,2} k_3}{nF k_2 K_{p,2} z_p}\omega^{-1/2} + \frac{K_{o,2}}{nF k_2} \quad [14]$$

In the absence of adsorption limitations, the term $k_2/K_{o,2}$ can then be calculated from a regression of C_oN/I_R with rotation speed, allowing the calculation of I_2 via Eq. 9. Based on the earlier analysis of Fig. 4, the present data indicate limitations due to oxygen adsorption. Therefore, an adsorption model must be incorporated into the reaction system.

For oxygen and peroxide, the Langmuir adsorption coefficients, $K_{o,2}$ and $K_{p,2}$, may be defined as:[24]

$$K_{o,2} = \frac{C_o \theta_{v,2}}{\theta_{o,2}}; K_{p,2} = \frac{C_p \theta_{v,2}}{\theta_{p,2}} \quad [15]$$

where $\theta_{o,2}$ and $\theta_{p,2}$ are the surface fractions of oxygen and peroxide respectively on the sites involved in indirect ORR pathway (site 2), $\theta_{v,2}$ is the surface availability of this adsorption site, and C_o, C_p are oxygen and peroxide concentrations near the surface. If the reactions two and three are first order with respect to the surface species ($\theta_{o,2}$ and $\theta_{p,2}$) the rate laws can be re-written:

$$I_2 = \frac{nF k_2 \theta_{v,2} C_o}{K_{o,2}} \quad [16]$$

$$I_3 = \frac{nFk_3\theta_{v,2}C_p}{K_{p,2}} \quad [17]$$

Using these rate laws, Eq. 14 becomes:

$$\frac{C_o N}{I_R} = \frac{K_{o,2}k_3}{nFk_2K_{p,2}z_p}\omega^{-1/2} + \frac{K_{o,2}}{nFk_2\theta_{v,2}} \quad [18]$$

Assuming that the surface fractions of oxygen and peroxide are small (that is $\theta_{v,2}$ is near unity) the equation reduces to Eq. 14.

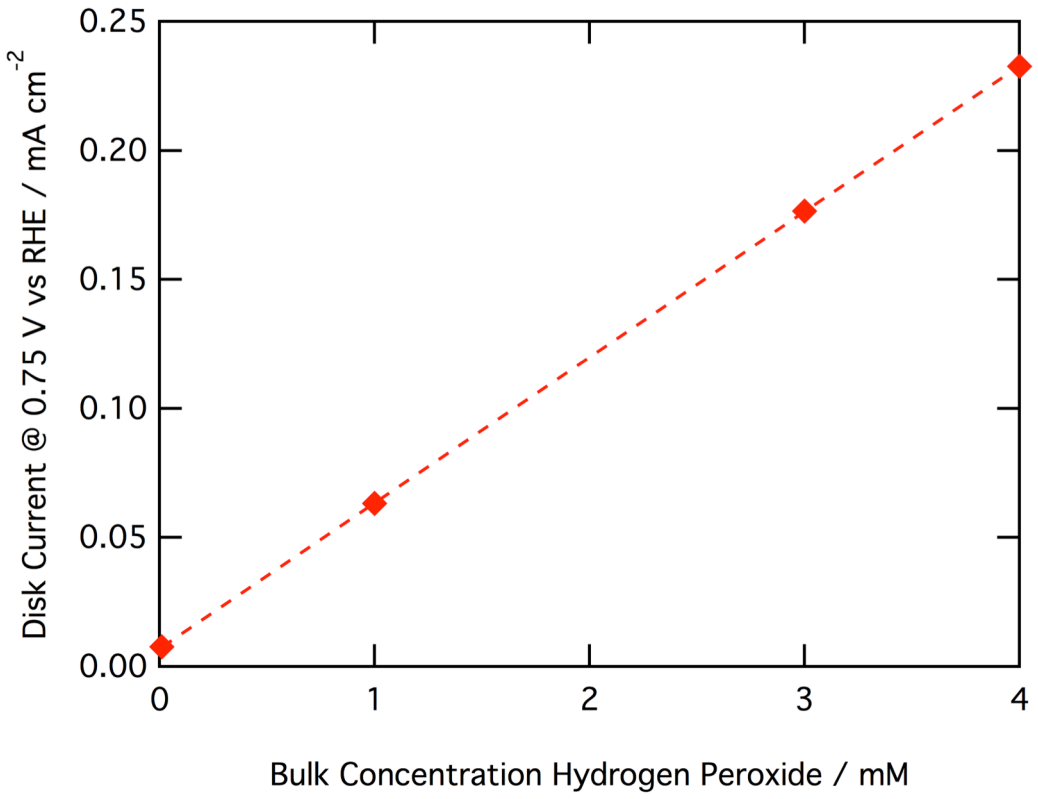

Figure 4.6: Correlation of disk current with hydrogen peroxide concentration showing first-order peroxide reduction reaction: slope is 0.0564 ± 0.0007 mA cm^{-2} mM^{-1}. Hydrogen peroxide concentrations range from 10 μM to 4 mM in 0.5 M H_2SO_4: room temperature, nitrogen saturated.

Peroxide reduction experiments were performed by running the same RRDE experiment as above, but in the presence of various concentrations of hydrogen peroxide and saturated with nitrogen. By plotting the current at a given potential as a function of peroxide concentration, the

presence of adsorption limitations associated with peroxide reduction can be studied. As demonstrated in Fig. 4.6, in the absence of oxygen, the observed peroxide reduction rate is linearly dependent on bulk hydrogen peroxide concentration at least to 4 mM. This suggests that $K_{p,2}$ is large and adsorbed peroxide does not contribute significantly to surface coverage. Considering this approximation, surface fractions for site 2 become $\theta_{v,2} + \theta_{o,2} = 1$, and Eq. 18 becomes:

$$\frac{C_o N}{I_R} = \frac{K_{o,2} k_3}{nF k_2 K_{p,2} z_p} \omega^{-1/2} + \frac{C_o + K_{o,2}}{nF k_2} \quad [19]$$

Additionally, at high potentials where I_3 is insignificant, Eq. 19 simplifies to

$$\frac{C_o N}{I_R} = \frac{C_o + K_{o,2}}{nF k_2} \quad [20]$$

In these cases the figure of merit $C_o N/I_R$ should scale with C_o. Some representative correlations are shown in Fig. 4.7a. For this correlation the ratio of the intercept to slope indicates an adsorption coefficient, and the inverse slope represents a rate constant. The resulting reaction parameters $K_{o,2}$ and k_2 are shown in Fig. 4.7b as a function of potential. At low loading and high potentials, $K_{o,2}$ does not vary with potential, while k_2 varies exponentially with potential. These characteristics indicate potential independent adsorption and Tafel kinetics. At high loading and low pressure $K_{o,2}$ decreases and k_2 becomes less potential dependent, likely caused by the onset of I_3. By fitting rate parameters in the Tafel region, rate parameters can be established. These rate parameters can be used to calculate surface coverage and I_2. Charge balances can be applied to deduce I_1 and I_3.

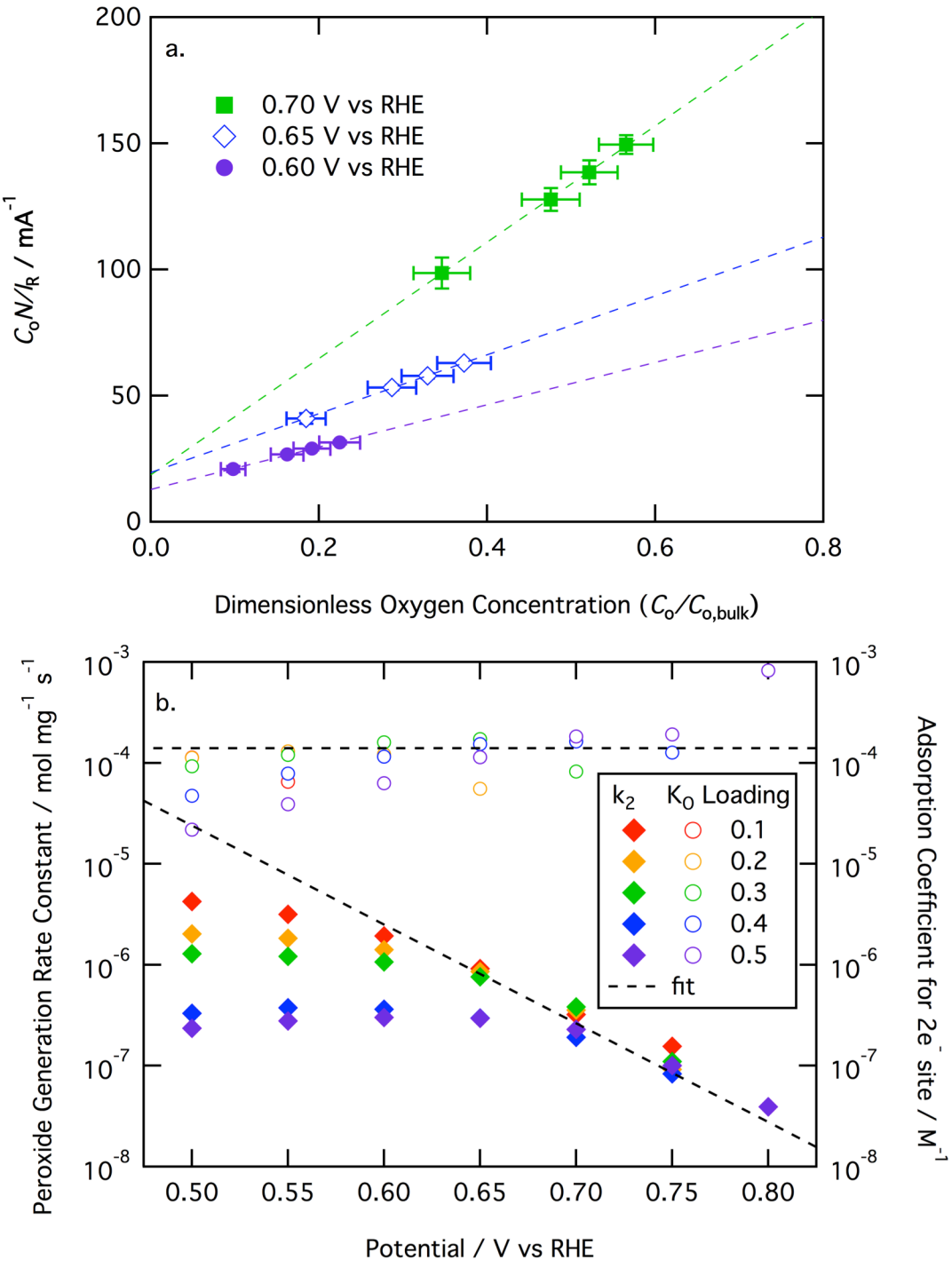

Figure 4.7: (a) Plot of C_oN/I_R vs oxygen concentration at four high potentials with 0.3 mg/cm^2 loading, 0.5 M H_2SO_4, room temperature, oxygen saturated, ring poised at 1.2 V vs. RHE. (b) Plot of peroxide generation parameters k_2 and $K_{o,2}$ at various loadings and potentials. Reaction parameters are: $K_{o,2}$ = 1.7e-4 ± 1.1e-4 M, k_2 = 4.3e-8 ± 0.8e-8 mol s^{-1} mg^{-1} and the Tafel slope is 114 ± 6 mV per decade. Conditions: 0.5 M H_2SO_4, room temperature, oxygen saturated, ring poised at 1.2 V vs. RHE.

Surface coverage at various potentials can be compared as shown in Fig. 4.8. Surface coverage was calculated via the definition of the adsorption coefficient (Eq. 15) and a mass balance on adsorption sites ($1 = \theta_{v,2} + \theta_{o,2}$):

$$\theta_{o,2} = \frac{C_o}{C_o + K_{o,2}}; \theta_{v,2} = \frac{K_{o,2}}{C_o + K_{o,2}} \quad [21]$$

As shown in Fig. 4.8, For 0.1 mg cm^{-2} loading, oxygen surface coverage remains above 70% down to 0.6 V vs RHE. Low surface coverage at 0.5 mg cm^{-2} indicates that the high loadings approach mass-transfer-limiting current faster than lower loadings. This is an indication of high catalyst utilization.

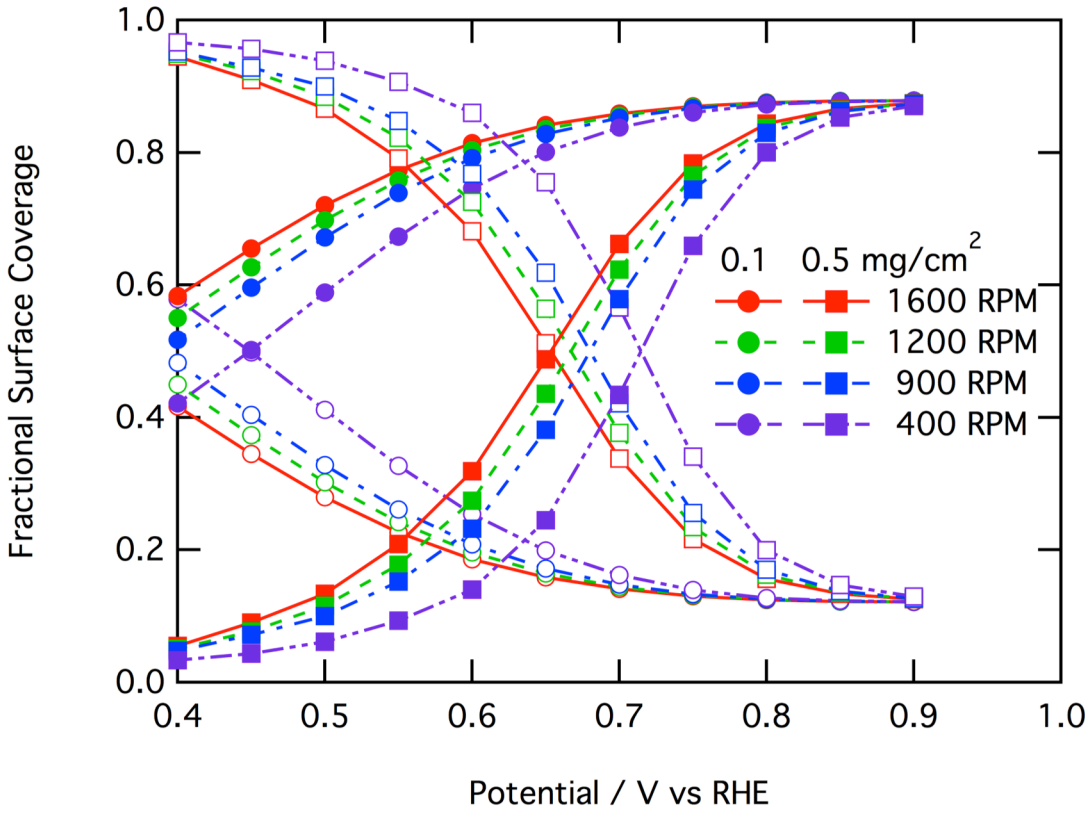

Figure 4.8. Fractional surface coverage at two different loadings and at various rotation speeds. Open symbols represent vacant sites, while filled symbols represent occupied sites.

The currents for each reaction step can also be compared. Fig. 4.9 shows currents I_1, I_2, and I_3 cumulatively as compared to disk current. It is evident that at high potentials I_1 dominates, but I_2 becomes significant below 0.7 V and I_3 below 0.6 V. The fact that I_1 dominates over most of the potential range justifies the use of disk current as a proxy for I_1, as was assumed in the context of Fig. 4.4.

The adsorption limitation may be why I_2 is not significant at higher potentials: at high potential, oxygen surface concentration is high and available sites for adsorption limit the 2+2 reaction pathway. At low potential oxygen concentration and surface coverage are mass transfer limited, decreasing adsorption limitations. At these low potentials the 2+2 reaction pathway can compete better with the direct 4-electron pathway.

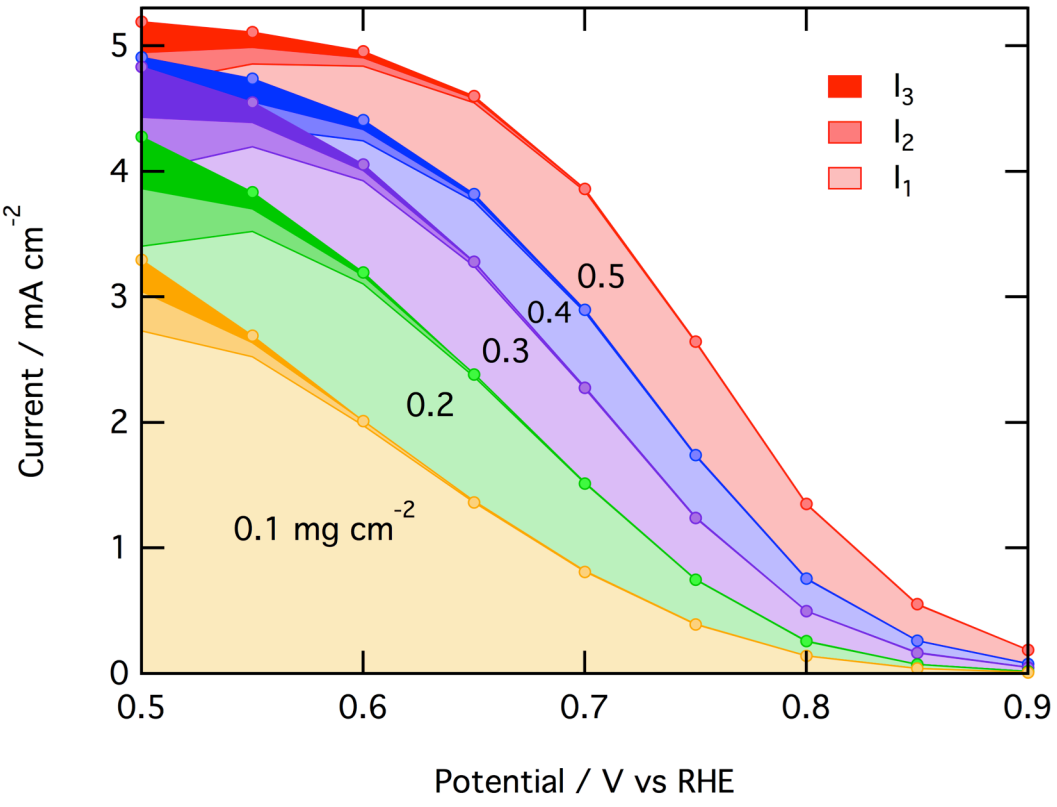

Figure 4.9: Polarization curve showing contributions of I_1, I_2, and I_3 with experimental I_D.values for various loadings at 1600 RPM.

4.5 Conclusions

An RRDE study indicates that oxygen reduction on this autogenic-pressure MNC catalyst proceeds primarily through the direct four-electron pathway to water. Langmuir-Hinschelwood analysis suggests that the indirect 2+2 pathway active sites are more saturated with surface species.

A second conclusion is that $4e^-$ and $2e^-$ oxygen reduction occur at different sites that compete for oxygen in the catalyst layer. This is illustrated in the difference in adsorption behaviors between the disk current and ring current. The variance of disk and ring current with oxygen, as discussed with relation to Fig. 4.4, indicates that the $2e^-$ adsorption site is more saturated than the $4e^-$ site. Furthermore, correlations between peroxide generation and oxygen concentration indicate that peroxide generation is significantly adsorption limited.

Together, these main conclusions show a more complete picture of oxygen reduction and peroxide generation on MNC catalysts: the onset of peroxide generation occurs around its redox potential of 0.8 V vs RHE with fast kinetics driving a sharp increase in peroxide generation. Although the peroxide generation does not require a large over-potential, low site availability keeps the ring current small. As the potential decreases further, the combination of increasing over-potential and increasing peroxide surface concentration causes a dramatic increase in ring current. Below 0.6 V a second reduction step scavenges the peroxide on the catalyst surface decreasing the flux of peroxide from the catalyst layer.

4.6 Acknowledgments

We gratefully acknowledge the partial financial support from the U.S. Department of Energy (EERE), under a Non PGM Catalyst development effort (Contract no EE 0000459) lead by Northeastern University (Sanjeev Mukerjee, P.I.).

REFERENCES

REFERENCES

1. R. Kothandaraman, V. Nallathambi, K. Artyushkova and S. C. Barton, "Non-precious oxygen reduction catalysts prepared by high-pressure pyrolysis for low-temperature fuel cells," *Applied Catalysis B Environmental,* **92**(1-2), 209-216 (2009). doi:10.1016/J.Apcatb.2009.07.005

2. M. Bron, S. Fiechter, M. Hilgendorff and P. Bogdanoff, "Catalysts for oxygen reduction from heat-treated carbon-supported iron phenantroline complexes," *Journal of Applied Electrochemistry,* **32**(2), 211-216 (2002). doi:10.1023/a:1014753613345

3. H. T. Chung, C. M. Johnston, K. Artyushkova, M. Ferrandon, D. J. Myers and P. Zelenay, "Cyanamide-derived non-precious metal catalyst for oxygen reduction," *Electrochemistry Communications,* **12**(12), 1792-1795 (2010). doi:10.1016/j.elecom.2010.10.027

4. E. Yeager, "Electrocatalysts for O-2 Reduction," *Electrochimica Acta,* **29**(11), 1527-1537 (1984).

5. N. A. Anastasijevic, V. Vesovic and R. R. Adzic, "Determination of the kinetic parameters of the oxygen reduction reaction using the rotating ring-disk electrode: Part I. Theory," *Journal of Electroanalytical Chemistry and Interfacial Electrochemistry,* **229**(12), 305-316 (1987). doi:10.1016/0022-0728(87)85148-3

6. N. Anastasijević, V. Vesović and R. Adžić, "Determination of the kinetic parameters of the oxygen reduction reaction using the rotating ring-disk electrode: Part II. Applications," *Journal of electroanalytical chemistry and interfacial electrochemistry,* **229**(1), 317-325 (1987).

7. F. Jaouen, "O2 Reduction Mechanism on Non-Noble Metal Catalysts for PEM Fuel Cells. Part II: A Porous-Electrode Model To Predict the Quantity of H2O2 Detected by Rotating Ring-Disk Electrode," *The Journal of Physical Chemistry C,* **113**(34), 15433-15443 (2009).

8. H. S. Wroblowa, P. Yen Chi and G. Razumney, "Electroreduction of oxygen: A new mechanistic criterion," *Journal of Electroanalytical Chemistry and Interfacial Electrochemistry,* **69**(2), 195-201 (1976). doi:10.1016/S0022-0728(76)80250-1

9. K. L. Hsueh, D. T. Chin and S. Srinivasan, "Electrode kinetics of oxygen reduction: A theoretical and experimental analysis of the rotating ring-disc electrode method," *Journal of Electroanalytical Chemistry and Interfacial Electrochemistry,* **153**(1), 79-95 (1983). doi:10.1016/S0022-0728(83)80007-2

10. A. Damjanovic, M. A. Genshaw and J. O. M. Bockris, "The Role of Hydrogen Peroxide in the Reduction of Oxygen at Platinum Electrodes," *The Journal of Physical Chemistry,* **70**(11), 3761-3762 (1966). doi:10.1021/j100883a515

11. A. J. Bard and L. R. Faulkner, *Electrochemical methods : fundamentals and applications,*(John Wiley, New York, 2000).

12. T. S. Olson, S. Pylypenko, J. E. Fulghum and P. Atanassov, "Bifunctional Oxygen Reduction Reaction Mechanism on Non-Platinum Catalysts Derived from Pyrolyzed Porphyrins," *Journal of the Electrochemical Society,* **157**(1), B54-B63 (2010). doi:Doi 10.1149/1.3248003

13. A. Bonakdarpour, M. Lefevre, R. Z. Yang, F. Jaouen, T. Dahn, J. P. Dodelet and J. R. Dahn, "Impact of loading in RRDE experiments on Fe-N-C catalysts: Two- or four-electron oxygen reduction?," *Electrochemical and Solid State Letters,* **11**(6), B105-B108 (2008). doi:10.1149/1.2904768

14. N. Guillet, L. Roue, S. Marcotte, D. Villers, J. P. Dodelet, N. Chhim and S. Trevin, "Electrogeneration of hydrogen peroxide in acid medium using pyrolyzed cobalt-based catalysts: Influence of the cobalt content on the electrode performance," *Journal of Applied Electrochemistry,* **36**(8), 863-870 (2006).

15. S. Marcotte, D. Villers, N. Guillet, L. Roue and J. P. Dodelet, "Electroreduction of oxygen on Co-based catalysts: determination of the parameters affecting the two-electron transfer reaction in an acid medium," *Electrochimica Acta,* **50**(1), 179-188 (2004).

16. N. Leonard, V. Nallathambi and S. C. Barton, "Carbon Supports for Non-Precious Metal Oxygen Reducing Catalysts," *Journal of the Electrochemical Society,* **160**(8), F788-F792 (2013). doi:10.1149/2.026308jes

17. M. H. Robson, A. Serov, K. Artyushkova and P. Atanassov, "A Mechanistic Study of 4-Aminoantipyrine and Iron Derived Non-Platinum Group Metal Catalyst on the Oxygen Reduction Reaction," *Electrochimica Acta* (2012).

18. V. Nallathambi, N. Leonard, R. Kothandaraman and S. Calabrese Barton, "Nitrogen Precursor Effects in Iron-Nitrogen-Carbon Oxygen Reduction Catalysts," *Electrochemical and Solid State Letters,* **14**(6), B55-B58 (2011). doi:10.1149/1.3566065

19. U. A. Paulus, T. J. Schmidt, H. A. Gasteiger and R. J. Behm, "Oxygen reduction on a high-surface area Pt/Vulcan carbon catalyst: a thin-film rotating ring-disk electrode study," *Journal of Electroanalytical Chemistry,* **495**(2), 134-145 (2001).

20. E. Claude, T. Addou, J. M. Latour and P. Aldebert, "A new method for electrochemical screening based on the rotating ring disc electrode and its application to oxygen reduction catalysts," *Journal of Applied Electrochemistry,* **28**(1), 57-64 (1998).

21. K. E. Gubbins and R. D. Walker, "The solubility and diffusivity of oxygen in electrolytic solutions," *Journal of The Electrochemical Society,* **112**(5), 469-471 (1965).

22. W. M. Haynes (ed.) *CRC Handbook of Chemistry and Physics* (CRC Press, 2010).

23. D. M. H. Kern, "The Polarography and Standard Potential of the Oxygen-Hydrogen Peroxide Couple," *Journal of the American Chemical Society,* **76**(16), 4208-4214 (1954). doi:10.1021/ja01645a059

24. H. S. Fogler, *Elements of Chemical Reaction Engineering,*(PHI Learning Private Limited, New Dehli, 2009).

Chapter 5. Modeling Low-Temperature Fuel Cell Electrodes using Non-precious Metal Catalysts[1]

5.1. Abstract

An electrode-scale, transport model for a proton-exchange-membrane fuel cell (PEMFC) cathode is presented. The model describes the performance of non-precious metal catalysts for the oxygen reduction reaction in a fuel cell context. Because of its relatively high thickness, emphasis is placed on phenomena occurring in the cathode layer. Water flooding is studied in terms of its impact on gas-phase transport and on electrochemically accessible surface area (ECSA). Although cathode performance in both air and oxygen are susceptible to ECSA loss, gas diffusion limitations at high current density in air are more significant. In oxygen, catalyst utilization at high current density is primarily limited by conductivity. For this reason, air fuel cell data is recommended over oxygen data for characterizing catalyst performance. Due to both ohmic and mass transport limitations, increased loading of low-cost catalysts does not necessarily lead to higher performance. Therefore, careful optimization of catalyst layer thickness is required.

---

[1] Authors: Nathaniel D. Leonard,[1]* Kateryna Artyushkova,[2] Barr Halevi,[3] Alexey Serov,[2] Plamen Atanassov,[2] Scott Calabrese Barton[1]

[1]*Department of Chemical Engineering and Materials Science, Michigan State University, East Lansing, MI 48824(USA)*
[2]*University of New Mexico, Chemical & Nuclear Engineering Department, UNM Center for Emerging Energy Technologies, University of New Mexico, Albuquerque, NM 87131 (USA)*
[3]*Pajarito Powder, Albuquerque, NM 87102 (USA*

5.2. Introduction

The high environmental costs of current energy systems drives a search for commercializable energy technologies with low carbon footprints. Proton exchange membrane fuel cells present one energy option for transportation applications. A significant impediment to commercialization has been the cost and availability of catalysts for the oxygen reduction reaction (ORR) due to prevalent use of platinum group metals (PGM). Metal-Nitrogen-Carbon (MNC) catalysts are a potential solution to the cost and availability challenges that come with using PGMs. MNC catalysts are synthesized by mixing metal, carbon, and nitrogen precursors followed by one or more pyrolysis steps at 700-900 C.[1-7] Such MNC catalysts are generally washed in acid to remove excess metal precursors.[1-5] These catalysts generally involve lower volume-specific activity than platinum, which results in thicker electrodes. It has been previously proposed that a low-cost catalyst may be allowed to have 10-fold lower activity than platinum, as long as the catalyst layer was 10-fold thicker.[8] This proposal was based on the assumption that transport loses would not be significant in this thickness regime. The purpose of this paper is to understand quantitatively how the thickness of these electrodes will impact membrane electrode assembly (MEA) performance for MNC catalyst.

A number of models have addressed electrode scale transport issues.[9-15] These models generally concentrate on water flooding in the gas diffusion layer (GDL) and consider a relatively thin catalyst layer. Here, gas and liquid transport in the catalyst layer are considered in a way that is similar to treatment of gas diffusion layers in previous models. We also treat the GDL consistently with previous models.

Multiple works have considered the catalyst layer.[16-22] These works have primarily concentrated on thin catalyst layers that do not provide significant gas diffusion limitations in

comparison to the GDL. For this reason these works concentrate on how flooding impacts electrochemically active surface area (ECSA). Here, we consider the impact of flooding on ECSA in addition to gas diffusion. The ECSA impact is considered by incorporating a flooding term in the kinetics model similar to Eikerling et al.[20] Treatment of gas diffusion limitations are based on the decrease in effective porosity due to flooding, as well as the dilution of oxygen by to water vapor and nitrogen, similar to the treatment of the GDL by Weber et al.[11] This second consideration is likely more significant than in thin Pt-based catalyst layers due to increased catalyst layer thickness as well as the increased hydrophilicity that can accompany heat-treated carbon materials.

5.3. Experimental

5.3.1 Materials

Catalysts were synthesized by Pajarito Powder using a scaled up proprietary method similar to the work by Serov et al.[23] To summarize, a silica template material is thoroughly mixed with iron nitrate and various nitrogen precursors. After pyrolyzing the mixture, the silica template is removed by etching in hydrofluoric acid. A second pyrolysis follows etching.

5.3.2 MEA Fabrication

Catalyst ink containing a 9:11 mass ratio of ionomer to catalyst with 500 mg catalyst per 20 mL solvent was sprayed on a 5 cm^2 Sigracet 25BC GDL using a Sono-tek Exacta-Coat automated spray system. The catalyst layer (CL) plus GDL was assembled with a 211 membrane and an anode containing 0.2 mg_{Pt}/cm^2. This assembly was hot pressed at 131°C and 90 psi for six minutes.

5.3.3 Electrochemical Characterization

MEAs, fabricated as explained in previous section, were loaded onto single serpentine pattern graphite flow plates and assembled with 4.5 N torque. The cells was allowed to equilibrate under a feed of 200 sccm, 1.5 bar total pressure. After reaching a temperature of 80 °C, they were broken in by holding for 15 minutes at 0.3 and 0.6 V. MEA activity was measured potentiostatically at various backpressures over a potential range from open-circuit voltage (OCV) to 0.3 V, and then back to OCV. At each potential, a current was recorded after a one minute hold, and a high frequency resistance measurement was recorded. The MEA was poised at 0.6 V for 15 minutes between polarization measurements. For additional break-in, an initial polarization from OCV to 0.3 V and back was discarded. Inlet gases were hydrogen and air at 100% relative humidity and 200 sccm.

5.3.4 Physical Characterization

Catalyst layer material for physical characterization was created by spraying the catalyst ink onto a glass plate. Catalyst ink contained a 9:11 mass ratio of ionomer to catalyst with 500 mg catalyst per 20 mL solvent. After the material was dry, it was scraped of and used for porosity measurements.

The pore size distribution (PSD) of catalyst layer material was measured via mercury intrusion porosimetry (Micromeritics AutoPore IV 9500.) A 3 mL penetrometer with a stem volume of 1.1 mL was loaded with 0.1 g of CL material. Mercury intrusion was measured over

the pressure range of 0.1 to 30000 psi_a. The pressure is related to a pore radius with the Washburn equation:[24]

$$r_{\mathrm{p}} = \frac{2\gamma \cos\theta}{p_{\mathrm{meas}}} \qquad [1]$$

where the measured pressure, p_{meas}, contact angle, θ, and surface tension of mercury, γ, establish the pore radius, r_p. In this way the change in mercury volume from one pressure to another can be associated with intrusion into a certain pore size and a pore size distribution can be calculated.

5.4. Model Description

5.4.1 Overview

This section describes the governing equations for a two-region, multi-phase, transport model of an electrolyte membrane - catalyst layer (CL) - gas diffusion layer (GDL) assembly. This one-dimensional, steady-state model consists of two regions (CL and GDL) with the electrolyte membrane being considered as a boundary condition at the CL surface (Figure 5.1). Each region has different properties, but the governing equations are similar.

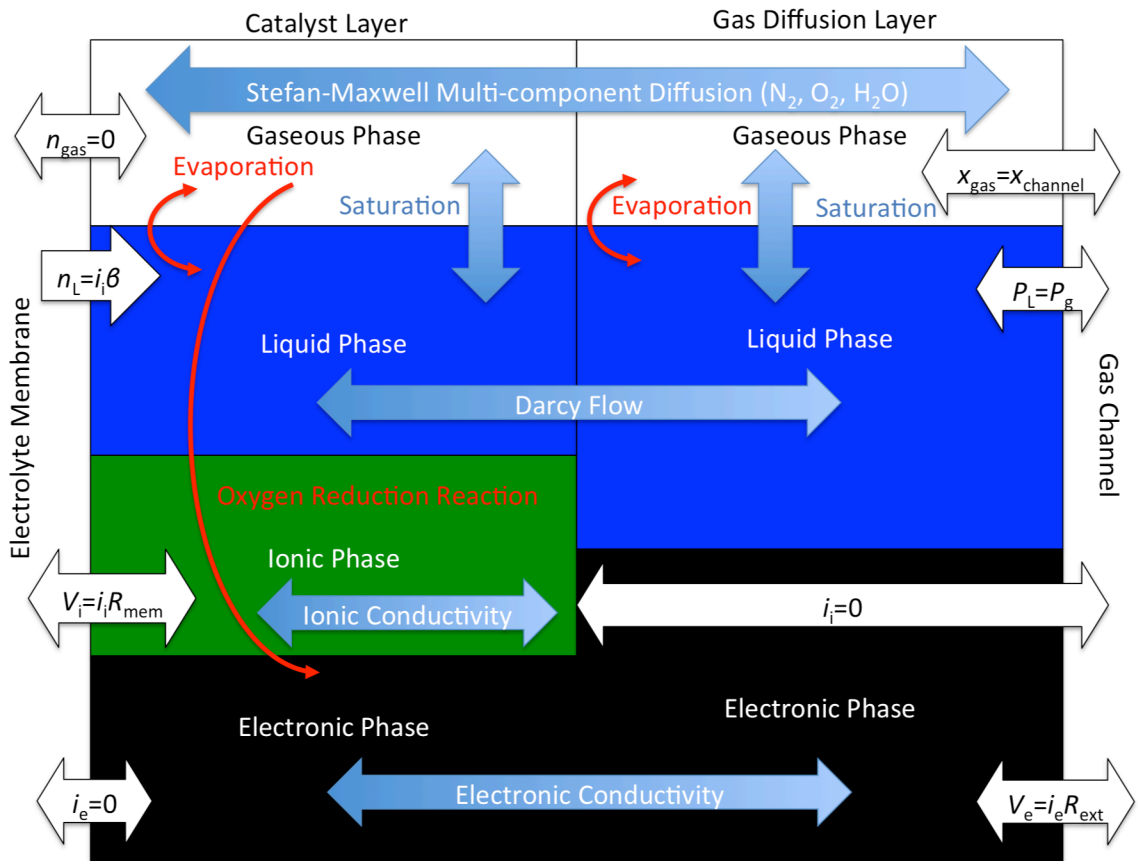

Figure 5.1: Schematic of cathode showing different phases and regions of the model with boundary conditions (black-outlined, white arrows), transport phenomena (blue arrows), and generation terms (red arrows).

Within each region there are four phases: an electron-conducting solid phase, an ion-conducting ionic phase, and non-conducting liquid and gas phases. The primary dependent variables in these phases are electronic phase potential, V_e, ionic phase potential, V_i, liquid pressure, P_L; and vapor fractions of oxygen and water vapor, x_o and x_w. Currents and species flux are also dependent variables, but can all be related to gradients of primary dependent variables, as discussed in detail below. The governing equations consider the conservation of electrons, protons, liquid water, and water vapor (Equations 2, 3, 4, and 5 respectively):

$$0 = -\kappa_{\mathrm{e}} \nabla^2 V_{\mathrm{e}} + nF r_{\mathrm{ORR}} \quad [2]$$

$$0 = -\kappa_{\mathrm{i}} \nabla^2 V_{\mathrm{i}} - nF r_{\mathrm{ORR}} \quad [3]$$

$$0 = -\frac{k_{\mathrm{L}}}{\mu} \nabla^2 P_{\mathrm{L}} + 2 r_{\mathrm{ORR}} - r_{\mathrm{evap}} \quad [4]$$

$$\nabla N_{\mathrm{w}} = r_{\mathrm{evap}} \quad [5]$$

where κ_e is electronic conductivity, V_e is electronic phase potential, n is electrons per mole oxygen, F is Faraday's constant, r_{ORR} is an oxygen reduction reaction rate, κ_i is ionic conductivity, V_i is ionic potential, k_L is liquid permeability (a function of saturation), μ is viscosity, P_L is liquid pressure, r_{evap} is an evaporation rate, and N_w is flux of water vapor. Flux of nitrogen in air is set to zero everywhere, because it does not participate in any reaction, and the membrane is considered to be gas-impermeable.

Boundary conditions for the governing equations fall into three categories: membrane, CL-GDL interface, and channel (shown in Figure 5.1 in the black-outlined, white arrows). The membrane is treated as an electrical insulator (i_e =0), with ionic resistance, R_{mem}, that leads to an ohmic drop $V_i = i_i * R_{mem}$ in the electrolyte phase. Electroosmotic flux of water through the membrane is calculated based on flux coefficient, β_{mem}, via the equation: $N_L = i_i * \beta_{mem}/F$.[25,26] The coefficient is a function of pressure as discovered by Jansen and shown in Table 4.[26] The membrane is also considered gas impermeable ($N_w = N_n = N_o$ =0). At the CL-GDL interface, all variables are considered continuous. The channel boundary is treated as an ionic insulator (i_i =0), and the solid phase overpotential at the channel is $V_e = i_e * R_{ext}$ to account for external resistances

not included in this model (current collectors, contact resistances, bipolar plates, anode, and anode GDL). The resistance R_{ext} was estimated by subtracting GDL, membrane, and CL resistances from measured high frequency resistance. Using this approach, experimental data did not have to be iR corrected prior to fitting. At the channel boundary, all concentrations are fixed to bulk conditions for the inlet gas. The liquid phase pressure is in equilibrium with the gas phase pressure, making the capillary pressure zero.

5.4.2 Porous Phase

Void space in the catalyst layer consists of water-filled hydrophilic pores with contact angles less than 90°, and hydrophobic pores with contact angle $\theta_{obs} \geq 90º$, and filled by a combination of liquid and gas phases. The fraction of pores that are flooded with water is given by saturation, S, a measure of flooding. Saturation is in turn controlled by the capillary pressure, p_c, which is the pressure difference between the liquid phase and gas phase. Saturation impacts electrochemically active surface area as well as effective permeability and gas diffusivity. For hydrophilic pores, $S = 1$, because capillary pressure is always positive due to the generation of liquid water via oxygen reduction: the liquid flux results in a pressure gradient away from the channel. This gradient and boundary condition ensure all liquid pressures are greater than the gas pressure, which is considered constant and equal to the channel gas pressure.

In order consider hydrophobic pores, a contact angle is required. The contact angle was measured to be 108 ± 5° based on the average and standard deviation of eight contact angle measurements. For hydrophobic pores, the capillary pressure, p_c, apparent contact angle, θ_{obs}, and surface tension of water, γ, define a critical pore radius, r_c, via the Washburn equation:[10,11,27,28]

$$r_{\mathrm{c}} = \frac{2\gamma \cos\theta_{\mathrm{obs}}}{p_{\mathrm{c}}} \qquad [6]$$

The saturation, *S*, of hydrophobic pores can be calculated by summing the volume of pores larger than the critical radius, r_{c}. This can be performed via an integration of the pore size distribution:[10]

$$S = \frac{\int_{r_c}^{\infty} \frac{dV}{dr} dr}{\int_{0}^{\infty} \frac{dV}{dr} dr} \qquad [7]$$

Essentially, as capillary pressure increases, water is forced into increasingly smaller pore sizes. Although direct integration of a measured pore size distribution (PSD) is achievable, a set of log-normal PSDs (LNPSDs) can be used to describe the PSD to make further calculations more manageable.[11] The use of lognormal PSDs also allows a means to differentiate pore modes. From the PSDs shown in Figure 5.2 it is evident that there are three different characteristic pore sizes: a small narrow pore size around 5 nm radius and a broad pore mode at around 300 nm radius (for neat catalyst) with a shoulder representing another characteristic pore size at a slightly smaller radius (at 100 nm for neat catalyst). Performing porosimetry of pellets composed of catalyst layer material (containing ionomer) allows the impact of the ionomer on porosity to be observed. By comparing porosity with and without ionomer it is evident that ionomer content primarily impacts macroporous and larger mesopores. The deviation between the two curves occurs around 25 nm pore radius which agrees well with literature values indicating that ionomer agglomerate size is about 40 nm diameter.[29] Furthermore, a large portion of the porosity, ~80%, is situated initially in macropores, and with the addition of ionomer the overall macroporosity decreases as well as the size of the macropores. This indicates that the macropores are covered with an ionomer film reducing the effective pore diameter.

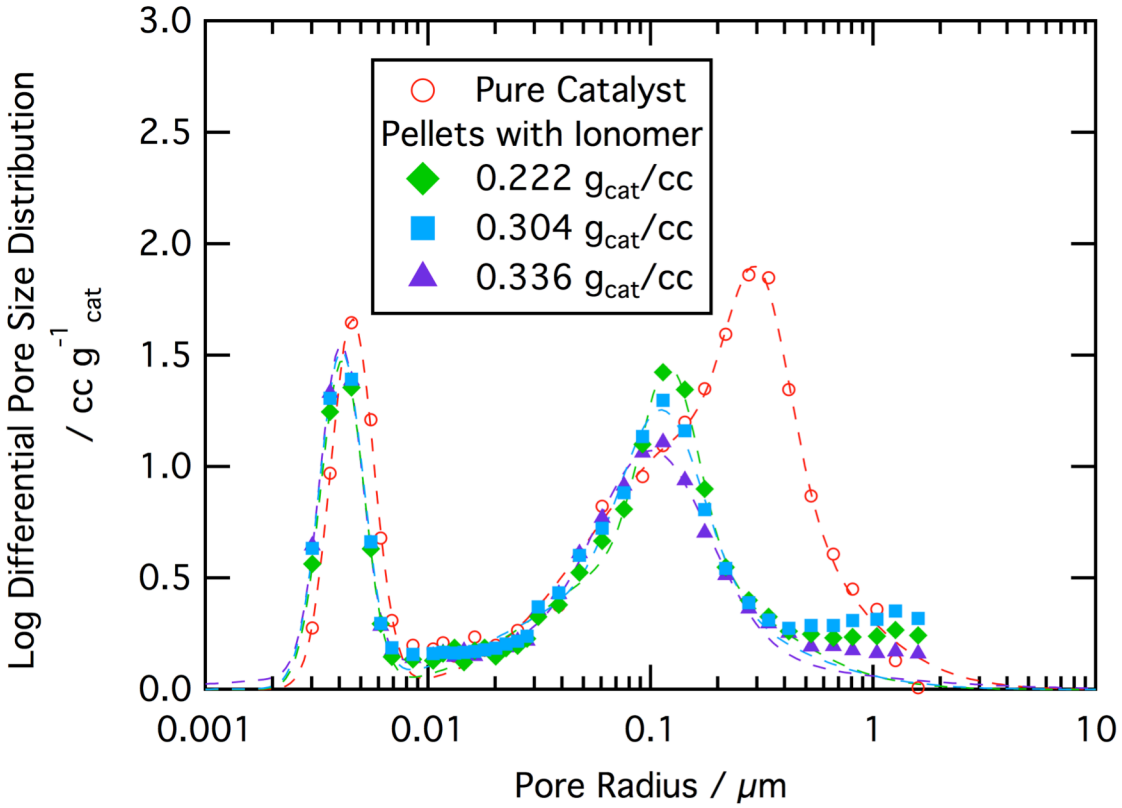

Figure 5.2: Pore size distribution of catalyst as well as three different pellets of catalyst layer material (including ionomer) as measured by mercury intrusion porosimetry with a fit composed of three lognormal pore size distributions. Fit characteristics are included in Table 5.1.

Table 5.1: Pore Size Distribution Fit Parameters

Parameter	Pore Mode	Neat Catalyst	Pellet (0.222 g_{cat}/cc)	Pellet (0.304 g_{cat}/cc)	Pellet (0.336 g_{cat}/cc)
Mean Radius /nm	1	4.57 ± 0.04	4.11 ± 0.03	4.08 ± 0.03	4.06 ± 0.02
	2	164.6 ± 8.3	98.6 ± 8.8	84.4 ± 17.5	51.9 ± 47.0
	3	307 ± 8	121.8 ± 2.4	113.3 ± 3.8	102.0 ± 3.5
Spread	1	0.222 ± 0.009	0.222 ± 0.008	0.225 ± 0.008	0.214 ± 0.007
	2	1.115 ± 0.035	1.097 ± 0.080	1.242 ± 0.140	1.943 ± 0.623
	3	0.320 ± 0.032	0.293 ± 0.026	0.416 ± 0.047	0.586 ± 0.046
Volume fraction	1	0.191 ± 0.033	0.266 ± 0.045	0.263 ± 0.093	0.261 ± 0.144
	2	0.656 ± 0.023	0.524 ± 0.033	0.451 ± 0.069	0.306 ± 0.109
	3	0.153 ± 0.022	0.210 ± 0.030	0.286 ± 0.063	0.433 ± 0.094

The various distributions are easily modeled by considering the porosity to be composed of three LNPSDs as shown in Figure 5.2. Each LNPSD, $V_k(r)$, can be represented as a function of a characteristic pore radius, r_k, spread, s_k, and fraction of total porosity, f_k:[10]

$$V_k(r) = f_k \left[\frac{1}{r s_k \sqrt{2\pi}} \exp\left(-\frac{1}{2} \frac{\ln r - \ln r_k}{s_k \sqrt{2}} \right)^2 \right] \quad [8]$$

Saturation is calculated by integrating these PSDs over the whole range for the hydrophilic pore fraction (because $p_c > 0$) and for all pores greater than the critical radius for the hydrophobic pore fraction:[10]

$$S_k = f_{HI,k} + f_{HO,k}[1 - erf(\frac{ln(r_c) - ln(r_k)}{s_k \sqrt{2}})] \quad [9]$$

where the saturation of the k^{th} LNPSD, S_k, is a function of the hydrophilic pore fraction, f_{HI}, and the hydrophobic pore fraction, f_{HO}.

Saturation impacts transport parameters via the permeability, k_L, and a reduction in effective diffusivity. In the liquid phase, an expression used by Weber et al accounts for tortuosity as well as weighting of pore sizes according to Poiseuille flow.[10,11]

$$k_L = k_{sat} \frac{S^2}{2} f_H [1 - erf(\frac{ln(r_c) - ln(r_k)}{s_k \sqrt{2}} - s_k \sqrt{2})] \quad [10]$$

In the gas phase, the governing mass balance on the various constituents is coupled with Stefan-Maxwell multicomponent diffusion: [10,21]

$$\nabla x_i = \sum_{i \neq j} \frac{N_i x_j - N_j x_i}{c D_{ij}} \quad [11]$$

where x_i represents mole fraction, N_i is the flux, c the total molar concentration, and D_{ij} a binary diffusion coefficient. The diffusion coefficient is an effective value due to the impact of porosity on the mean free path of constituents:[22,27,28]

$$D_{ij,eff} = D_{ij}^{0}(\epsilon(1-S))^{3/2} \quad [12]$$

where the bulk diffusivity, D_{ij}^{0}, is modified by the porosity (ε) and saturation (S from Eq.9). The effective diffusivity is also modified to account for Knudsen diffusion. Knudsen diffusion limits diffusivity in small pores where wall effects dominate. In order to incorporate the impact of Knudsen diffusion, a mean open pore radius is calculated. This mean open pore radius, r_K is used to calculation Knudsen diffusivity, D_K:[11,28]

$$D_{\mathrm{K}} = \frac{2r_{\mathrm{K}}}{3}\left(\frac{8RT}{\pi M}\right)^{1/2} \quad [13]$$

where R is the ideal gas constant, T is the temperature, and M is the molar mass of the gas molecule. Contributions of the two diffusion modes can be combined via the Bosanquet equation:[30-33]

$$\frac{1}{D} = \frac{1}{D_{\mathrm{K}}} + \frac{1}{D_{\mathrm{M}}} \quad [14]$$

where the diffusivity, D, is a function of Knudsen diffusivity, D_K, and molecular diffusivity, D_M.

Darcy's Law governs liquid phase transport where liquid flux is proportional to the liquid pressure gradient: [11,28]

$$N_{\mathrm{L}} = -\frac{k_{\mathrm{L}}}{\mu}\nabla P_{\mathrm{L}} \quad [15]$$

where N_L is the flux of liquid water, k_L is the effective permeability (a function of saturation, Eq. 10), μ is the viscosity of water, and ∇P_L is the liquid pressure gradient.

5.4.3 Conductive Phases

Two different conductive phases exist: solid electronic (*s*) and electrolyte (*e*) conductor. Here, Ohm's Law governs charge transport:[21]

$$i_i = -\kappa_i \nabla V_i \; ; \; i_e = -\kappa_e \nabla V_e \qquad [16]$$

where, for a given phase (i or e), the current density, i, is a function conductivity, κ, and potential, V.

Electronic conductivity was calculated from correlating high frequency resistance (HFR) with the thickness of MEAs of varying loading. This correlation, shown in Figure 5.3, assumes that ionic conductivity in the catalyst layer is much lower than electronic conductivity. Essentially, at high frequencies capacitors behave like short circuits eliminating the effect of transport and kinetic effects on the impedance. Without these effects the HFR is the ohmic resistance of the system. In the catalyst layer, the solid and electrolyte systems are in parallel making the HFR (R_{HFR}):

$$R_{\mathrm{HFR}} = R_{\mathrm{sys}} + \frac{R_{\mathrm{i}} R_{\mathrm{e}}}{R_{\mathrm{i}} + R_{\mathrm{e}}} \qquad [17]$$

where the HFR is function of the resistances of the electronic (R_e) and ionic phases (R_i) as well as the resistance of the remainder of the system (R_{sys}). When $R_i >> R_e$, the right hand side of Eq. 17 simplifies to $R_{HFR} = R_{sys} + R_e$. By comparing HFR to the electrolyte resistance calculated in the next section we can confirm this assumption that $R_i >> R_e$. The slope of the HFR with respect to catalyst layer thickness represents the electric conductivity of the catalyst layer. From this

correlation two model parameters can be found: the electronic conductivity, κ_e= 0.62 ± 0.38 S/cm and the resistance of the remainder of the system (contact resistance, etc.) R_{sys}= 0.046 ± 0.010 Ω-cm^2. While the error on the conductivity is quite large, we consider this a reasonable estimate for our purposes.

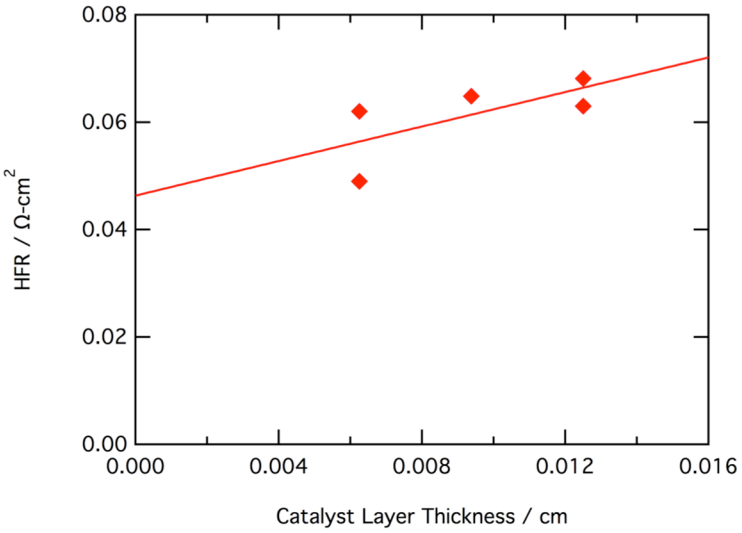

Figure 5.3: Conductivity of catalyst layer material by correlating high frequency resistance (HFR) with thickness of catalyst layers with varying loadings at constant density.

Electrolyte conductivity was calculated from electrochemical impedance spectroscopy. Makharia et al[34] and Eikerling et al[17] show that impedance of catalyst layers can be well modeled by transmission line circuits. Specifically, when the electrode potential is small and the electronic resistance in the catalyst layer is insignificant, the impedance, Z, can be modeled by the expression: [11,17,34]

$$Z = R_{\text{ext}} + \sqrt{R_{\text{i}} Z_{\text{CT}}} coth(\sqrt{R_{\text{i}}/Z_{\text{CT}}}) \quad [18]$$

where R_{ext} is the resistance external to the catalyst layer, ω is frequency, R_i is the ionic resistance in the catalyst layer, and Z_{CT} is a charge transfer impedance. This charge transfer impedance is ostensibly a Voigt element, where the impedance is a function of some charge transfer resistance, R_{CT}, and a capacitance, C_{CT}:

$$Z_{CT} = \frac{R_{CT}}{1 + j\omega R_{CT} C_{CT}} \quad [19]$$

Figure 5.4 shows impedance spectra of two loadings at two different current densities that are all well below the onset of mass transport limitations; lines represent the fit by the transmission line model, Eq. 18. From the fitted ionic resistance, R_i, conductivity for the electrolyte in the catalyst layer was calculated to be κ_i= 0.0181 ± 0.0049 S/cm. A comparison of this ionic conductivity with the electronic conductivity (κ_e= 0.62 ± 0.38 S/cm) calculated in the previous paragraph confirms the assumption that $\kappa_i << \kappa_e$ (or $R_i >> R_e$).

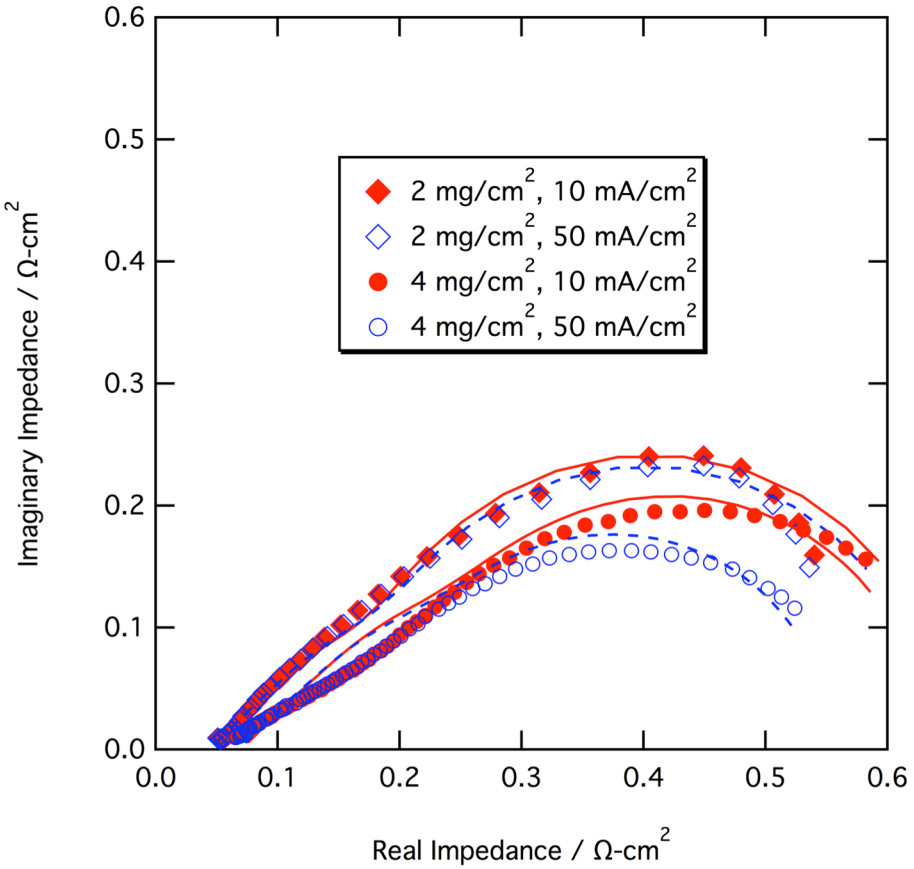

Figure 5.4: Impedance spectra of MEA with two different loadings at two different current densities. Fits shown are based on Eq. 18. Fitted parameters are shown in Table 5.2.

Table 5.2: Impedance Fit Parameters

Loading / mg cm^{-2}	Current / A cm^{-2}	Electrolyte Resistance (R_e) / Ω cm^2	Charge Transfer Resistance (R_{CT}) / Ω cm^2	Capacitance (C_{CT}) / mF cm^{-2}	External Resistance (R_{ext}) / Ω cm^2
2	0.01	0.434 ± 0.066	0.468 ± 0.029	126 ± 18	0.045 ± 0.003
2	0.05	0.466 ± 0.074	0.447 ± 0.029	131 ± 20	0.044 ± 0.003
4	0.01	0.580 ± 0.165	0.385 ± 0.046	151 ± 44	0.070 ± 0.005
4	0.05	0.544 ± 0.166	0.322 ± 0.044	153 ± 48	0.068 ± 0.005

5.4.4 Generation Terms

The generation terms for oxygen reduction and evaporation are treated as first order reaction rates. Oxygen reduction is expressed in a symmetrical Butler-Volmer form, in which the forward reaction (oxygen reduction) is first order with respect to the local partial pressure of oxygen:[28,35]

$$r_{\mathrm{ORR}} = \frac{i_{0,\mathrm{eff}}}{nF}\left[p_{\mathrm{o}}\exp\left(\frac{\alpha F\eta}{RT}\right) - \exp\left(\frac{-(1-\alpha)F\eta}{RT}\right)\right] \quad [20]$$

$$\eta = U_0 - V_0 - V_{\mathrm{i}} - V_{\mathrm{e}} \quad [21]$$

where p_{o} is the partial pressure of oxygen, η is the over-potential, and α the transfer coefficient. The over-potential, η, is a function of U_0, the reversible potential; V_0, the electrode polarization (an independent variable); V_{s}, the ionic phase potential; and V_{e}, the electronic potential. The effective pre-exponential exchange current density, $i_{0,\mathrm{eff}}$, is considered to be a function of porosity, saturation, and ionomer volume fraction due to the requirement that protons, electrons, and oxygen have access to catalytic active sites. To incorporate the impact of these phases, the exchange current density is modeled as a three-phase effective parameter:[27]

$$i_{0,\mathrm{eff}} = i_0 f_{\mathrm{i}} f_{\mathrm{s}} \epsilon (1-S) \quad [22]$$

where f_{i} is the volume fraction of ionomer and represents the probability that protons are available at any given differential volume element. The ionomer volume is calculated based on the ionomer content and density. The volume fraction of solid catalyst, f_{s}, represents the probability that a given volume element has connectivity with the electronic phase. The solid catalyst volume is calculated by subtracting porosity as measured by porosimetry and ionomer volume from the volume of the pellets used for porosimetry experiments. The porosity, ε, is calculated for a given catalyst layer specific volume by subtracting solid catalyst volume and ionomer volume. The expression ε (1-S) represents the volume fraction of oxygen-accessible open pores. In the expression above, $f_{\mathrm{s}}\varepsilon$ can also be interpreted as an area per unit volume that is dependent on the quantity of porous and solid phases. Because the total volume fractions must

equal one ($1 = f_s + f_i + \varepsilon$), an increase in one of these volume fractions necessitates a decrease in the remaining volume fraction.

The evaporation term, r_{evap}, is dependent on water vapor pressure and the partial pressure of water: [11,28]

$$r_{\mathrm{evap}} = k_{\mathrm{m}} a_{\mathrm{T}} (P_{\mathrm{vap}} - p_{\mathrm{w}}) \qquad [23]$$

where k_m is a mass-transfer coefficient, a_T the area per unit volume, P_{vap}, the vapor pressure of water, and p_w the partial pressure of water vapor. Because the reaction is fast and at equilibrium,[11,36] the rate can be thought of as the necessary evaporation necessary to keep the vapor pressure and water partial pressure equal.

5.4.5 Model Implementation

The model was written with MATLAB using the boundary value solver BVP5C. The boundary value solver generated the mesh density necessary to achieve 0.1% error for residuals above the threshold value 10^{-6}. Generally, the number of points was on the order to 20 in low-current regimes and 200 in high current regimes. A nonlinear, least-squares fitting function was used to fit the following parameters: hydrophobic pore fraction, f_{HO}; saturated liquid permeability, k_w; exchange current density, i_0; reversible potential, U; and exchange coefficient, α. The parameters were fitted simultaneously to polarization data at four different air pressures and nine potentials in the range 0.82 to 0.30 volts. Parameters were fit to a tolerance of 0.1%. The current density was calculated as the electronic current at the channel.

Sensitivity was calculated by running the model at a fixed step size of 1% for a given parameter. The change in current density, Δi, due to a change, Δx, in the value of a parameter x, leads to the sensitivity, B_x:

$$B_x = \frac{\Delta i/i}{\Delta x/x} \qquad [24]$$

A positive sensitivity indicates a correlation between current and the parameter of interest, whereas a negative value indicates anti-correlation. No correlation is indicated by a sensitivity of zero. The model was non-dimensionalized as shown in Appendix A.

5.5. Results and Discussion

The model was used to fit MEA data obtained at three different backpressures: 2, 12, and 30 psi_g. These pressures correspond to partial air pressures: 0.5, 1.2, and 2.4 atm respectively correcting for altitude in Albuquerque, NM (P_{atm}=0.83 bar)[37] and experimental conditions. Catalyst loadings of 2, 3, and 4 mg/cm^2 were studied. Five parameters were fit: hydrophobic pore fraction, f_{HO}; saturated liquid permeability, k_w; exchange current density, i_0; reversible potential, U_0 and transfer coefficient, α. The fitted parameters are shown in Table III, while the remaining parameters are shown in Table IV at the end of the chapter.

A plot of experimental polarization curves along with the fitted model is shown in Figure 5.5. From observation, the model fits the data well with regards to the shape of the curves. The model fit shown in Figure 5.5 can be further validated by comparing fitted values with expected values. The exchange coefficient, α is 0.407 ± 0.009 which is in the range of typical values (0.3-0.7).[35] The exchange current density is large because it represents a theoretical value if all points in the electrode where on a triple-phase boundary. This is not possible for materials of finite thickness, so it is best to consider the effective exchange coefficient (Eq. 22) for comparison purposes. The effective exchange current densities are 28, 42, and 56 mA/cm^2 at 30 psi for 2, 3, and 4 mg/cm^2 loadings respectively. These numbers correspond well with the currents at which the

experimental polarization curves deviate from the Tafel regime in the upper part of Figure 5.5. At some point, when the active site for these catalysts is better understood, i_0 should be revisited to account for turnover rate and adsorption effects. The fitted permeability of $(5.27 \pm 2.58)\times10^{-13}$ agrees well with the value predicted by the Kozeny-Carmen Equation (4×10^{-13}).[12] The hydrophobic pore fraction was found to be 0.287 ± 0.110. Based on the assumption that all hydrophobicity is due to the ionomer, this number can be compared to the electrolyte solid fraction in the catalyst layer, 0.193 ± 0.070. The agreement between these values corroborates the theory that the majority of the hydrophobicity is due to the ionomer.

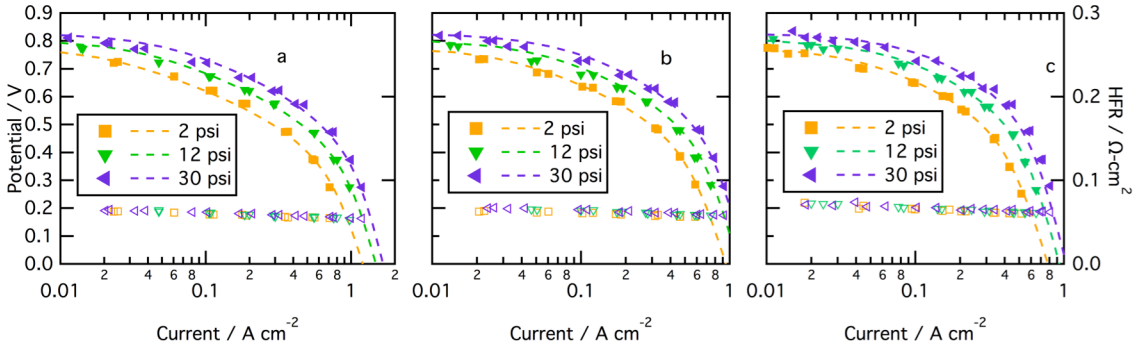

Figure 5.5: Comparison of experimental and model results at three different gas pressures for (a) 2 mg/cm^2, (b) 3 mg/cm^2, and (c) 4 mg/cm^2. Conditions: Temp. 80 C, 25BC GDL, 4mg/cm^2 Catalyst Loading, 45 wt.% Nafion, Cell Area: 5cm^2, membrane: NR211.

Table 5.3: Fitted Parameters

Parameter	Values	Units
Transfer Coefficient	0.416 ± 0.010	
Exchange current density (i_0)	1300 ± 512	A / bar cm^3
Reversible potential (U_0)	0.853 ± 0.005	V
CL Hydrophobic pore fraction (f_{HO})	0.287 ± 0.110	
Saturated Liquid Permeability (k_w)	$(5.03\pm 2.41)\times10^{-13}$	cm^2

Now that the fit has been established, profiles in the catalyst layer can be used to better understand transport phenomena. Figure 5.6 shows electronic current profiles (a), oxygen vapor fraction profiles (b), and flooding (c) in the catalyst layer at three different potentials. How these

potentials correspond to the polarization curve is shown in Figure 5.6d: points I, II, and III correspond to potentials in the kinetically limited regime, ohmic limited regime, and catalyst layer oxygen transport limited regime respectively. The first point shows a linear current profile as shown in Figure 5.6a, which is typical of kinetically-limited ORR in the absence of concentration gradients. Point II shows an ohmically-limited current profile, in which ohmic resistance in the catalyst layer electrolyte cause most of the ORR to occur near the membrane-CL interface, where a steep current gradient is observed. Continuing to lower potentials, in Figure 5.6b, point III shows conditions where the catalyst layer closest to the membrane has been completely exhausted of oxygen. Oxygen depletion makes those sections inert, and the current profile is flat and zero as shown in Figure 5.6a between 0 and 0.1. The limiting case (not shown) is where the catalyst layer is almost entirely oxygen starved and all the ORR occurs at the CL-GDL interface. At this extreme, the polarization becomes linear due to the ionic resistance of the catalyst layer.

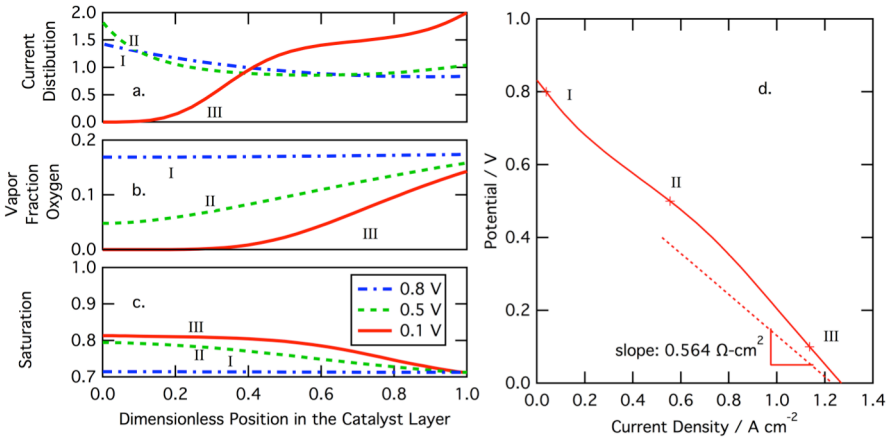

Figure 5.6: (a) Solid phase current distribution, (b) ionic over-potential, and (c) flooding at dimensionless positions in the catalyst layer at three different potentials on the polarization curve (d) showing I, kinetic limitations; II, electrolyte conductivity limitations; and III, oxygen diffusion limitations. For position in the catalyst layer, zero represents the membrane interface and one represents GDL interface.

A sensitivity study of performance in air is shown in Figure 5.7. Sensitivity is defined as a ratio of relative change in performance (current) to relative change in a given parameter. Figure 5.7 shows sensitivity as it varies with potential (on the *y*-axis). At all potentials hydrophobic pore volume shows high sensitivity, this indicates that flooding is high. Essentially, flooding limits electrochemically active surface area at high potentials (kinetically limited, I) and limits oxygen diffusion at low potentials (oxygen transport limited, III). Around 0.6 V there is a dip in the hydrophobic pore fraction sensitivity. This dip correlates to an increase in electrolyte conductivity sensitivity. This confirms the ohmic limited regions identified by point II in Figure 5.6. The significant anti-correlation is loading: at high potentials increased loading means increased electrochemically active surface area, but at low potentials this increased loading only inhibits oxygen diffusion, leading to lowered utilization and reduced performance.

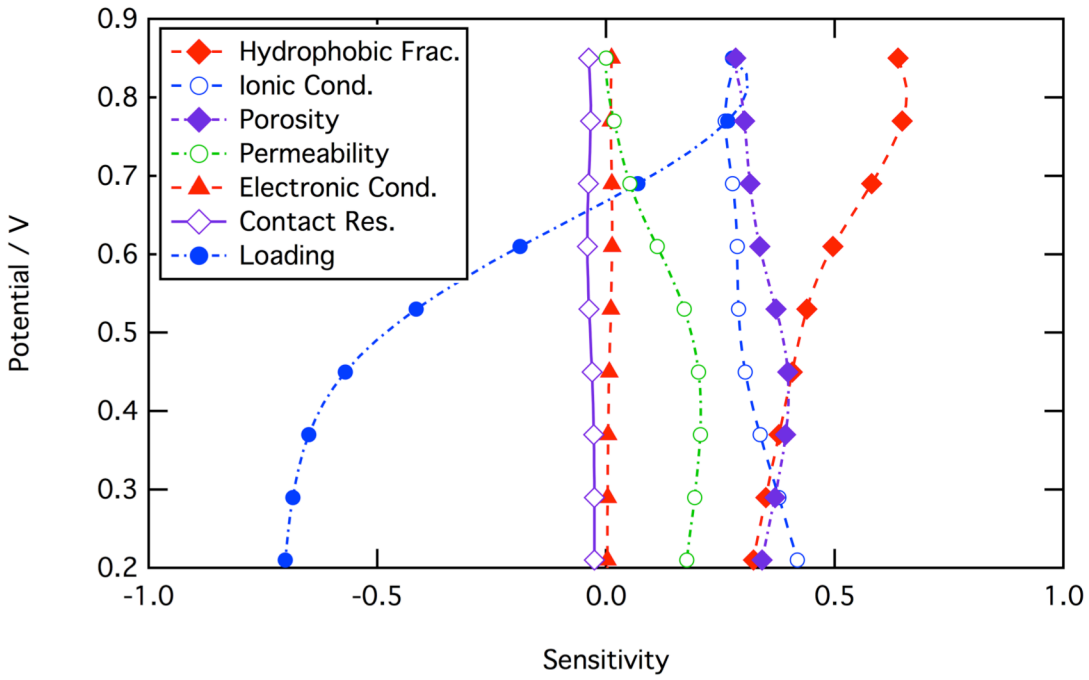

Figure 5.7: Plot of current sensitivity in air varying with potential.

A sensitivity study can also be calculated for oxygen, as shown in Figure 5.8. The sensitivity in oxygen is similar to air at high potentials, but not at low potentials. The similarity in sensitivity is expected at high potentials due to kinetic limitation. Once outside of this regime, the similarities decrease substantially due to the lack of transport limitations in oxygen. In this ohmically-limited regime flooding only impacts electrochemically active surface area causing the hydrophobic pore fraction sensitivity to decrease as kinetics become less limiting at lower potentials. In oxygen, electron transport limits current density at low potentials. This is shown by the increase in ionic conductivity sensitivity around 0.8 V. At low potentials activity reaches a mixed domination region. In this region performance is equally controlled by hydrophobic porosity, ionic conductivity, and kinetic parameters. Essentially the current profile is similar to point II in Figure 5.6a, but as the potential decreases further the current distribution becomes increasingly concentrated at the CL-membrane interface due to ionic conductivity limitations. As the current distribution becomes more concentrated at that interface, less charge is conducted through the catalyst layer electrolyte, which decreases the ionic conductivity sensitivity. External ohmic losses also become more significant at low potentials. This value is not a fitted parameter, but it does include contact resistance between the CL and GDL due to the high Nafion content in the CL. For this reason, external resistance was added to the oxygen sensitivity study (purple line with open diamonds) and represents the impact of contact resistance between assembly layers.

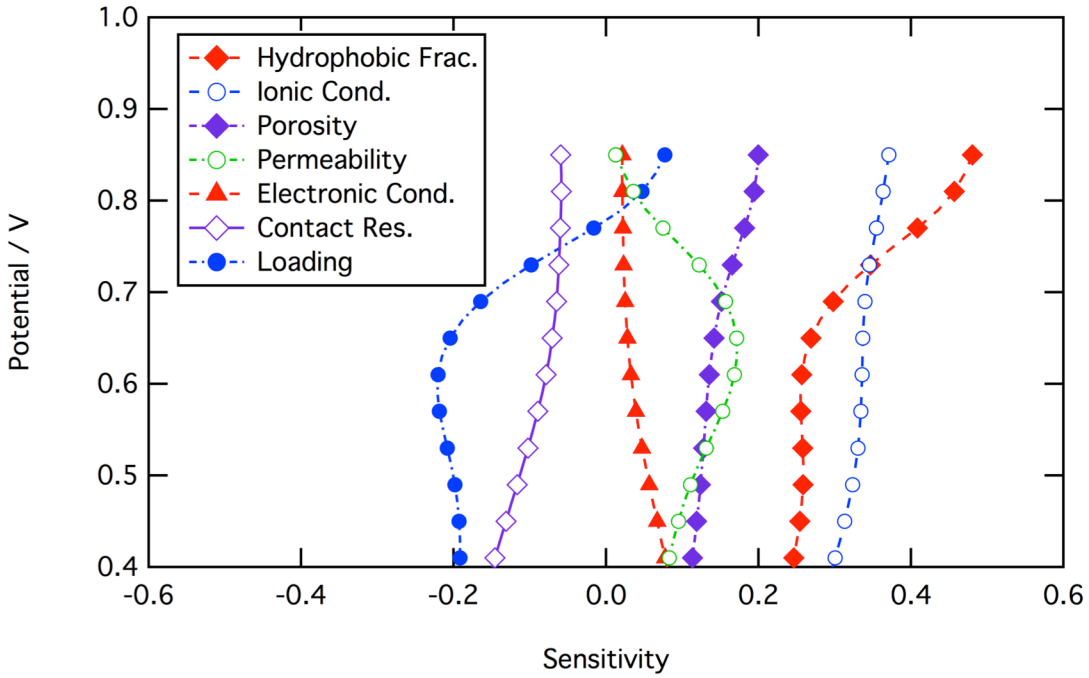

Figure 5.8: Plot of current sensitivity in oxygen varying with potential.

To return to air sensitivity, two recommendations can be made for future non-PGM catalysts and their application in fuel cells. Loading should be optimized with current density at key operating potentials in mind. For applications running at max power, lower loadings are desired to increase performance in the 0.6-0.4 V range. A second observation that can be gleaned from the air sensitivity is that increasing ionomer content near the CL-membrane interface could mitigate ohmic losses resulting from poor catalyst utilization at low potentials, as previously observed by other workers for platinum based catalyst layers.[38,39] This would be the result of optimizing catalyst ink for different depths in the catalyst layer, and the catalyst layer close to the GDL would be optimized for oxygen diffusion, while the catalyst layer close to the membrane would be optimized for electrolyte conductivity.

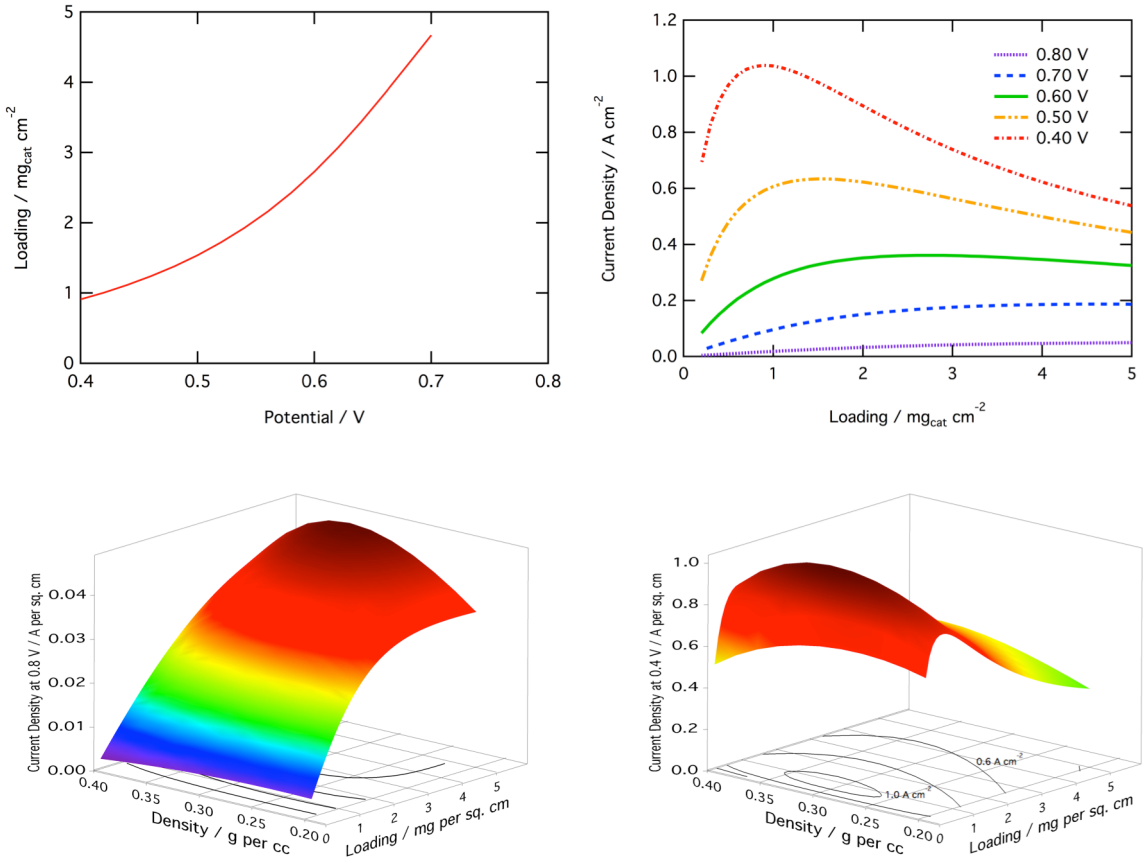

Figure 5.9: (a) Optimal loading as it varies with potential, (b) current as it varies with loading at various potentials, (c) current as it varies with density and loading at 0.8 V, and (d) current as it varies with density and loading at 0.4 V. Conditions: 30 psi, Temp. 80 C, 25BC GDL, 45 wt.% Nafion, Cell Area: 5cm^2, membrane: NR211.

Finally, optimization studies were conducted for loading and catalyst layer density. For each parameter, the value was obtained that provided maximum current density with all other parameters at baseline values (Table 3 and 4). From Figure 5.9a, it is apparent that optimal loading changes with potential, because mass transport limitations are more significant at low potential and kinetic limitations more significant at high potential. CL density represents how compressed the catalyst layer is during MEA construction and the optimal value does not vary much with potential as shown in contour plots Figure 5.9c and 5.9d.

5.6. Conclusions

A one-dimensional, steady-state model was developed for electrode-scale transport in a non-PGM PEMFC cathode. It was found that flooding limits oxygen transport in air due to reduced effective porosity and active surface area. At low potentials the flooding limitations result in poor catalyst utilization and increased ohmic losses. In contrast to air performance, oxygen performance depends primarily on active surface area and electron conductivity. The difference in sensitivity between air and oxygen performance suggests that oxygen MEA performance is not an effective indicator for non-PGM catalysts.

Finally, cathodes can be designed for improved air performance by improving catalyst utilization. Utilization can be improved in two different ways. Most simply, utilization can be increase by decreasing loading. Although this model predicts improved performance with decreased loading, it is important to note that as catalyst thickness decreases, the relative importance of interfacial effects between CL and GDL will increase. Utilization can also be improved by optimizing sections of the catalyst layer for different phenomena. Optimization would include improving gas diffusion near the GDL and improving ionic conductivity near the membrane.

5.7. Acknowledgments

We gratefully acknowledge the partial financial support from the U.S. Department of Energy (EERE), under a Non PGM Catalyst development effort (Contract no EE 0000459, lead by Northeastern University, Sanjeev Mukerjee, P.I.).

Table 5.4: Model Parameters

Parameter	Values	Units	Notes
Diffusion coefficient of oxygen in water (pD_{ow}) [40]	$0.3022\times (T/323.83)^{2.334}$	bar cm^2 / s	Literature Value[11, 33, 34]
Diffusion coefficient of oxygen in nitrogen (pD_{on}) [40]	$0.0544\times (T/143.01)^{1.823}$	bar cm^2 / s	Literature Value[11,40,41]
Diffusion coefficient of water in nitrogen (pD_{wn}) [40]	$0.2599\times (T/299.42)^{2.334}$	bar cm^2 / s	Literature Value[11,40,41]
Evaporation rate ($k_m a_T$) [11]	100	mol / bar s cm^3	Literature Value[11,36]
Viscosity (μ) [11]	$(2695.3\text{-}6.6\ T)\times 10^{-11}$	bar s	Literature Value[11]
Water surface tension (γ) [11]	$0.12398\text{-}0.00017393\times T$	N / m	Literature Value[11]
CL electronic conductivity (κ_e)	0.62 ± 0.38	S/cm	Correlated from HFR
CL ionic conductivity (κ_i)	0.0158 ± 0.0020	S/cm	Calculated from impedance model
Catalyst density	0.32	g_{cat}/cc	Measured
CL Hydrophobic Contact Angle (θ_{obs})	90.02	Degrees	Literature Value[11]
Saturated Permeability (k_{sat})[12]	1×10^{-9}	cm^2	Literature Value[11]
External Resistance (R_{ext})	0.046 ± 0.010	Ω cm^2	Calculated from High Frequency Impedance
Electro-osmotic coefficient	$0.5\times P_{vap}/(P_g\text{-}P_{vap})$		Literature[26]

APPENDIX

Appendix A Non-Dimensional Cathode Model

This section describes the non-dimensional equations for a multi-phase, transport model of a catalyst layer (CL). This one-dimensional, steady-state model consists of four phases: an electron-conducting solid phase, an ion-conducting ionic phase, and non-conducting liquid and gas phases. The primary dependent variables in these phases are solid phase potential, V_s, electrolyte phase potential, V_e, liquid pressure, P_L; and vapor fractions of oxygen and water vapor, x_o and x_w. Currents and species flux are also dependent variables, but can all be related to gradients of primary dependent variables. A more complete discussion of the model is available in Chapter 5 of this dissertation.

The governing equations consider the conservation of electrons, protons, liquid water, and water vapor (Equations 2, 3, 4, and 5 respectively):

$$0 = -\kappa_s \nabla^2 V_s + nF r_{ORR} \quad [25]$$

$$0 = -\kappa_e \nabla^2 V_e - nF r_{ORR} \quad [26]$$

$$0 = -\frac{k_L}{\mu} \nabla^2 P_L + 2 r_{ORR} - r_{evap} \quad [27]$$

$$\nabla N_w = r_{evap} \quad [28]$$

where κ_s is solid conductivity, V_s is solid phase potential, n is electrons per mole oxygen, F is Faraday's constant, r_{ORR} is an oxygen reduction reaction rate, κ_e is electrolyte conductivity, V_e is

electrolyte potential, k_L is liquid permeability (a function of saturation), μ is viscosity, P_L is liquid pressure, r_{evap} is an evaporation rate, and N_w is flux of water vapor. Flux of nitrogen in air is set to zero everywhere, because it does not participate in any reaction, and the membrane is considered to be gas-impermeable.

Non-dimentionalization was based on the gas phase because understanding oxygen transport is a key goal for this project. In the gas phase, the governing mass balance on the various constituents is coupled with Stefan-Maxwell multicomponent diffusion: [11,22]

$$\nabla x_i = RT \sum_{i \neq j} \frac{N_i x_j - N_j x_i}{p D_{ij}} \quad [29]$$

where x_i represents mole fraction, N_i is the flux, c the total molar concentration, and D_{ij} a binary diffusion coefficient. This equation is non-dimensionalized by multiplying through with a length scale and results in:

$$\nabla x_i = \sum_{i \neq j} Q_{ij} x_j - Q_{ji} x_i \quad [30]$$

$$Q_{ij} = \frac{RT N_i L}{p D_{ij}} \quad [31]$$

where Q is a dimensionless flus. Although it would be fine to leave the equations in this system, it is better keep a consistent frame of reference for the various fluxes. This is accomplished using oxygen in dry air as a reference system and results in:

$$\nabla x_i = \sum_{i \neq j} \Pi_{ij} (Q_i x_j - Q_j x_i) \quad [32]$$

$$\Pi_{ij} = \frac{pD_{on}}{pD_{ij}} \quad [33]$$

where Π_{ij} is a dimensionless flux resistance of constituent *i* in *j*, and Q is a dimensionless flux that can be related to the dimensional flux:

$$N_i = Q_0 Q_i \quad [34]$$

$$Q_0 = \frac{pD_{on}}{RTL} \quad [35]$$

where Q_0 is the reference flux resulting from the non-dimensionalization. The above analysis has an analogy across all phases and results in all fluxes having similar magnitudes, which improves performance of the boundary value solver.

Darcy's Law can be similarly non-dimensionalized. This equation governs liquid phase transport where liquid flux is proportional to the liquid pressure gradient: [12,28]

$$N_{\mathrm{L}} = -\frac{k_{\mathrm{L}}}{\mu} \nabla P_{\mathrm{L}} \quad [36]$$

where N_{L} is the flux of liquid water, k_{L} is the effective permeability (a function of saturation, Eq. 9 in Chapter 5), μ is the viscosity of water, and ∇P_{L} is the liquid pressure gradient. This can be non-dimensionalized by a *Q*-flux:

$$Q_{\mathrm{L}} = -\nabla \Psi_{\mathrm{L}} / \Pi_{\mathrm{L}} \quad [37]$$

$$\Pi_{\mathrm{L}} = \frac{\mu_{\mathrm{L}} pD_{on}}{RTk_{\mathrm{L}} P} \quad [38]$$

where Π_{L} is a dimensionless liquid flux resistance and Ψ_{L} is a dimensionless liquid pressure.

Two different conductive phases exist: solid electronic (*s*) and electrolyte (*e*) conductor. Here, Ohm's Law governs charge transport:[22]

$$i_i = -\kappa_i \nabla V_i \; ; \; i_e = -\kappa_e \nabla V_e \qquad [39]$$

where, for a given phase (i or e), the current density, i, is a function conductivity, κ, and potential, V. In order non-dimensionalize these phases, an analogy can be drawn between the pressure/liquid-flux system of the previous section of the potential/current system. The current can be thought of as a molar flux, and the potential is non-dimensionalized by the Tafel slope:

$$Q_e = -\nabla \Psi_e / \Pi_e \qquad [40]$$

$$\Pi_e = \frac{pD_{on}n}{\kappa_e} \qquad [41]$$

where Ψ_e is a dimensionless electronic potential (V_eF/RT) and Π_e is a dimensionless electronic resistance that is a function of electrons per mole oxygen, n, and the electronic conductivity, κ_e. Q_e can be thought of a dimensionless molar flux of oxygen or a current density:

$$N_o = \frac{i_e}{nF} = Q_0 Q_o = Q_0 Q_e \qquad [42]$$

now that the transport equations have been dimensionalized the generation terms will be considered.

The generation terms for oxygen reduction and evaporation are treated as first order reaction rates. Oxygen reduction is expressed in a symmetrical Butler-Volmer form, in which the forward reaction (oxygen reduction) is first order with respect to the local partial pressure of oxygen:[28,31]

$$r_{\mathrm{ORR}} = \frac{i_{0,\mathrm{eff}}}{nF}\left[p_{\mathrm{o}}\exp\left(\frac{\alpha F\eta}{RT}\right) - p_{\mathrm{ref}}\exp\left(\frac{-(1-\alpha)F\eta}{RT}\right)\right] \quad [43]$$

$$\eta = U_0 - V_0 - V_{\mathrm{s}} - V_{\mathrm{e}} \quad [44]$$

where p_{o} is the partial pressure of oxygen, p_{ref} is a reference pressure chosen to be 1 atm because the reverse reaction does not contain constituents in the gas phase, η is the over-potential, and α the transfer coefficient. The over-potential, η, is a function of U_0, the reversible potential; V_0, the electrode polarization (an independent variable); V_{s}, the solid phase potential; and V_{e}, the electrolyte potential. This equation is non-dimensionalized based on a local mass balance of oxygen:

$$\nabla N_o = r_{\mathrm{ORR}} = \frac{i_{0,\mathrm{eff}}}{nF}\left[p_{\mathrm{o}}\exp\left(\frac{\alpha F\eta}{RT}\right) - p_{\mathrm{ref}}\exp\left(\frac{-(1-\alpha)F\eta}{RT}\right)\right] \quad [45]$$

by substituting for a dimensionless oxygen flux, and normalizing our length scale the equation can be put in terms of a reduced Thiele modulus:

$$\nabla Q_o = \Phi_{Th}^2\left[x_{\mathrm{o}}\exp\left(\alpha\Psi\right) - x_{\mathrm{ref}}\exp\left(-(1-\alpha)\Psi\right)\right] \quad [46]$$

$$\Phi_{Th}^2 = \frac{Pi_{o,eff}}{nF}\frac{RTL^2}{pD_{o,n}} \quad [47]$$

$$\Psi = \Psi_0 - \Psi_{\mathrm{e}} - \Psi_{\mathrm{i}} \quad [48]$$

where Φ_{Th} is a Thiele modulus for oxygen reduction, and Ψ is a dimensionless overpotential that takes into account electrode polarization (Ψ_0) and ohmic losses due to electronic (Ψ_{e}) and ionic (Ψ_{i}) conductivities.

The evaporation term, r_{evap}, is dependent on water vapor pressure and the partial pressure of water: [12,28]

$$r_{\mathrm{evap}} = k_{\mathrm{m}} a_{\mathrm{T}} (P_{\mathrm{vap}} - p_{\mathrm{w}}) \quad [49]$$

where k_m is a mass-transfer coefficient, a_T the area per unit volume, P_{vap}, the vapor pressure of water, and p_w the partial pressure of water vapor. Because the reaction is fast and at equilibrium,[12,32] the rate can be thought of as the necessary evaporation necessary to keep the vapor pressure and water partial pressure equal. This equation is similarly non-dimensionalized based on a local mass balance of water vapor:

$$\frac{dN_{g,w}}{dx} = r_{evap}|_x \quad [50]$$

by substituting for a dimensionless oxygen flux, and normalizing our length scale the equation can be put in terms of a reduced Thiele modulus:

$$\frac{dQ_w}{d\xi} = \Phi_{evap}^2 (P_{vap}/P_g - x_w) \quad [51]$$

$$\Phi_{evap}^2 = \frac{k_m a_T RTLP_g}{pD_{o,n}} \quad [52]$$

where Π_L is a dimensionless liquid flux resistance and Ψ_L is a dimensionless liquid. Files associated with the model have been published on gitlab.msu.edu:

https://gitlab.msu.edu/leona148/CathodeModel

REFERENCES

REFERENCES

1. M. H. Robson, A. Serov, K. Artyushkova and P. Atanassov, "A Mechanistic Study of 4-Aminoantipyrine and Iron Derived Non-Platinum Group Metal Catalyst on the Oxygen Reduction Reaction," *Electrochimica Acta* (2012).

2. R. Bashyam and P. Zelenay, "A class of non-precious metal composite catalysts for fuel cells," *Nature,* **443**(7107), 63-66 (2006). doi:10.1038/nature05118

3. H. T. Chung, C. M. Johnston, K. Artyushkova, M. Ferrandon, D. J. Myers and P. Zelenay, "Cyanamide-derived non-precious metal catalyst for oxygen reduction," *Electrochemistry Communications,* **12**(12), 1792-1795 (2010). doi:10.1016/j.elecom.2010.10.027

4. F. Jaouen, E. Proietti, M. Lefèvre, R. Chenitz, J.-P. Dodelet, G. Wu, H. T. Chung, C. M. Johnston and P. Zelenay, "Recent advances in non-precious metal catalysis for oxygen-reduction reaction in polymer electrolyte fuel cells," *Energy & Environmental Science,* **4**(1), 114 (2011). doi:10.1039/c0ee00011f

5. F. Jaouen, J. Herranz, M. Lefevre, J.-P. Dodelet, U. I. Kramm, I. Herrmann, P. Bogdanoff, J. Maruyama, T. Nagaoka, A. Garsuch, J. R. Dahn, T. Olson, S. Pylypenko, P. Atanassov and E. A. Ustinov, "Cross-Laboratory Experimental Study of Non-Noble-Metal Electrocatalysts for the Oxygen Reduction Reaction," *ACS Applied Materials & Interfaces,* **1**(8), 1623-1639 (2009). doi:10.1021/am900219g

6. N. Leonard, V. Nallathambi and S. C. Barton, "Carbon Supports for Non-Precious Metal Oxygen Reducing Catalysts," *Journal of the Electrochemical Society,* **160**(8), F788-F792 (2013). doi:10.1149/2.026308jes

7. V. Nallathambi, N. Leonard, R. Kothandaraman and S. C. Barton, "Nitrogen Precursor Effects in Iron-Nitrogen-Carbon Oxygen Reduction Catalysts," *Electrochemical and Solid-State Letters,* **14**(6), B55-B58 (2011). doi:Doi 10.1149/1.3566065

8. H. A. Gasteiger, S. S. Kocha, B. Sompalli and F. T. Wagner, "Activity benchmarks and requirements for Pt, Pt-alloy, and non-Pt oxygen reduction catalysts for PEMFCs," *Applied Catalysis B: Environmental,* **56**(1-2), 9 (2005).

9. T. E. Springer, T. A. Zawodzinski and S. Gottesfeld, "Polymer Electrolyte Fuel-Cell Model," *Journal of the Electrochemical Society,* **138**(8), 2334-2342 (1991). doi:Doi 10.1149/1.2085971

10. A. Z. Weber and J. Newman, "Modeling transport in polymer-electrolyte fuel cells," *Chem Rev,* **104**(10), 4679-726 (2004).

11. A. Z. Weber and J. Newman, "Modeling Transport in Polymer-Electrolyte Fuel Cells," *Chemical Reviews,* **104**(10), 4679-4726 (2004).

12. U. R. Salomov, E. Chiavazzo and P. Asinari, "Pore-scale modeling of fluid flow through gas diffusion and catalyst layers for high temperature proton exchange membrane (HT-PEM) fuel cells," *Computers & Mathematics with Applications,* **67**(2), 393-411 (2014). doi:Doi 10.1016/J.Camwa.2013.08.006

13. J. T. Gostick, M. W. Fowler, M. A. Ioannidis, M. D. Pritzker, Y. M. Volfkovich and A. Sakars, "Capillary pressure and hydrophilic porosity in gas diffusion layers for polymer electrolyte fuel cells," *Journal of Power Sources,* **156**(2), 375-387 (2006). doi:Doi 10.1016/J.Jpowsour.2005.05.086

14. J. T. Gostick, M. A. Ioannidis, M. W. Fowler and M. D. Pritzker, "Pore network modeling of fibrous gas diffusion layers for polymer electrolyte membrane fuel cells," *Journal of Power Sources,* **173**(1), 277-290 (2007). doi:Doi 10.1016/J.Jpowsour.2007.04.059

15. Q. Ye and T. Van Nguyen, "Three-dimensional simulation of liquid water distribution in a PEMFC with experimentally measured capillary functions," *Journal of the Electrochemical Society,* **154**(12), B1242-B1251 (2007). doi:10.1149/1.2783775

16. A. Z. Weber, "Macroscopic Modeling of the Proton-Exchange-Membrane Fuel-Cell Catalyst Layer," *ECS Transactions,* **45**(2), 71-83 (2012).

17. M. Eikerling and A. A. Kornyshev, "Electrochemical impedance of the cathode catalyst layer in polymer electrolyte fuel cells," *Journal of Electroanalytical Chemistry,* **475**(2), 107-123 (1999). doi:Doi 10.1016/S0022-0728(99)00335-6

18. J. Liu and M. Eikerling, "Model of cathode catalyst layers for polymer electrolyte fuel cells: The role of porous structure and water accumulation," *Electrochimica Acta,* **53**(13), 4435-4446 (2008). doi:Doi 10.1016/J.Electacta.2008.01.033

19. M. Eikerling and A. A. Kornyshev, "Modelling the performance of the cathode catalyst layer of polymer electrolyte fuel cells," *Journal of Electroanalytical Chemistry,* **453**(1-2), 89-106 (1998). doi:Doi 10.1016/S0022-0728(98)00214-9

20. M. Eikerling, "Water management in cathode catalyst layers of PEM fuel cells - A structure-based model," *Journal of the Electrochemical Society,* **153**(3), E58-E70 (2006). doi:Doi 10.1149/1.2160435

21. W. Yoon and A. Z. Weber, "Modeling Low-Platinum-Loading Effects in Fuel-Cell Catalyst Layers," *Journal of The Electrochemical Society,* **158**(8), B1007-B1018 (2011). doi:10.1149/1.3597644

22. M. El Hannach, J. Pauchet and M. Prat, "Pore network modeling: Application to multiphase transport inside the cathode catalyst layer of proton exchange membrane fuel cell," *Electrochimica Acta,* **56**(28), 10796-10808 (2011). doi:10.1016/j.electacta.2011.05.060

23. A. Serov, K. Artyushkova and P. Atanassov, "Fe-N-C Oxygen Reduction Fuel Cell Catalyst Derived from Carbendazim: Synthesis, Structure, and Reactivity," *Advanced Energy Materials,* **4**(10), n/a-n/a (2014). doi:10.1002/aenm.201301735

24. A. W. Adamson and A. P. Gast, *Physical chemistry of surfaces,* vol. (Wiley, New York, 1997).

25. A. Z. Weber and J. Newman, "Transport in Polymer-Electrolyte Membranes: III. Model Validation in a Simple Fuel-Cell Model," *Journal of The Electrochemical Society,* **151**(2), A326-A339 (2004). doi:10.1149/1.1639158

26. G. J. M. Janssen, "A Phenomenological Model of Water Transport in a Proton Exchange Membrane Fuel Cell," *Journal of The Electrochemical Society,* **148**(12), A1313-A1323 (2001). doi:10.1149/1.1415031

27. P. K. Das, X. G. Li and Z. S. Liu, "Effective transport coefficients in PEM fuel cell catalyst and gas diffusion layers: Beyond Bruggeman approximation," *Applied Energy,* **87**(9), 2785-2796 (2010). doi:Doi 10.1016/J.Apenergy.2009.05.006

28. A. Z. Weber, R. L. Borup, R. M. Darling, P. K. Das, T. J. Dursch, W. Gu, D. Harvey, A. Kusoglu, S. Litster, M. M. Mench, R. Mukundan, J. P. Owejan, J. G. Pharoah, M. Secanell and I. V. Zenyuk, "A Critical Review of Modeling Transport Phenomena in Polymer-Electrolyte Fuel Cells," *Journal of The Electrochemical Society,* **161**(12), F1254-F1299 (2014). doi:10.1149/2.0751412jes

29. M. Uchida, Y. Fukuoka, Y. Sugawara, N. Eda and A. Ohta, "Effects of microstructure of carbon support in the catalyst layer on the performance of polymer-electrolyte fuel cells," *Journal of the Electrochemical Society,* **143**(7), 2245-2252 (1996). doi:Doi 10.1149/1.1836988

30. W. G. Pollard and R. D. Present, "On Gaseous Self-Diffusion in Long Capillary Tubes," *Physical Review,* **73**(7), 762-774 (1948). doi:Doi 10.1103/Physrev.73.762

31. J. Becker, C. Wieser, S. Fell and K. Steiner, "A multi-scale approach to material modeling of fuel cell diffusion media," *International Journal of Heat and Mass Transfer,* **54**(7-8), 1360-1368 (2011). doi:Doi 10.1016/J.Ijheatmasstransfer.2010.12.003

32. T. Hutzenlaub, J. Becker, R. Zengerle and S. Thiele, "Modelling the water distribution within a hydrophilic and hydrophobic 3D reconstructed cathode catalyst layer of a proton exchange membrane fuel cell," *Journal of Power Sources,* **227**(0), 260-266 (2013). doi:10.1016/j.jpowsour.2012.11.065

33. S. Litster, W. K. Epting, E. A. Wargo, S. R. Kalidindi and E. C. Kumbur, "Morphological Analyses of Polymer Electrolyte Fuel Cell Electrodes with Nano-Scale Computed Tomography Imaging," *Fuel Cells,* **13**(5), 935-945 (2013). doi:10.1002/fuce.201300008

34. R. Makharia, M. F. Mathias and D. R. Baker, "Measurement of catalyst layer electrolyte resistance in PEFCs using electrochemical impedance spectroscopy," *Journal of the Electrochemical Society,* **152**(5), A970-A977 (2005).

35. A. J. Bard and L. R. Faulkner, *Electrochemical methods : fundamentals and applications,* vol. (John Wiley, New York, 2001).

36. J. H. Nam and M. Kaviany, "Effective diffusivity and water-saturation distribution in single- and two-layer PEMFC diffusion medium," *International Journal of Heat and Mass Transfer,* **46**(24), 4595-4611 (2003). doi:10.1016/S0017-9310(03)00305-3

37. M. L. Salby, *International Geophysics, Volume 61 : Fundamentals of Atmospheric Physics,* vol. (Academic Press, Burlington, MA, USA, 1996).

38. Z. Xie, T. Navessin, K. Shi, R. Chow, Q. Wang, D. Song, B. Andreaus, M. Eikerling, Z. Liu and S. Holdcroft, "Functionally Graded Cathode Catalyst Layers for Polymer Electrolyte Fuel Cells: II. Experimental Study of the Effect of Nafion Distribution," *Journal of The Electrochemical Society,* **152**(6), A1171-A1179 (2005). doi:10.1149/1.1904990

39. D. Song, Q. Wang, Z. Liu, M. Eikerling, Z. Xie, T. Navessin and S. Holdcroft, "A method for optimizing distributions of Nafion and Pt in cathode catalyst layers of PEM fuel cells," *Electrochimica Acta,* **50**(16–17), 3347-3358 (2005). doi:10.1016/j.electacta.2004.12.008

40. R. B. Bird, W. E. Stewart and E. N. Lightfoot, *Transport phenomena,* vol. (J. Wiley, New York, 2007).

41. T. R. Marrero and E. A. Mason, "Gaseous diffusion coefficients," *J. Phys. Chem. Ref. Data,* **1**(1), 3-118 (1972).

Chapter 6 Summary of Research Contributions

This dissertation improves performance and understanding of non-precious metal catalysts (NPMCs) for proton exchange membrane fuel cells. Chapter 2 is an important optimization of carbon supports for the autogenic pressure metal-nitrogen-carbon catalyst, while Chapters 3 and 4 increase understanding of this catalyst. Chapter 4 also introduces a new method of analyzing NPMCs. Chapter 5 both increases understanding of NPMC behavior in fuel cells and provides specific guidance for Pajarito Powder in how best to use their catalyst. This guidance also relates more generally to improved membrane electrode assembly (MEA) construction for other NPMCs.

Initially a porosity study of metal-nitrogen-carbon (MNC) oxygen reduction catalysts and carbon supports found that mesoporosity is critical to high performance. Porous carbon materials with varying structural and compositional properties were studied for their impact on the nitrogen content and activity of MNC catalysts prepared using high-pressure pyrolysis. The carbon materials and resulting catalysts were characterized morphologically, chemically, and electrochemically. The results indicated that substrates adsorbing the most nitrogen and iron show the highest activity. Furthermore, a relationship found between mesoporosity and nitrogen adsorption indicate the importance of transport of precursors to potential active sites. This work had a role in establishing mesoporosity as one of the key parameters in MNC catalyst development.[1] Currently, some of the highest performing catalysts use pore-formers to ensure a high level of mesoporosity.[2-4]

The second project found a correlation between surface alkalinity and catalytic activity for the autogenic pressure MNC (APMNC). The basic site strength and quantity were calculated by two different methods, and it was shown that increased Brønsted-Lowry basicity correlates to

more active catalysts. Future work should elucidate the chemistry found in this MNC catalyst. Specifically, a correlation of this alkalinity data with RRDE analysis of catalysts with varying nitrogen content could couple the basicity with a specific role in the oxygen reduction reaction as discussed in Chapter 4. Another related need for the APMNC is improved understanding of synthesis reactions, which could be accomplished by analysis of gases produced during pyrolysis. This could be accomplished with differential thermal analysis (DTA) or differential scanning calorimetry (DSC).

In Chapter 4, an analysis of peroxide generation using rotating ring-disk electrodes indicated that ORR proceeds both via a direct four-electron pathway to water at high potentials and an indirect peroxide pathway at low potentials. The main contribution of this research was increased understanding of APMNC function. Specifically, oxygen reduction is dominated by the direct four-electron pathway to water without a desorbing intermediate dominates at higher potentials because peroxide generation is inhibited due to site availability. At lower potentials, oxygen reduction begins to shift to the indirect peroxide pathway due to fast kinetics and higher site availability. The net peroxide generation remains relatively low over the entire range due to reduction of peroxide to water. This work not only presents data on a significant catalyst in the literature, but it also represents a novel method for analyzing non-precious metal catalyst via RRDE.

In order to achieve the full benefit of this work, the steady-state RRDE analysis should be performed on multiple catalysts for comparison. For example, performing this analysis for catalysts of differing surface chemistries could isolate the oxygen adsorption properties of various surface groups. One could also study how the measured adsorption coefficients

compared to calculated oxygen binding energies. These types of studies could give important indications of how various catalysts are involved in both reaction pathways.

Chapter 5 presented an electrode-scale, transport model for a proton-exchange-membrane fuel cell (PEMFC) cathode. The model described the performance of non-precious metal catalysts in a fuel cell context. Water flooding was studied in terms of its impact on gas-phase transport and electrochemically accessible surface area (ECSA). Although cathode performance in both air and oxygen are susceptible to ECSA loss, gas diffusion limitations at high current density in air are more significant. In oxygen, catalyst utilization at high current density is primarily limited by conductivity. For this reason, air fuel cell data is recommended over oxygen data for characterizing catalyst performance. Increased loading of low-cost catalysts does not lead to higher performance, due to transport limitations. These findings have been useful in optimization of MEAs for MNC catalysts.

There are two important next steps for this work. First, the model should be validated with a thin platinum electrode. The purpose of this work would be to confirm a correct distribution of transport limitations between the catalyst layer and GDL. The second important step is extending this model to two or three dimensions. The current 1-D model assumes no gradients along the channel, and does not account for the impact of the land on flooding and transport. These features are necessary to properly model GDL behavior.

REFERENCES

REFERENCES

1. K. N. Wood, R. O'Hayre and S. Pylypenko, Recent progress on nitrogen/carbon structures designed for use in energy and sustainability applications, *Energy & Environ. Sci.*, **7**, 1212 (2014), 10.1039/C3EE44078H.

2. A. Serov, M. H. Robson, M. Smolnik and P. Atanassov, Templated bi-metallic non-PGM catalysts for oxygen reduction, *Electrochim. Acta*, **80**, 213 (2012), Doi 10.1016/J.Electacta.2012.07.008.

3. M. H. Robson, A. Serov, K. Artyushkova and P. Atanassov, A Mechanistic Study of 4-Aminoantipyrine and Iron Derived Non-Platinum Group Metal Catalyst on the Oxygen Reduction Reaction, *Electrochim. Acta* (2012)

4. E. Proietti, F. Jaouen, M. Lefevre, N. Larouche, J. Tian, J. Herranz and J. P. Dodelet, Iron-based cathode catalyst with enhanced power density in polymer electrolyte membrane fuel cells, *Nature communications*, **2**, 416 (2011), 10.1038/ncomms1427.